The Dissertation Committee for Michael Jeffrey Clements certifies that this is the approved version of the following dissertation:

A Mathematical Model for Magnetically-Assisted Delivery of Thrombolytics in Occluded Blood Vessels for Ischemic Stroke Treatment

Committee:

Roger T. Bonnecaze, Supervisor

Francis Creighton

Venkat Ganesan

Adam Heller

Nicholas A. Peppas

A Mathematical Model for Magnetically-Assisted Delivery of Thrombolytics in Occluded Blood Vessels for Ischemic Stroke Treatment

by

Michael Jeffrey Clements, B.S.E.

Dissertation

Presented to the Faculty of the Graduate School of

The University of Texas at Austin

in Partial Fulfillment

of the Requirements

for the Degree of

Doctor of Philosophy

The University of Texas at Austin

May 2016

Acknowledgements

First, I would like to thank Dr. Roger Bonnecaze for acting as my advisor and mentor. His support, patience, encouragement, and enthusiasm were tremendous assets during my research. Although he was extremely busy, he still made the time to provide guidance to help me set goals, advice on how to proceed when I was stuck, and feedback both constructive and motivational whenever needed.

In addition, I would like to thank Pulse Therapeutics, Inc. Their exciting and groundbreaking work on magnetically-enhanced diffusion inspired my research.

I would also like to thank the entire Bonnecaze research group for their friendship and for all the memories, lunches, and laughter. I am truly grateful to Derek Bassett, Susana Carranza, and Lavanya Mohan for helping me acclimate and get acquainted with the group. I would also like to thank Erwan Chabert, Meghali Chopra, Soumik Das, Ben Huntington, Akhilesh Jain, Tianfei Liu, Mohammad Shafiei, and Andrew Spann for their insights and for being such good listeners. I am particularly thankful to my office mates Talha Arshad, Mark Ferraro, Shruti Jain, and Parag Katira both for their technical expertise helping me to look at my research from new perspectives and for the multitude of animated discussions and general good times.

Last, but not least, I would like to thank my amazing family for their constant unconditional love and support.

A Mathematical Model for Magnetically-Assisted Delivery of Thrombolytics in Occluded Blood Vessels for Ischemic Stroke Treatment

Michael Jeffrey Clements, PhD

The University of Texas at Austin, 2016

Supervisor: Roger Bonnecaze

Currently, the most popular method of ischemic stroke treatment is intravenous administration of thrombolytics like alteplase. Once administered, the rate of thrombolytic delivery to a clot in a fully occluded vessel is limited by the slow process of diffusion. This is problematic as increased duration of the hypoxic state due to a thrombus or embolus increases the likelihood of severe disability and death.

The transport of the drug could be improved by inducing fluid flow within the blocked vessel. This could be accomplished by utilizing a methodology invented by Pulse Therapeutics. Ferroparticles are administered along with the thrombolytic, and a rotating magnetic field with a gradient is applied to the affected region of the stroke victim's brain. The presence of the magnetic field causes the ferroparticles to aggregate. Its rotation causes the aggregates to rotate, and its gradient causes the rotating aggregates to produce a net unidirectional flow within the blocked vessel.

A general analytical model describing this process is developed to assist prediction of the qualitative effect of changing various system parameters like the magnetic field strength or rotation rate. Increasingly complex two-dimensional models

are developed and computationally analyzed to quantitatively predict the resulting velocity profile in a blocked vessel.

Computational analyses were also performed to simulate the diffusion-limited and magnetically-enhanced transport of thrombolytics. As anticipated, utilizing the rotating magnetic field with a gradient significantly improves transport in a blocked vessel.

Table of Contents

List of Tables

List of Figures

Chapter 1: Introduction

1.1 STROKE

Stroke is the fourth leading cause of death in the United States [Corbyn (2014)]. With a mortality rate of 17 percent, stroke accounts for approximately one out of every eighteen fatalities or 134,000 total fatalities each year [Roger *et al.* (2012)]. Stroke survivors have a roughly 75 percent chance of moderate to severe disability [Kwon *et al.* (2004)]. On average, the lifetime cost of a first stroke per survivor is approximately $140,000 [Roger *et al.* (2012)].

Strokes result in reduced blood flow to a region of the brain. Some are classified as hemorrhagic and are due to ruptured blood vessels. Eight-seven percent of strokes, however, are classified as ischemic [Roger *et al.* (2012)], meaning they result from a blockage of blood flow to the brain due to a thrombus or embolus. A thrombus, or blood clot, forms by aggregation of blood platelets and fibrin usually consequent to an injury to a blood vessel [Furie and Furie (2008)].

The endothelium, which lines the interior of blood vessels, typically ensures that blood vessel walls are not conducive to thrombogenesis or clot formation. When the endothelium is damaged, the subendothelial matrix, which contains collagen and tissue factor, is exposed to the circulating blood. This leads to the formation of a plug at the injury site as blood platelets then bind directly to collagen. Simultaneously, coagulation factor VII in the blood plasma comes into contact with tissue factor to form an activated complex, which can bind to coagulation factor X, activating it. The activated factor X complexes with its cofactor, activated factor V, to yield the prothrombinase complex that activates prothrombin to thrombin. Thrombin performs multiple important functions. It amplifies the coagulation pathway by activating coagulation factors V, VIII, and XI,

converts fibrinogen into insoluble fibrin strands, and activates coagulation factor XIII to crosslink the fibrin strands [Furie and Furie (2008)]. The crosslinked fibrin mesh strengthens the platelet plug and stabilizes the thrombus.

An embolus is typically a detached thrombus or portion thereof, which can become lodged far from the original clot, clogging a blood vessel. The blocked blood flow due to either a thrombus or embolus can result in hypoxia, or oxygen deprivation of cells, and finally cell and tissue death from lack of oxygen. Disabilities, varying based on the location of the clot and affected cells, arise as brain cells die due to prolonged oxygen deprivation as shown in Figure 1.1 [Corbyn (2014)]. Increased duration of the hypoxic state increases the permanency and severity of these disabilities as well as increasing the chance of death.

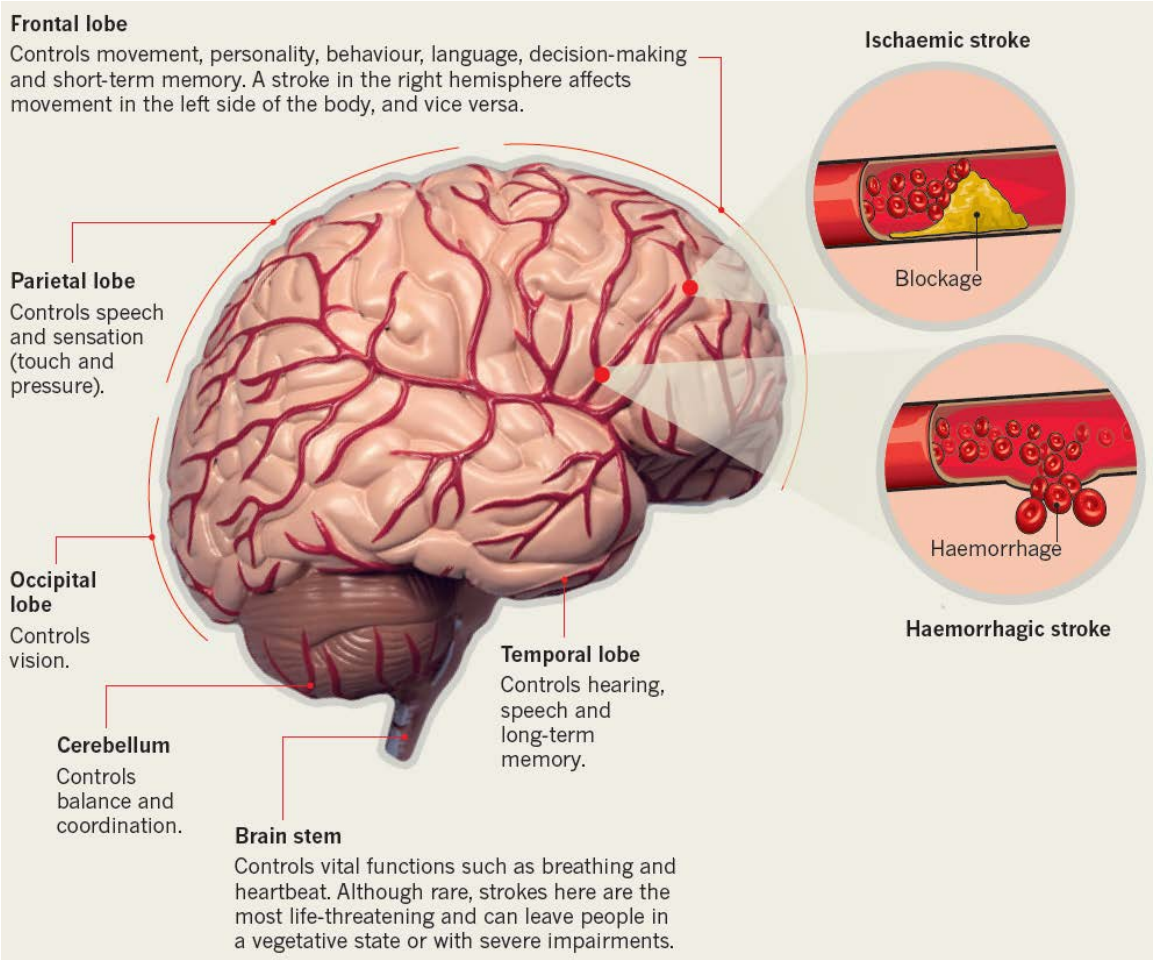

Figure 1.1: Schematic of ischemic and hemorrhagic strokes with functions affected for different areas of the brain [Corbyn (2014)].

1.2 Current Methods of Stroke Treatment

1.2.1 Mechanical Thrombectomy

Several methods have been developed to deal with this widespread and serious health problem. Mechanical thrombectomy, also known as endovascular therapy, mechanical intervention, and embolectomy, involves using a device to physically remove a thrombus. While several different devices exist, their basic components are quite similar. Each device includes a microcatheter through which the rest of the device is

transported to the thrombus, a wire or system of wires to physically ensnare the thrombus, and a balloon guide catheter, which inflates proximal to, or positioned before, the thrombus, to control and suspend blood flow as the clot is being removed or withdrawn. Aspiration, or suction, is applied to the balloon guide catheter, to ensure all clot debris is removed from the blood vessel and cannot act as emboli. The balloon guide catheter subsequently deflates to re-establish flow [Gobin *et al.* (2004), Langer *et al.* (2009), Machi *et al.* (2011)].

The most obvious difference between the various devices is the form of the wire or wires used to withdraw the clot. MERCI X5, X6 and L5 devices use a memory shaped nitinol wire that remains in its straight configuration within the microcatheter. When deployed from the microcatheter, however, it returns to its previously set shape of helical loops as shown in Figure 1.2 [Smith *et al.* (2008)]. The microcatheter must first transverse the thrombus. Then, the first two or three loops of the nitinol wire are delivered distal to, or beyond, the thrombus. These helical loops are pulled back until they contact the thrombus at which point further loops are deployed into the clot. The loops are then torqued before being drawn toward the balloon guide catheter [Gobin *et al.* (2004)].

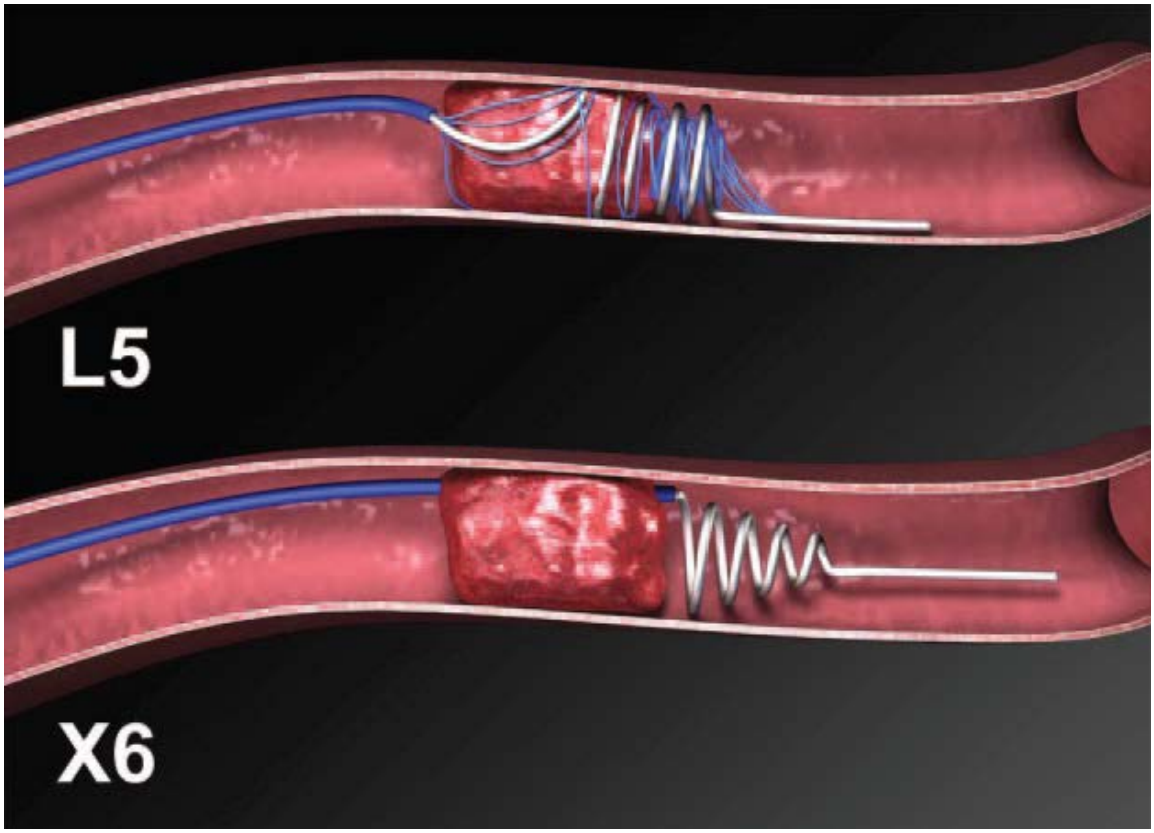

Figure 1.2: Depiction of the L5 and X6 MERCI devices removing a thrombus without balloon guide catheter [Smith *et al.* (2008)].

The Solitaire FR device [Machi *et al.* (2011)], shown in Figure 1.3, uses a nitinol wire mesh that acts as a stent, expanding to fill the blood vessel. As in the MERCI devices, the microcatheter must first transverse the thrombus. The stent retriever is positioned such that it bridges the proximal and distal ends of the thrombus. Next, the microcatheter sheath is retracted allowing the stent to expand before being drawn back to the balloon guide catheter.

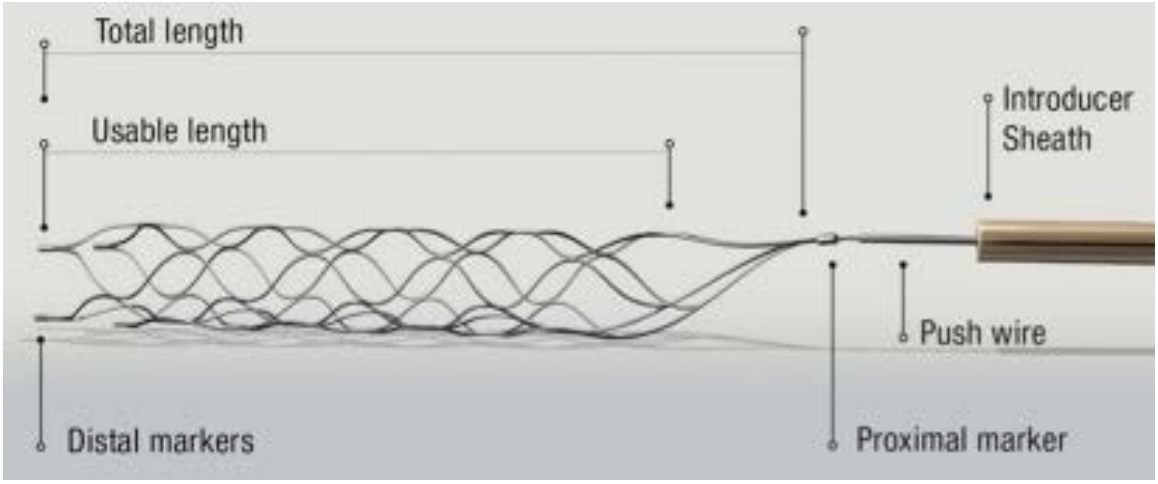

Figure 1.3: Schematic of Solitaire FR device with long stent retriever [Machi *et al.* (2011)].

The Penumbra system [Langer *et al.* (2009)], shown in Figure 1.4, first attempts to remove the thrombus by aspiration using its separator. In this case, suction is applied to a reperfusion catheter instead of the balloon guide catheter. If residual thrombus still remains after aspiration, then a wire mesh, referred to as a thrombus removal ring, is used to remove the thrombus directly, embedding at least a centimeter into the proximal end of the thrombus. Subsequently, the reperfusion catheter is advanced until it is also embedded into the thrombus. Finally, as in the other systems, the thrombus removal ring and reperfusion catheter are drawn back to the balloon guide catheter.

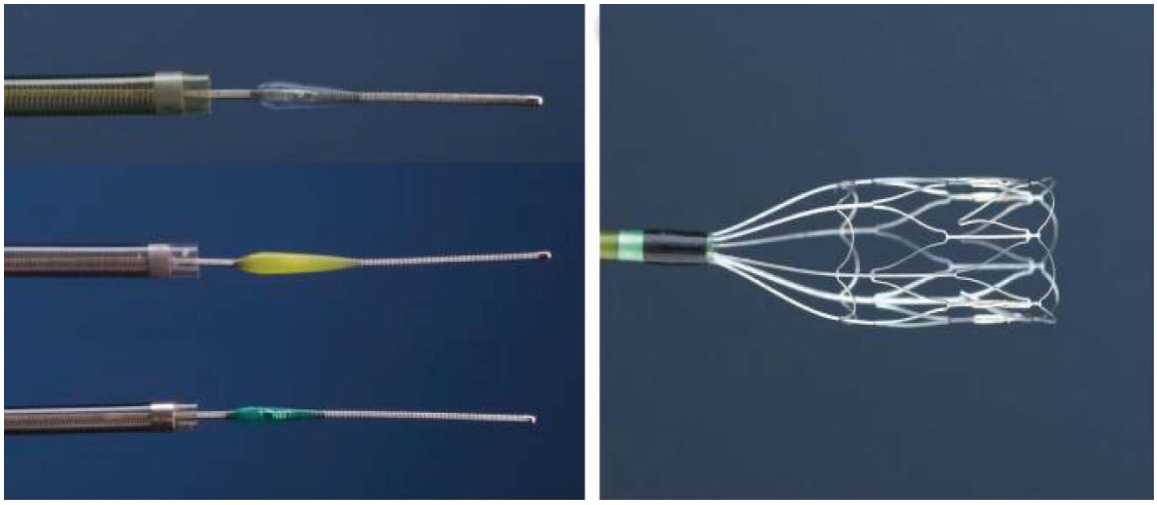

Figure 1.4: Penumbra system including reperfusion catheters and separators (left) and thrombus removal ring (right) [Langer *et al.* (2009)].

Unfortunately, the use of these devices requires a trained doctor to insert a catheter into the femoral artery near the groin and then thread the catheter up to the blockage, or occlusion. In the event that a qualified physician is unavailable, the treatment becomes impractical and would not be performed at all. In addition, the operation should be performed within 6 to 8 hours of stroke onset [Broderick (2009), Powers *et al.* (2015)], and the thrombus needs to be imaged and located first.

1.2.2 Ultrasound

Another potential option for ischemic stroke treatment is thrombus dissolution via ultrasound. This method is known as both sonolysis and sonothrombolysis. The exact mechanism of treatment varies but is often similar to that used in diagnostics to produce ultrasound images. While a low intensity diagnostic ultrasound beam is used to cause targeted microbubbles to oscillate, high intensity ultrasound pressure instead causes the targeted microbubbles to react violently: bursting and releasing energy that can be utilized to destroy a thrombus. Even at lower intensity, the expanding and contracting

microbubbles can deform and erode a thrombus [Chen X. *et al.* (2014), Roos *et al.* (2014)]. At present, however, sonolysis is unused for stroke treatment outside of research unless paired with another method of stroke treatment. Cerevast Therapeutics is developing an ultrasound emitting headset apparatus that could be used in conjunction with intravenous administration of microbubbles without extensive specialized training [Alleman *et al.* (2013)].

Ultrasound's role in typical stroke treatment is generally more preventative. Stroke survivors and individuals otherwise at high risk for stroke may undergo a carotid ultrasound to image the carotid arteries in order to detect blood clots or plaque buildup due to atherosclerosis. Significant plaque buildup can lead to a stroke since the plaque can directly reduce blood flow to the brain or a piece of it may break off to form an embolus. If the ultrasound identifies a problem, the thrombus or plaque may be surgically removed or a carotid artery stent may be inserted [Hill *et al.* (2012)].

Ultrasound may also be used as a low cost, low risk, readily available imaging tool in current stroke victims, but magnetic resonance imaging (MRI) or computed tomography (CT) is typically performed first [Huibers *et al.* (2015)].

1.2.3 Antithrombotic Treatment

The most common method of dealing with thrombi, however, is the use of antithrombotics, or drugs that destroy thrombi or prevent their formation. Antithrombotics include antiplatelet drugs like aspirin, which inhibit platelet aggregation, anticoagulants like heparin, which inhibit the coagulation pathway, and thrombolytics, which dissolve existing thrombi. Thrombolytics are the primary drugs used to treat strokes, although they are often used in conjunction with an anticoagulant or antiplatelet drug.

In addition, administration of thrombolytics may also accompany sonolysis in a treatment invariably referred to as sonothrombolysis [Roos *et al.* (2014)]. In this case, -thrombo- refers to the thrombolytic doing the lysing, or destroying, instead of to the thrombus being destroyed. Such sonothrombolysis may be performed with or without microbubbles. In the absence of the microbubbles, the ultrasound energy produces pressure waves in the blocked artery. This improves delivery of the thrombolytic to the clot as well as penetration of the thrombolytic into the clot [Rubiera and Alexandrov (2010)].

Mechanical thrombectomy may also be used following intravenous thrombolytic therapy [Broderick (2009)]. According to the American Heart Association and American Stroke Association's latest guidelines, mechanical thrombectomy should be attempted following thrombolytic treatment regardless of patient response if still within 6 hours of stroke onset [Powers *et al.* (2015)].

The EKOS ultrasound-assisted catheter-directed thrombolysis system, though currently lacking FDA approval for stroke treatment, actually combines all three methods of treatment as it delivers thrombolytic directly to a blocked vessel while emitting ultrasound to induce pressure waves [McCabe *et al.* (2015)].

1.3 THROMBOLYTICS

Thrombolytics are drugs which aim to break down existing blood clots. Streptokinase (SK), urokinase, and tissue plasminogen activator (tPA) are three commonly used thrombolytics that are termed fibrinolytics, which break down the fibrin in a clot. Streptokinase, urokinase and tPA all function by activating plasminogen, a zymogen that is produced by the liver [Mehta and Shapiro (2008)] and comprises part of

thrombi. The active enzyme, plasmin, then directly breaks down the blood clots by cleaving the fibrin mesh holding the clot together [Baker (2003)]

Streptokinase is produced by streptococci bacteria. In order to activate plasminogen, SK complexes with it in a 1:1 stoichiometric ratio [Lottenberg *et al.* (1992), Runge *et al.* (1989), Verstraete (1987)]. Urokinase is an active human enzyme that was originally isolated from urine, although it can be found in different physiological locations including kidney cells [White *et al.* (1966)]. As an active enzyme, urokinase can directly convert plasminogen into plasmin by cleaving a specific peptide bond without forming a complex. tPA is a human protein that is secreted by various tissues, including the endothelium. tPA and plasminogen react according to Michaelis-Menten enzyme-substrate kinetics. Streptokinase lacks fibrin selectivity, but tPA binds fibrin, which catalyzes the reaction with plasminogen when bound [Runge *et al.* (1989)].

Streptokinase, urokinase, and tPA have all been FDA approved thrombolytics at one time. Urokinase was most recently re-approved by the FDA in 2002 for treatment of pulmonary emboli, or for clots obstructing blood flow to the lungs, but not ischemic stroke. At that time, urokinase was produced by Abbott Laboratories under the brand name Abbokinase. Subsequently, Microbix acquired the rights to Abbokinase and re-branded it as Kinlytic. Unfortunately, Microbix's lack of an approved manufacturing facility has kept urokinase unavailable to patients since 2009 [Microbix].

Streptokinase production under the brand name Streptase has been discontinued in the US, however, it was once FDA approved for treatment of myocardial infarctions, commonly known as heart attacks. Streptokinase is still marketed globally for treatment of heart attack, pulmonary embolism, and deep vein thrombosis. It is sold under a variety of names, most notably Streptase, which is produced by CSL Behring for use in Argentina, Australia, Bosnia & Herzegovina, Brazil, Bulgaria, China, Denmark,

Germany, Hong Kong, Hungary, Indonesia, Israel, the Netherlands, New Zealand, Poland, Portugal, Serbia, Spain, Sweden, Taiwan, and the United Kingdom, by Sanofi Aventis for use in Bangladesh, India, and Taiwan, and by various other companies for use in Colombia, Croatia, Egypt, Greece, Lebanon, Malta, South Africa, and Turkey. It is sold under other names in Georgia, Lithuania, Mexico, Myanmar, Pakistan, the Philippines, and Vietnam [Drugs.com]. A recombinant form of streptokinase, known as Heberkinasa, or Heberkinase, is manufactured by Heber Biotech and sold throughout much of Latin America including Cuba, Ecuador, and Venezuela [Hermentin *et al.* (2005)]. Indeed, streptokinase remains the most commonly used thrombolytic worldwide. This is likely due, in large part, to its low cost. Streptokinase is cheaper than urokinase and much cheaper than tPA. Streptokinase is also the only thrombolytic on the World Health Organization's List of Essential Medicines, which is meant to include the most important medications necessary in any basic healthcare system, prioritizing efficacy, safety and cost-effectiveness [World Health Organization].

The brands of tPA that are commercially available in the United States today are recombinant tPA's. Tenecteplase, produced under the brand name TNKase by Genentech, has higher fibrin specificity than native tPA [Genentech], while reteplase, produced under the brand name Retavase by Chiesi USA, has lower fibrin specificity than native tPA [Chiesi USA]. Both tenecteplase and reteplase are FDA approved for treatment of myocardial infarction but not ischemic stroke. Alteplase, produced under the brand name Activase by Genentech, is in fact the only thrombolytic FDA approved for treating ischemic stroke [Food and Drug Administration]. It should be administered intravenously within three hours of stroke onset [Donnan *et al.* (2003)]. Alteplase is broadly applicable and is also approved for treatment of both myocardial infarctions and pulmonary emboli [Genentech].

The decision by the FDA to not approve streptokinase for ischemic stroke treatment was quite controversial. The decision was likely based off the three intravenous streptokinase trials: Australian Streptokinase Trial (ASK) and the two Multicenter Acute Stroke Trials: European (MAST-E) and Italian (MAST-I). Each of the trials was terminated prematurely due to excess mortality due to hemorrhaging. All three of these trials are widely believed to have been flawed in their design, however. In the streptokinase ischemic stroke trials, the treatment time window and the administered dosage relative to the cardiac dosage were larger than in tPA trials, and streptokinase was administered along with aspirin and/or heparin [Broderick and Hacke (2002), Cornu *et al.* (2000), Jaillard *et al.* (1999)]. Due to the premature end to those trials, these issues were left uncorrected. Despite all these experimental design flaws promoting the risk of hemorrhaging, the ASK trial still found a trend toward patient benefit when focusing only on the sub-set of patients treated within three hours [Broderick and Hacke (2002)], which is the same as the current recommended time window for administration of alteplase.

The issue with intravenous administration of any thrombolytic, including alteplase, is that its delivery to a thrombus in a fully occluded vessel is limited by its rate of diffusion [Clements and Bonnecaze (2013), Piebalgs and Xu (2015)]. Hospitals strive to minimize their door-to-needle time, or the time between patients entering the hospital and being administered the thrombolytic. This serves to maximize the percentage of stroke patients able to receive IV thrombolytic treatment within the typically required 3 to 4.5 hour time window [Maulaz *et al.* (2009)]. Once the drug has been administered, however, the time required for it to reach the clot and react is controlled by convection, diffusion, and reaction kinetics. The delay in thrombolytic delivery to the clot due to slow diffusion in a completely blocked artery could easily prove fatal. Unfortunately, the simplest method of improving diffusion rate by increasing the concentration of

thrombolytic is impractical since elevated concentration leads to high risk of hemorrhaging and other bleeding complications [Gardell (1993), Van de Werf (1999)].

In intra-arterial thrombolytic stroke treatment, the thrombolytic is delivered directly into the occluded vessel at the clot within six hours of stroke onset. This eliminates the time delay associated with the drug's diffusion through the blocked vessel to the thrombus. In addition, since the thrombolytic is delivered locally, systemic fibrinolysis is avoided, reducing the chance of bleeding complications arising. Like mechanical thrombectomy, however, intra-arterial stroke treatment requires a trained doctor to perform the procedure after the thrombus has been located and imaged [Mattle (2007)].

1.4 Mechanism for Magnetically-Assisted Delivery of Thrombolytics

Pulse Therapeutics has invented a method for rapidly delivering thrombolytics that can be easily performed by a nurse [Creighton (2012), Creighton (2013), Creighton (2014)]. The apparatus associated with this delivery method is a permanent magnet that uses a two-motor system so that it can rotate in any plane. It generates a rotating magnetic field with a gradient and applies it to the affected area of the stroke victim's brain. The affected area is typically determined from a CT scan. Approximately 0.1 micron diameter ferroparticles added to the IV during thrombolytic administration interact with the magnetic field, inducing a flow within the occluded vessel (Figure 1.5).

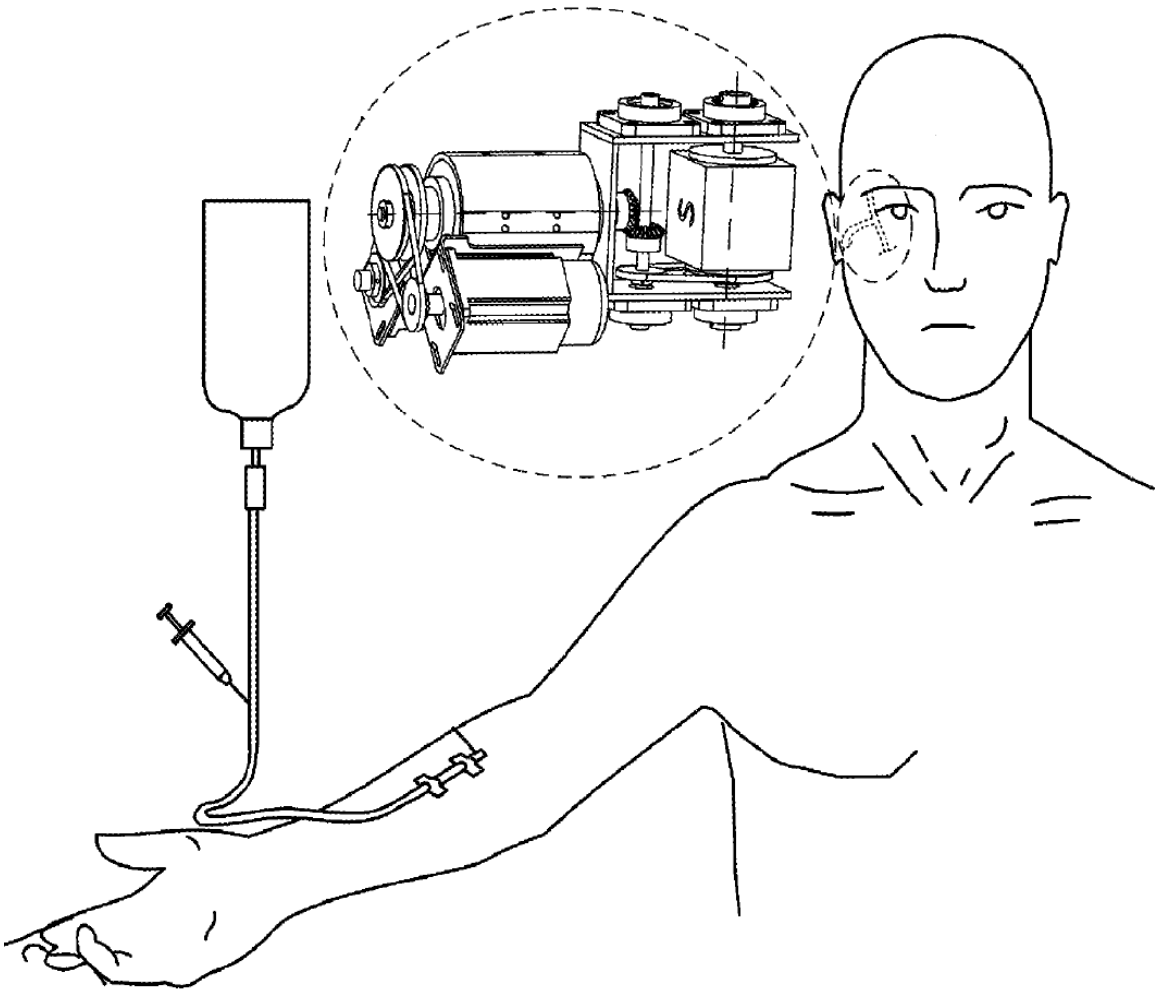

Figure 1.5: Schematic of Pulse Therapeutic's method for treating ischemic strokes by adding ferroparticles during the thrombolytic's IV administration and using a specially designed apparatus to apply a rotating magnetic field with a gradient to the affected area of the brain [Creighton (2014)].

In the presence of a magnetic field, ferroparticles aggregate into chains, which experience a torque and subsequent rotation in a rotating magnetic field. The hypothesis is that the rotation of the particle aggregates is the immediate cause of the induced fluid flow in the blocked vessel, re-establishing convective transport and eliminating the problem of slow diffusive drug delivery.

1.4 DISSERTATION OUTLINE

In the following chapters, I will discuss thrombolytic delivery and models thereof for both the standard diffusion-limited intravenous method and Pulse Therapeutic's magnetically-enhanced method.

In Chapter 2, diffusion-limited thrombolytic delivery is studied computationally. A computational model simulating streptokinase and tPA's transport and reaction with plasminogen in the occluded vessel and the unblocked vessel from which it branches is developed. The length and diameter of the blocked vessel, the flowrate in the unblocked vessel, and the angle between the two vessels are all treated as system variables. The concentration profiles for the thrombolytics and plasminogen one hour after the start of the intravenous treatment are predicted. The amount of the drug delivered to the thrombus is also simulated transiently.

In Chapter 3, a general analytical model for Pulse Therapeutic's method of magnetically-assisted thrombolytic delivery is setup in which the ferroparticles are assumed to have already aggregated into chains in response to the presence of the magnetic field. Equations describing the rotation of the aggregates are derived by balancing the magnetic and hydrodynamic torques acting on the aggregates. The fluid flow is described according to conservation of mass and linear momentum. The suspension dynamics of the fluid flow are linked to the particle dynamics of the aggregates' rotation by the antisymmetric stress and magnetic torque resulting from the body couple of the applied magnetic field acting on the magnetized particles.

In Chapter 4, the model is simplified to a two-dimensional model for the theoretical case where the source of the magnetic field is located at the occluded vessel and the size of the aggregates is fixed with respect to both space and time.

In Chapters 5 and 6 the two-dimensional model is improved. In Chapter 5, the model is made to account for the magnetic field source's displacement from the occluded vessel. This corresponds with Pulse Therapeutic's magnet apparatus rotating beside the patient's head instead of inside it. In Chapter 6, the model is further improved to account for the aggregate size being functionally related to the shear and to the applied magnetic field's strength and rotation rate. The aggregates grow in response to increasing magnetic field strength and can be torn apart by increasing shear or H-field rotation rate.

In Chapter 7, the magnetically-enhanced transport of a non-reactive species in an occluded vessel is computationally studied. Finally, in Chapter 8, key conclusions, drawn from the model and simulations, are presented along with recommendations for future work on this topic.

Chapter 2: Diffusion-Limited Thrombolytic Delivery*

2.1 INTRODUCTION

Stroke is the fourth leading cause of death in the United States accounting for approximately one out of every eighteen or 134,000 total fatalities each year [Corbyn (2014), Roger *et al.* (2012)]. Stroke has a mortality rate of over 17 percent, and the survivors have about a 75 percent chance of moderate to severe disability [Kwon *et al.* (2004), Roger *et al.* (2012)]. Some strokes are classified as hemorrhagic and are due to ruptured blood vessels. Eighty-seven percent of all strokes though are ischemic [Roger *et al.* (2012)], caused by a blockage of blood flow and starvation of oxygen to the brain due to a thrombus or embolus.

Thrombolytics are an important class of pharmaceutical treatment that aims to break down existing blood clots, thereby eliminating them. Most thrombolytics can also be termed fibrinolytics, which specifically break down the fibrin in a clot. Streptokinase (SK) and tissue plasminogen activator (tPA) are two commonly used fibrinolytics. Both of these proteins activate plasminogen, which is part of the thrombi, to plasmin which cleaves fibrin mesh and breaks down blood clots [Baker (2003)].

Despite the ideal placement of plasminogen in the clot, timely delivery of a thrombolytic remains difficult, particularly in more severe strokes. As a thrombus blocks off blood flow, convective transport of the drug to the clot decreases. If the blood vessel completely clogs so there is no blood flow past the thrombus or embolus, convection can only transport the drug to the branch point of the occluded vessel. Subsequent delivery to

---

* Much of this chapter has appeared in Clements M. and R. Bonnecaze, "Diffusion limited delivery of streptokinase and tPA to a thrombus," *Cardiovascular Engineering and Technology* **4** (4), 364-373 (2013).

Dr. Bonnecaze contributed to this publication by advising on the research and critiquing the article.

the clot must be achieved solely by diffusion in the blocked vessel. This is especially problematic because diffusion is much slower than forced convection; the resulting time lag could easily be fatal.

For effective treatment, an amount of thrombolytic sufficient to dissolve the clot must be delivered to the thrombus as soon as possible before a large number of brain cells die from oxygen and nutrient deprivation. Typically hospitals adhere to a 3 to 4.5 hour treatment window for thrombolytics like tPA [Maulaz *et al.* (2009)]. More than 3 hours after the initial presentation of stroke symptoms, most physicians opt not to administer a thrombolytic since the probability of the treatment saving the life of the patient is very small and the risk of unwanted side effects such as hemorrhaging increases. Hospitals have set up rigorous protocols to reduce their door-to-needle time, or the time lost between the patient entering the hospital and having the thrombolytic administered to them. This is beneficial, but once injected the time needed for the thrombolytic to reach and react with the thrombus is controlled by the convection, diffusion, and reaction in the bloodstream and the thrombus [Donnan *et al.* (2003), Gardell (1993), Runge *et al.* (1989), Van de Werf (1999), Verstraete (1987)].

The reaction of streptokinase and tPA with plasminogen is computationally studied as they convect and diffuse from the bulk flow in the neighboring unblocked vessel through the occluded vessel to the thrombus to be treated. This study complements previous computer simulations that analyzed the kinetics and diffusive transport of thrombolytics through a clot but did not consider the transport through the occluded vessel [Anand and Diamond (1996), Diamond and Anand (1993)]. Since the diffusion-limited transport through the occluded vessel is rate limiting, this study is vital to more accurately determine the time needed to deliver the required amount of streptokinase or tPA. Different occluded vessel geometries and flow rates are considered.

2.2 Model Description

To understand the time required for streptokinase and tPA to be delivered to a thrombus, simulations were developed to describe the convective and diffusive transport and reactions of the drugs in an artery. The geometry of the model (Figure 2.1) incorporates the thrombus, a segment of the unblocked vessel from which the occluded vessel branches, and the length L of the clogged vessel between the clot and the branch point. For these simulations, the typical radius of the nearby unblocked vessel is assumed to be 0.5 mm. Other geometric variables include the angle θ between the blocked and unblocked vessels, the diameter D of the occluded vessel and the length L to the occlusion. The blood flow rate is Q. The angle is measured on the downstream side of the occluded vessel and simulations were run for θ = 30°, 45°, and 60°. The diameters D of simulated clogged vessels were assumed to range from 0.5mm to 0.75mm to 1mm. The length of the blocked vessel, as well as position along the vessel, is measured along its upstream side from the unblocked vessel to the thrombus. Simulations were performed for lengths of 0.25cm, 0.5cm, and 0.75cm.

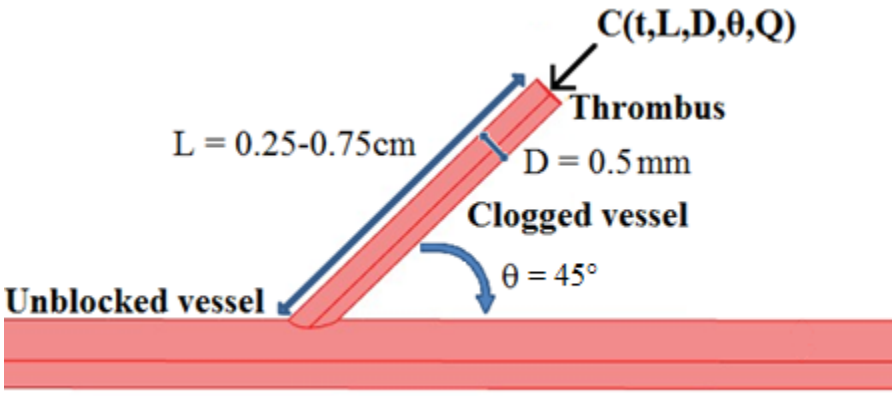

Figure 2.1: Geometry of model simulating thrombolytic drug delivery. The geometric system variables of occluded vessel length L, occluded vessel diameter D, and angle between the clogged and unblocked vessels θ are shown.

Using a more complex geometry does not change the qualitative nature of our conclusions. As will be seen, the flow only penetrates approximately two diameters into the occluded vessel. After that point, transport is completely diffusive. A more tortuous diffusion path of a curved cerebral artery only increases the diffusive length, which is essentially the contour length of the occluded artery in this study. The bulk flow rates in the unobstructed artery were set to 1mL/min, 2mL/min, and 3mL/min. In a 1mm diameter artery these flow rates are equivalent to superficial velocities of 2.12cm/s, 4.24cm/s, and 6.36cm/s, respectively.

The blood flow's conservation of mass is described by the continuity equation, given by

$$\nabla \cdot \mathbf{u} = 0, \tag{2.1}$$

where **u** is the velocity vector. Assuming blood is a completely incompressible fluid, the Navier-Stokes equation governing the blood flow becomes

$$\rho \frac{\partial \mathbf{u}}{\partial t} + \rho(\mathbf{u} \cdot \nabla)\mathbf{u} = \nabla \cdot \left[-p\mathbf{I} + \mu\left(\nabla \mathbf{u} + (\nabla \mathbf{u})^T\right)\right] + \mathbf{F}, \tag{2.2}$$

where p is pressure, and **F** denotes external forces. The physical properties of blood are assumed to be similar to water, so its density ρ is set to 1,000kg/m^3 and its viscosity μ is set to 10^{-3}Pa·s. Since the introduction of the thrombolytic into the bloodstream should alter the blood flow itself very little, the blood flow is assumed to be at steady state on average so that the derivative with respect to time t drops out of the equation. For this study, the flow is assumed constant and so only the pressure gradient is determined in the Navier-Stokes equations. For this assumption, the relative pressures between different points in the flow domain are all that matter, while the absolute pressure is not relevant to the fluid dynamics.

The boundary conditions are no slip ($\mathbf{u} = 0$) at the vessel walls and at the clot. At the upstream end of the unblocked vessel, the velocity is set equal to the superficial velocity. The viscous stress is assumed to be zero at the outlet.

The convective-diffusive-reactive transport of the thrombolytic drug τ and plasminogen P is described by

$$\frac{\partial \tau}{\partial t} + \mathbf{u} \cdot \nabla \tau + \nabla \cdot \left(-D_\tau \nabla \tau \right) = R, \tag{2.3}$$

$$\frac{\partial P}{\partial t} + \mathbf{u} \cdot \nabla P + \nabla \cdot \left(-D_P \nabla P \right) = R, \tag{2.4}$$

where R represents the rate of reaction and D_τ and D_P represent the diffusion coefficients of the thrombolytic and plasminogen, respectively. The diffusion coefficients for streptokinase, tPA and plasminogen are assumed to be approximately the same. A typical diffusion coefficient for a small protein in water is between 10^{-9}m^2/s and 10^{-10}m^2/s [Norris *et al.* (2012), Reilly (2008)], so $D_\tau = D_P = 3$mm^2/hr or 8.3×10^{-10}m^2/s. For streptokinase $R = -k[S][P]$ without any particular fibrin specificity [Runge *et al.* (1989)]. Plasminogen is produced by the liver and introduced into the systemic circulation resulting in a standard concentration of 122mg/L (1.506μM) in flowing blood plasma [Barlow *et al.* (1969), Leipnitz *et al.* (1988)]. In the bulk bloodstream, a pseudo-reaction rate constant ($k'=k[P]$) was calculated using streptokinase's half-life of 23 minutes [Baker (2003)], namely

$$\frac{c}{c_0} = e^{-k't}. \tag{2.5}$$

The pseudo-reaction rate constant is therefore 5.023×10^{-4} s^{-1} and then the reaction rate constant $k = 0.3335$m^{3}mol^{-1}s^{-1}.

tPA and plasminogen react according to Michaelis-Menten enzyme-substrate kinetics, and the reaction rate for tPA is $R = -0.07 s^{-1}[T][P]/(83\mu M+[P])$ [Runge *et al.* (1989)]. For these convection-diffusion-reaction equations, the boundary conditions are zero flux through the vessel walls, no flux of free plasminogen through the clot, and negligible concentration change with position at the outlet. At the inlet, the concentration of plasminogen is set to $1.506\times10^{-3} mol/m^3$ or $1.506\mu M$.

The time variation of the concentration of the thrombolytics at the inlet is more complex. When streptokinase is used to treat a stroke, up to 1.5 million units are administered by IV into the neck or arms over the course of one hour [Verstraete (1987)]. Here, a lower dose of one million units in an hour is used to decrease the probability of bleeding complications. Since purified streptokinase has an activity of approximately 70,000 units/mg, a million units amount to 0.0143g [Banerjee *et al.* (2004)]. A typical patient would have a blood volume of about 5.2L and a cardiac output of approximately 5L/min [Herman (2007)]. Nearly all his blood would complete at least one cycle, traveling from the heart to the organs or extremities and back again, in about one minute. Dilution of the thrombolytic in 5.2L of blood over the course of one hour yields $1.614\times10^{-8} mol\cdot m^{-3}s^{-1}$ since streptokinase has a molecular weight of 47,287g/mol [Parrado *et al.* (1996)]. It should take roughly half a minute for blood to travel from the administration point for the thrombolytic to the thrombus. Solving equation (2.5) for the streptokinase concentration per unit time after 30 seconds yields $1.590\times10^{-8} mol\cdot m^{-3}s^{-1}$ as the concentration at the inlet to the simulated region at the start time for the simulation (t=0s), 30 seconds after the drug's administration. Between t=0s and t=3600s, the concentration would increase by $1.590\times10^{-8} mol/m^3$ every second as thrombolytic continues to be administered except the thrombolytic is continually reacting in the bloodstream according to equation (2.5). As such the inlet concentration of streptokinase

during the first hour S_{i1} must account for both the IV administration and half-life of streptokinase.

$$S_{i1} = 1.590\times10^{-8}\,\frac{\text{mol}}{\text{m}^3\cdot\text{s}}\int_0^t e^{-(5.023\times10^{-4}\,\text{s}^{-1})t}\,dt \tag{2.6}$$

$$S_{i1} = 3.165\times10^{-5}\,\frac{\text{mol}}{\text{m}^3}\left(1-e^{-\left(5.023\times10^{-4}\,\text{s}^{-1}\right)t}\right) \tag{2.7}$$

The systemic plasminogen concentration outside the simulated region is assumed to be constant since it can be replenished by the liver. Note at t=3600s, the inlet concentration peaks at $2.647\times10^{-5}\text{mol/m}^3$. After the first hour, it is assumed that the inlet concentration of streptokinase decays exponentially from its peak value according to its half-life:

$$S_{i2+} = 2.647\times10^{-5}\,\frac{\text{mol}}{\text{m}^3}e^{-\left(5.023\times10^{-4}\,\text{s}^{-1}\right)(t-3600\text{s})}. \tag{2.8}$$

The inlet concentration of tPA is obtained in a similar manner. tPA is also delivered by IV into the neck or arms over the course of an hour, but the amount depends upon the body mass of the patient. 0.9mg of tPA are administered per kilogram of body mass [Eissa *et al.* (2012)], so for an ordinary 75kg person a total of .0675g of tissue plasminogen activator would be used [McDowell *et al.* (2008), Walpole *et al.* (2012)]. tPA has a molecular weight of around 70000g/mol [Van de Werf (1999)], so diluting it in 5.2L of blood over the course of an hour gives $5.151\times10^{-8}\text{mol}\cdot\text{m}^{-3}\text{s}^{-1}$. After 30 seconds, the initial inlet concentration for tPA is $4.962\times10^{-8}\text{mol}\cdot\text{m}^{-3}\text{s}^{-1}$. Setting the free plasminogen concentration to 1.506μM, the reaction rate for tissue plasminogen activator becomes $-1.2475\times10^{-3}\text{s}^{-1}[T]$, and from that the inlet concentration of tPA T_i is defined.

$$T_{i1} = 4.962\times10^{-8}\,\frac{\text{mol}}{\text{m}^3\cdot\text{s}}\int_0^t e^{-\left(1.2475\times10^{-3}\,\text{s}^{-1}\right)t}\,dt \tag{2.9}$$

$$T_{i1} = 3.978\times10^{-5}\,\frac{\text{mol}}{\text{m}^3}\left(1-e^{-\left(1.2475\times10^{-3}\,\text{s}^{-1}\right)t}\right) \tag{2.10}$$

Again, note at t=3600s, the inlet concentration peaks at 3.934×10^{-5}mol/m^3. After the first hour, the inlet concentration of tPA decays exponentially from its peak value:

$$T_{i2+} = 3.934\times10^{-5}\,\frac{\text{mol}}{\text{m}^3}\,e^{-\left(1.2475\times10^{-3}\,\text{s}^{-1}\right)(t-3600\text{s})}. \qquad (2.11)$$

Another boundary condition is the reaction rate of the thrombolytic and plasminogen at the clot. Forming and developed thrombi have an elevated plasminogen concentration compared to flowing blood plasma. A typical plasminogen concentration within a thrombus is 2.116μM [Cederholm-Williams (1981)]. To simplify the analysis, the bound plasminogen concentration [P_b] within the clot is assumed constant. While streptokinase is believed to penetrate into the clot and perform endogenous fibrinolysis, the boundary condition for the thrombus would be best implemented as a flux or surface reaction rate. In order to convert the bulk reaction rate to a surface reaction rate, a characteristic clot thickness δ is defined as $\sqrt{D_\tau/k}$. Multiplying the characteristic clot thickness with the bulk reaction rate approximates the flux through the surface of the thrombus. For streptokinase, the clot thickness is 1.084×10^{-3}m (1.084mm), and the reaction's mechanism and rate constant remain the same as in the bulk flow. As a result, the flux is 7.653×10^{-7}m/s times the local concentration of the streptokinase. For tPA, the fibrin in the thrombus catalyzes the reaction, changing the Michaelis-Menten type reaction rate to $0.28\text{s}^{-1}[T][P_b]/(0.18\mu\text{M}+[P_b])$, or $0.258\text{s}^{-1}[T]$ [Runge *et al.* (1989)]. The characteristic clot thickness is 5.671×10^{-5}m and the flux is 1.4635×10^{-5}m/s times the local concentration of tPA at the surface of the thrombus.

The equations were solved numerically using the finite-element package COMSOL. In order to reduce the required computational time and memory, the simulated system geometry is symmetrically split in half. The centerlines of the two arteries define the plane symmetrically splitting the system. This split results in an

additional boundary, but symmetry defines the necessary conditions. In the Navier-Stokes equation, the net flow across the symmetry boundary is zero, and in the convection-diffusion equation, the net flux of the protein across the boundary is zero.

With the system geometry and its domain and boundary conditions defined, the only remaining issues are the initial conditions for the transient convection-diffusion problem of the thrombolytics and plasminogen. At t=0s, no thrombolytic has entered the simulated region yet so its concentration throughout is 0mol/m^3. Also, at the start of the simulation, no thrombolytic has yet reacted with the plasminogen in the occluded vessel and the systemic plasminogen concentration outside the simulated region is assumed to be constant at 1.506μM.

Using these equations and conditions, the base case of L=0.5cm, D=0.5mm, θ=45°, and Q=2mL/min was solved, first for streptokinase and then for tPA, to obtain the local concentration of the thrombolytic at the clot site. This was achieved by simultaneously solving the Navier-Stokes and continuity equations under steady state conditions and then using the velocity field profile obtained to solve the transient convection-diffusion equation with 10 second time steps. Subsequently, another 16 cases were simulated (8 for streptokinase and 8 for tPA) in which each system variable was changed individually while the other variables remained at their base values.

2.3 CONCENTRATION PROFILES

Concentration profiles of the simulated region were obtained for the base case one hour after the first thrombolytic molecules reached the inlet. After one hour, the concentration of streptokinase ranges from 0.48nM at the clot to 26.5nM in the unblocked vessel (Figure 2.2a). When streptokinase is used, the concentration profile of

plasminogen has a peak value of 1.506μM in the unblocked vessel and a minimum value of 1.502μM near the middle of the occluded vessel (Figure 2.2b).

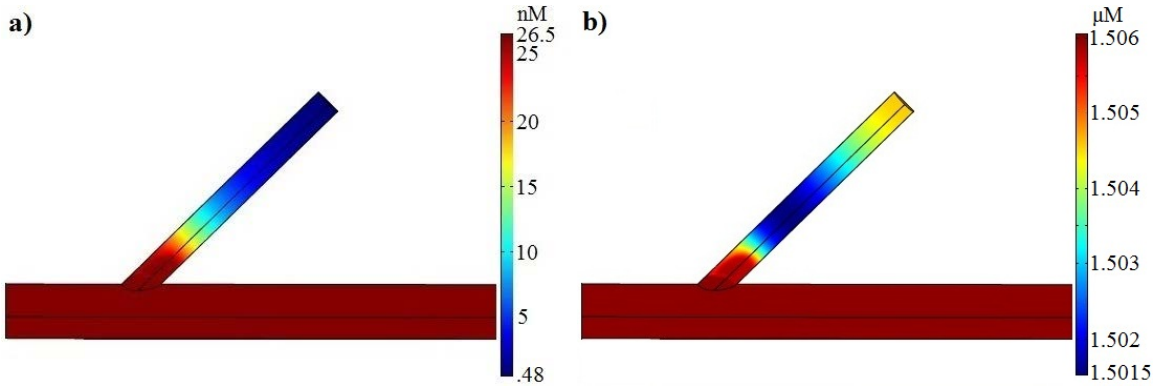

Figure 2.2: Typical concentration profiles one hour after start of streptokinase administration with system variables set to L=0.5cm, D=0.5mm, θ=45°, and Q=2mL/min. a) Concentration profile for streptokinase, b) concentration profile for plasminogen. Note that convection transports the streptokinase partially up the branched vessel, but diffusion is required to deliver it to the thrombus.

For the base case, about an hour after the start of administration, the concentration of tPA ranges from 0.03nM at the clot to 39.5nM in the unblocked artery (Figure 2.3a).

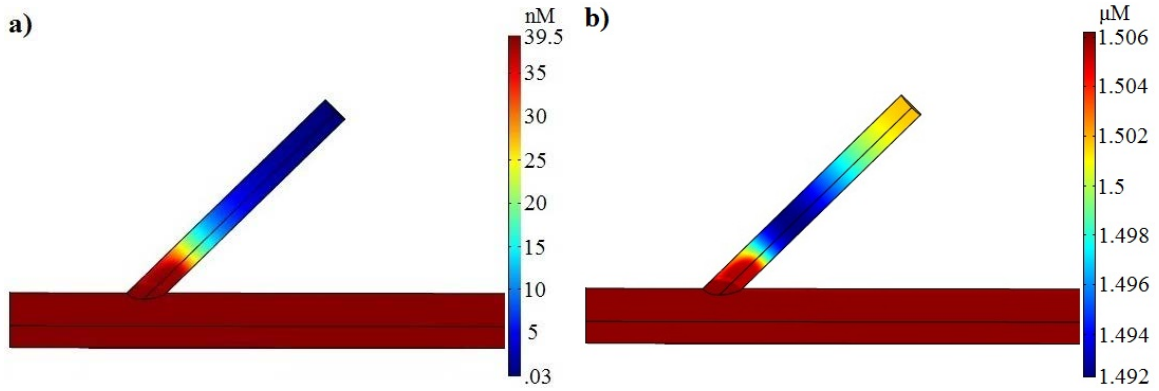

Figure 2.3: Typical concentration profiles one hour after start of tissue plasminogen activator (tPA) administration with system variables set to L=0.5cm, D=0.5mm, θ=45°, and Q=2mL/min. a) concentration profile for tPA, b) concentration profile for plasminogen. Note that convection transports the tPA partially up the branched vessel, but diffusion is required to deliver it to the thrombus.

Still analyzing the thrombolytic concentration profile one hour after the beginning of IV administration, the effect of changing each of the system variables is investigated. For streptokinase, decreasing the branch angle from 45° to 30° causes the local concentration at the clot to increase from 0.48nM to 0.71nM (Figure 2.4b).

Increasing the occluded vessel diameter from 0.5mm to 1mm causes the local concentration of streptokinase at the thrombus after one hour to increase from 0.48nM to 1.54nM (Figure 2.4c). Decreasing the volumetric flow rate through the unblocked vessel by a factor of two from 2mL/min to 1mL/min only shifts the streptokinase concentration at the thrombus from 0.48nM to 0.45nM for a change of about 6 percent (Figure 2.4d). Decreasing the length of the occluded vessel by a factor of two from 0.5cm to 0.25cm, however, allows the thrombolytic concentration to rise from 0.48nM to 6.36nM at the clot (Figure 2.4e).

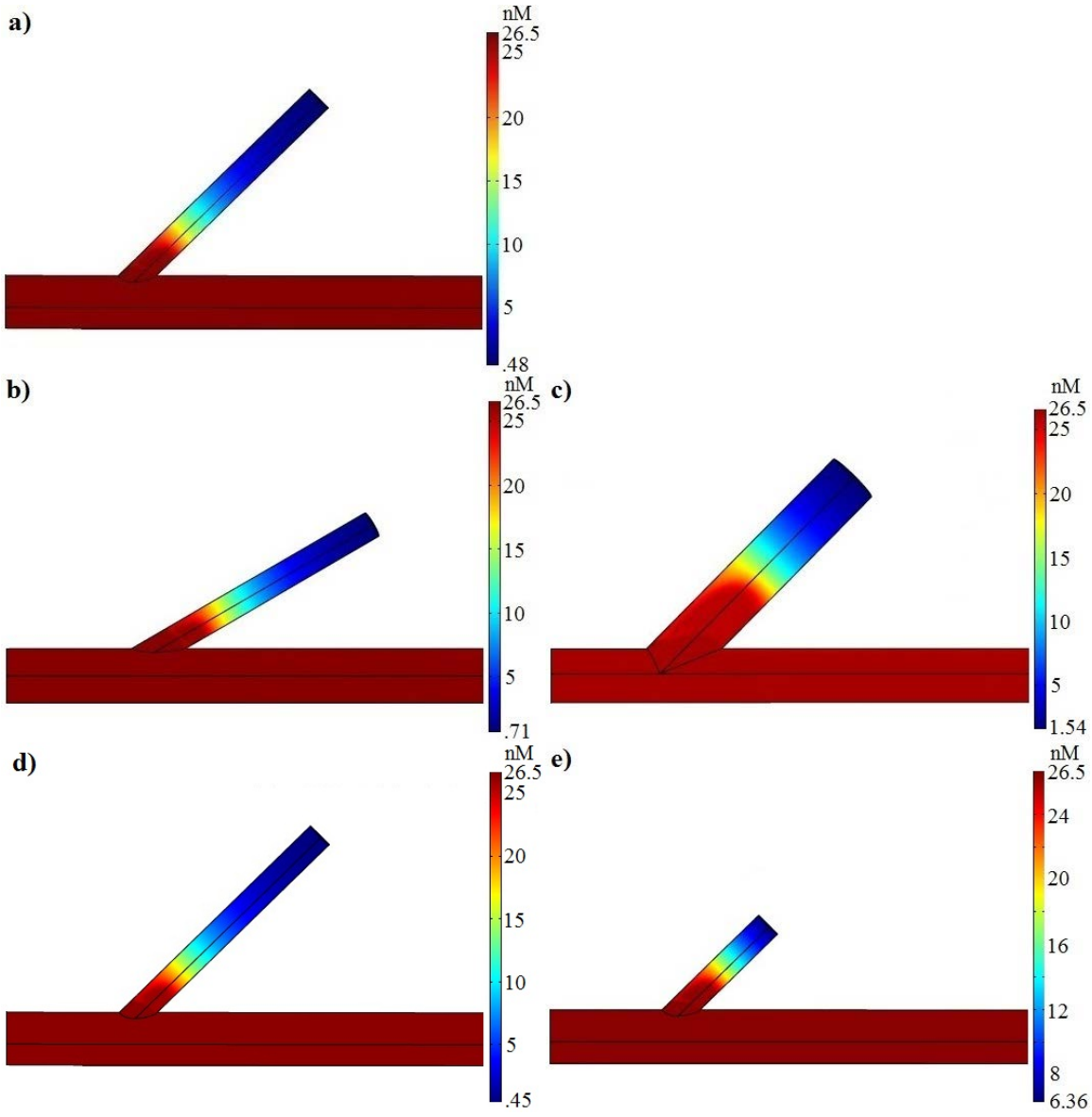

Figure 2.4: Concentration profiles demonstrating effect of changing system variables. a) Base case of L=0.5cm, D=0.5mm, θ=45°, and Q=2mL/min using streptokinase, b) angle changed to 30°, c) diameter of clogged vessel changed to 1mm, d) flowrate changed to 1mL/min, e) length of blocked vessel changed to 0.25cm.

2.4 TRANSIENT THROMBOLYTIC DELIVERY

In order to determine the total amount of thrombolytic that is ultimately delivered to a clot as a result of one hour IV administration to the neck or arms, the transient concentration of the drug at the thrombus must be considered. A complete analysis also requires at least three sets of data for each variable system parameter to establish a pattern. Tracking the clot concentration of both streptokinase and tPA over time at different values of θ further confirms the pattern suggested by the values found for streptokinase at 30° and 45° after one hour. The concentration also decreases when the angle is changed from 45° to 60° (Figure 2.5a-b). While the maximum inlet concentration is obtained one hour after the first thrombolytic molecules reached the inlet, the peak thrombus concentration is obtained about 1.5 hours after t=0s, slightly earlier for tPA. The tPA concentration at the thrombus decreases to a negligible amount relative to its maximum after 2.5-3 hours, while 4.5-5 hours are needed for the local clot concentration of streptokinase to become negligible. The tPA concentration peaks slightly earlier, decays faster after peaking, and experiences a noticeable decrease in its first derivative around one hour, when the thrombolytic stops being administered, all because tPA is consumed faster in the bulk bloodstream than streptokinase. The even more rapid reaction of tPA at the thrombus makes it very difficult for a high concentration to be obtained there. The concentration at the thrombus is not a particularly helpful parameter though.

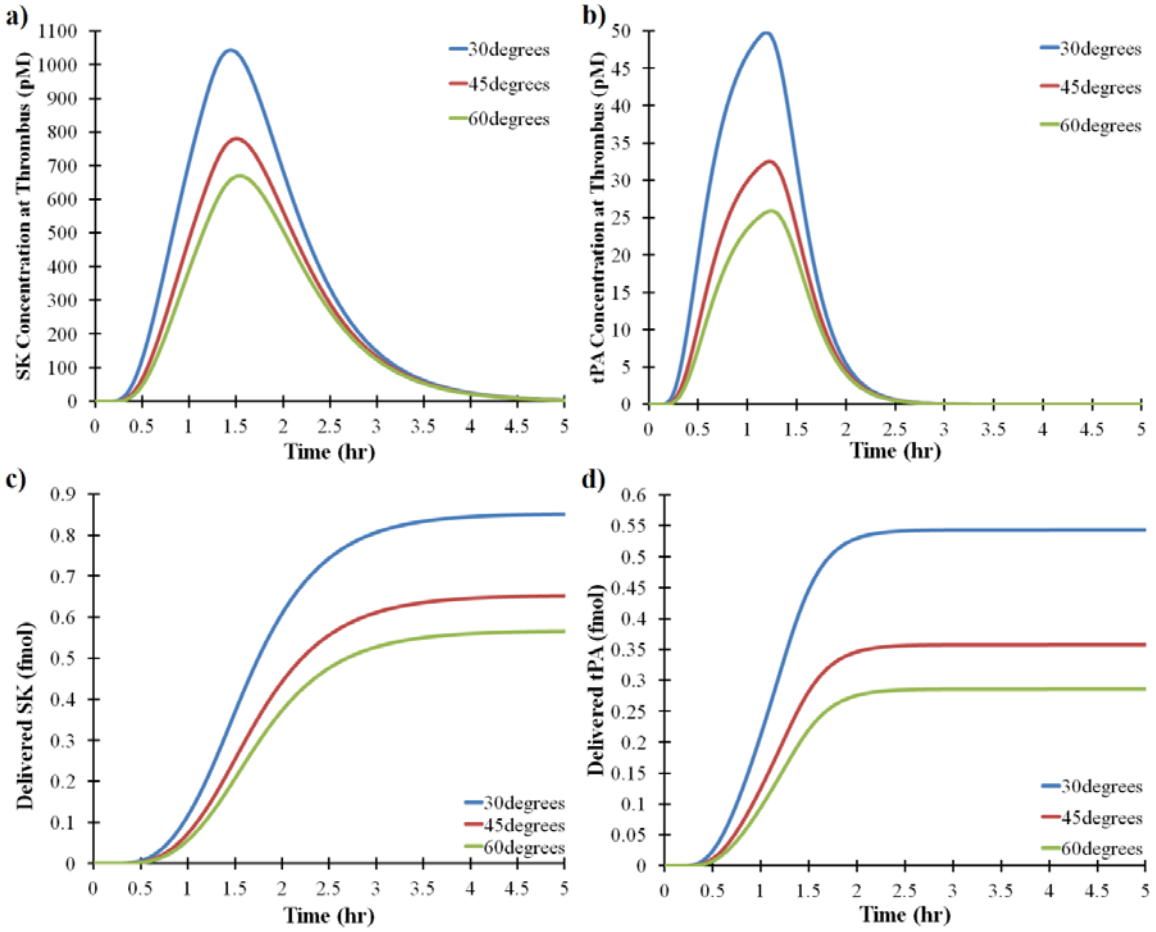

Figure 2.5: Transient plots showing the effect of changing the branch angle from 30° to 45° or 60° in the simulation and the time required for the thrombolytics to react at the thrombus. a) Concentration of streptokinase at the thrombus over time, b) concentration of tPA at the thrombus over time, c) cumulative amount of streptokinase that has reacted at the clot over time, d) cumulative amount of tPA that has reacted at the clot over time.

The cumulative amount of thrombolytic that has been delivered to the clot at any given time is a parameter of interest since it is proportional to the number of plasmin-fibrin reactions that have occurred at the clot under the assumption that any plasminogen activated in the bulk bloodstream is inhibited by α_2-antiplasmin before reaching the thrombus. Assuming the fibrin-bound plasminogen concentration in the thrombus is

constant, the local thrombolytic concentration is directly proportional to the flux and the number of moles of thrombolytic reacting at the clot at any given second. Integration of the latter value over time gives the cumulative number of moles of delivered thrombolytic. In plots of the cumulative amount of thrombolytic delivered, the time at which the maximum local clot concentration was obtained can be identified by the inflection point of the curve. The subsequent rapid decay in the concentration of tPA appears as a rapid transition to the final total amount of tPA delivered.

As θ increases from 30° to 45° to 60° the total amount of streptokinase delivered to the clot decreases (Figure 2.5c) as does the total amount of delivered tPA (Figure 2.5d). As the occluded vessel diameter is increased from 0.5mm to 0.75mm to 1mm, the total amount of streptokinase or tPA delivered increases following a power law relationship (Figure 2.6a-b). As the flow rate through the unblocked vessel is varied from 1mL/min to 2mL/min to 3mL/min, the total amount of thrombolytic delivered barely changes (Figure 2.6c-d). As the length of the occluded vessel increases from 0.25cm to 0.5cm to 0.75cm, the amount of delivered thrombolytic decays exponentially with increasing length (Figure 2.6e-f).

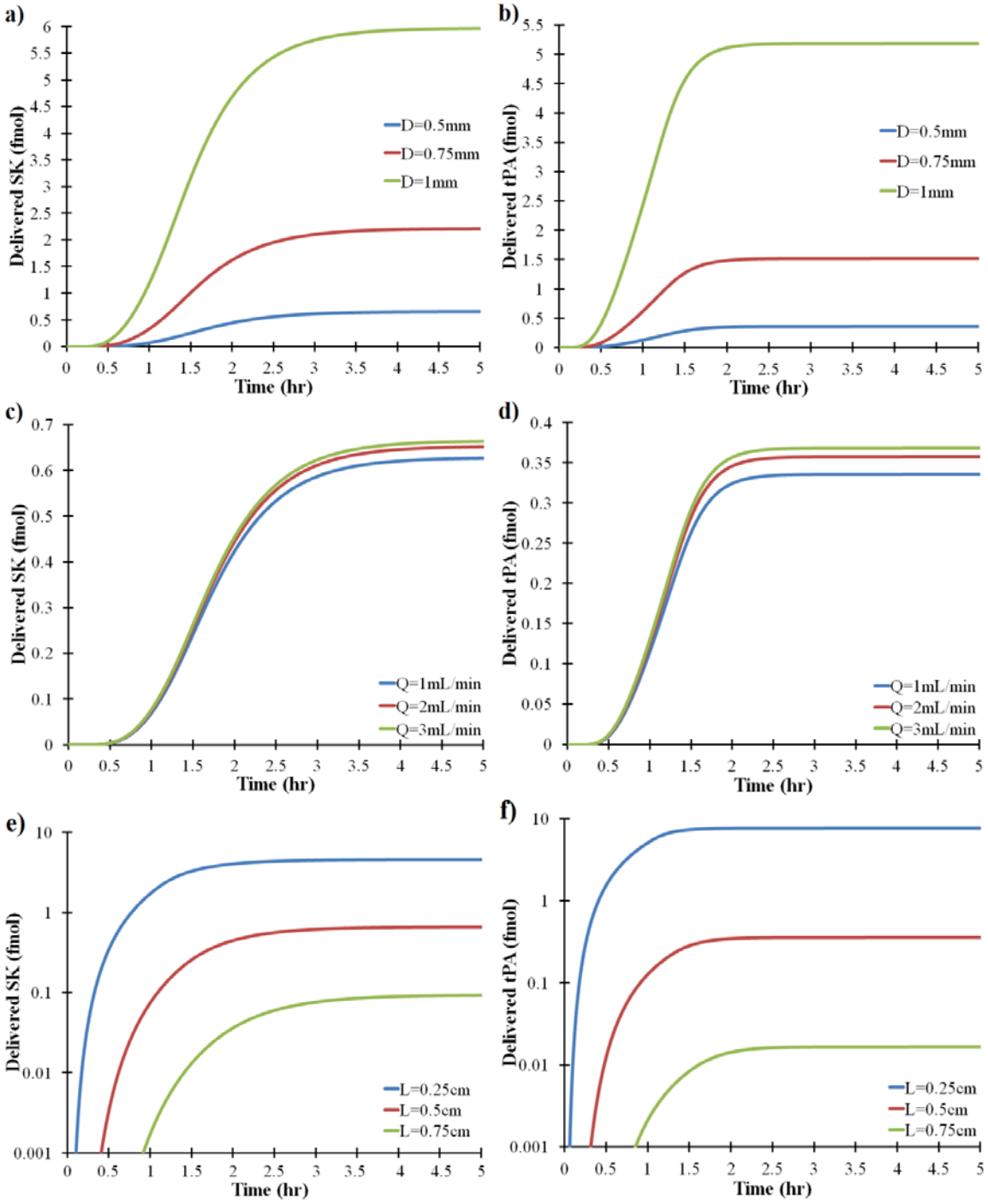

Figure 2.6: Transient plots comparing the effect of the diameter (a,b), the flow rate (c,d), and the length (e,f) on the cumulative amount of thrombolytic delivered to the thrombus over time when using SK (a,c,e) or tPA (b,d,f).

2.5 DISCUSSION AND CONCLUSIONS

The results show that the process of thrombolytic delivery to a clot in a completely blocked vessel is diffusion limited. After the thrombolytic enters the occluded vessel, it diffuses through the artery until it reacts with plasminogen. Since diffusion is a slow transport mechanism and the thrombolytic and plasminogen are continually reacting with each other, their concentrations decrease with distance along the occluded vessel. Thus, the minimum thrombolytic concentration occurs at the clot.

After one hour from the start of administration, the minimum concentration of tPA (0.03nM), which occurs at the thrombus, is even lower than that of streptokinase (0.48nM) because tPA reacts more rapidly than streptokinase both at the clot surface and in the bulk flow. A total of 0.0738fmol of streptokinase and 0.126fmol of tPA are delivered to the thrombus during the administration period. This accounts for only 11.3% of the total streptokinase that eventually reacts at the clot but 35.2% of the total tPA. The increase in local concentration at the clot with decreasing branch angle can be attributed to a slight increase in the distance over which convection transports the drug into the occluded vessel. In the case of decreasing the branch angle, this convective penetration of the blocked artery is improved because the blood and the thrombolytic it carries can deviate from the bulk flow in the unblocked artery by a smaller angle and therefore oppose the flow's inertia less. In addition, the convective penetration distance increases because the entrance to the clogged vessel ($D/\sin\theta$) becomes wider. In fact, the convective penetration distance is roughly $\sqrt{2}D/\sin\theta$. The resulting trend of increased thrombolytic delivery with decreased branch angle also suggests that the total thrombolytic delivered is proportional to $1/\sin\theta$, which is proportional to the width of the entrance to the occluded vessel. The proportionality constant relating $1/\sin\theta$ to the total thrombolytic delivered is approximately 0.34 for streptokinase and 0.31 for tPA.

The link between increasing occluded vessel diameter and increasing local thrombolytic concentration at the clot is again the increase in the width of the blocked artery's entrance leading to drastically improved convective penetration. Improved thrombolytic delivery naturally follows the increased thrombolytic concentration at the clot. The number of micromoles of streptokinase delivered is $20.275D^{3.181}$, and the number of micromoles of tPA delivered is $1655.3D^{3.841}$, where D has units of meters. Tripling the flow rate accounts for less than a six percent change in the total streptokinase delivered and less than a ten percent change in tPA delivered. This shows that the flow rate has a weak effect on the local clot concentration of the thrombolytic. When doubling the flow rate, the streptokinase delivered increases by four percent and the tPA delivered increases by 6.6 percent. Length is by far the most significant variable with the amount of delivered thrombolytic decaying exponentially with increasing length. The concentration profile of the drug remains nearly identical when the length of the occluded vessel is altered, so the length of the artery does little to affect the flow through it. The number of femtomoles of streptokinase delivered to the clot is $32.02e^{-778L}$, and the number of femtomoles of tPA delivered to the thrombus is $165.5e^{-1227L}$, where L has units of meters.

tPA and streptokinase behave quantitatively different since tPA has a greater fibrin specificity and a greater reaction rate both at the thrombus and in the bulk flow. Typically for the simulated cases, more thrombolytic is delivered to the clot if streptokinase is administered than if tPA were administered in large part because streptokinase reacts more slowly in the bulk bloodstream. However, this is not the case when the length of the occluded vessel is shortened to 0.25cm from the base case of 0.5cm. When the occluded vessel's length is 0.366cm and other variables are at their base values, the total amount of delivered thrombolytic should be 1.85fmol no matter

which drug is used. For vessel lengths shorter than about 0.366cm, more thrombolytic is delivered to the clot if tPA is used instead of streptokinase. This effect results from the delivered tPA being much more sensitive to *L* than delivered SK. In fact tPA is much more sensitive to all the system variables compared to streptokinase.

The diffusion-limited rate of transport and delivery in the occluded vessel, convective transport past the occluded vessel, and systemic reactions with plasminogen combined make it likely that only a small portion of the administered thrombolytic will actually react at the clot. In fact the results here suggest that often an insufficient amount of the drug is reaching the thrombus. Of the 0.30μmol of streptokinase administered by IV only about 0.65fmol (2.16×10^{-7} percent) are delivered to the thrombus under the base conditions with an occluded vessel length of 0.5cm. Of the 0.96μmol of tPA administered only 0.36fmol (3.7×10^{-8} percent) react at the clot for the same length. A shorter occluded vessel, 0.25cm long, yields better, but still undesirable, results: 1.52×10^{-6} percent for streptokinase and 8.02×10^{-7} percent. Interestingly, despite the much improved fibrin specificity of tPA, a greater fraction of the administered thrombolytic is delivered if streptokinase is used in lieu of tPA. Vastly improved fibrin specificity is unimportant if the reaction rate of the thrombolytic in the bulk blood plasma is already fast since the drug may never reach the clot site.

This diffusion-limited transport may be a primary reason that, even now, individuals suffering a stroke have about an 80 percent chance of death or disability [Kwon *et al.* (2004), Roger *et al.* (2012)]. The large scale trials by the European and European-Australasian Cooperative Acute Stroke Studies (ECASS I and II) and ATLANTIS (Alteplase Thrombolysis for Acute Noninterventional Therapy in Ischemic Stroke) of intravenously delivered alteplase, a recombinant tPA, found that its use for acute ischemic stroke treatment could not be definitively shown to be an improvement

over the use of a placebo [Donnan *et al.* (2003)]. The Third International Stroke Trial (IST-3), the largest scale-trial yet, was able to prove a very tiny improvement in the overall likelihood of surviving the stroke without disability if thrombolytic is administered within three hours of the stroke's onset. However, between three and six hours after the stroke, the majority of their data suggests that tPA actually diminishes those odds as well as the probability of surviving at all versus placebo [Wardlaw *et al.* (2012)]. In patients who are healthy enough, intra-arterial delivery directly into the occluded vessel, or even better at the clot site, would be extremely beneficial since it would avoid convective transport past the occluded vessel, systemic dilution and reaction of the thrombolytic, and decrease the diffusive length. Otherwise the effective use of thrombolytics remains elusive unless the mechanism of delivery is radically altered.

Chapter 3: General Model for Magnetically-Assisted Thrombolytic Delivery

3.1 INTRODUCTION

Inducing convective transport in dead-end pores is valuable for improving many processes. When reservoirs are waterflooded and subsequently re-flooded with alkali-surfactant-polymer solutions to displace and recover oil, a substantial amount of oil may be left behind, trapped within dead-end pores [Farajzadeh *et al.* (2013), Sedaghat *et al.* (2013)]. Convection of the flooding solution can lead to improved delivery of surfactants and alkalis to decrease interfacial tension or lead directly to convection of the oil. Both mechanisms would aid in removing the oil from the blocked pore. Similarly, pores can also trap environmental contaminants, like dense non-aqueous phase liquids, complicating subsurface remediation [Miller *et al.* (2000)]. Convection of the flushing medium can assist in the rapid cleanup of these contaminants. In ischemic stroke patients, delivering clot-busting thrombolytics to the site of the blood clot is time sensitive and slow diffusion-limited delivery of the drug through the length of the blocked artery is an issue [Clements and Bonnecaze (2013), Donnan *et al.* (2003)]. Inducing convection within the blocked artery can speed delivery of the thrombolytic to the clot.

There are many different methods of inducing fluid flow in general, ranging from the classical, such as pressure and gravity, to thermally induced buoyancy changes, which is popular for processes involving gases on a large scale, like building ventilation [Gan (2006)]. The more difficult issue is finding methods of generating fluid flow that can be applied to a range of systems that do not have separate inlets and outlets, in addition to being small-scale and typically difficult to access directly, for example being underground or inside the human body. Electro-osmosis is currently popular for use in

oil recovery since ions are plentiful in crude oils permitting a strong driving force [Chen S. *et al.* (2014)]. The use of acoustic vibrations is currently seeing increased interest as it may, in addition to inducing fluid flow [Sun and Guo (2007)], also bypass the issue by destroying the blockage, as in sonothrombolysis [Chen X. *et al.* (2014)].

Magnetically-driven flow in blocked pores via a method invented by Pulse Therapeutics is explored here. Ferroparticles are added to the fluid medium. A magnetic field is applied to the region of interest and in response the ferroparticles aggregate. In order to subsequently induce flow, the field is rotated, creating torque on the aggregates leading to their rotation within the bulk fluid. The rotating magnetic field must also have some gradient in order to establish a concentration gradient for the ferroparticle aggregates so that directional flow is possible within a blocked vessel.

Demetriades (1958) explored the effect of applying an electric field to rigid particles already immersed in a shear flow. The orientation of the particles was solved for with the electric field set normal to the shear flow. Mason co-wrote a series of articles on particle behavior when placed under the influence of both a shear field and an electric field, including one with Allan (1962) in which the orientation of a rigid rod is briefly presented for the case of zero shear flow. Shine and Armstrong (1987) considered the transient rotation of an axisymmetric ellipsoid in response to a constant, uniform DC magnetic field without the initial shear flow. In addition to the magnetic and hydrodynamic torques contributing to the net torque on the ellipsoid, they also focused on the relationship between the applied magnetic field and the magnetization of the ellipsoid. This included finding a perturbation solution for ellipsoids near their saturation magnetization due to a high strength magnetic field. Horvath and Kopcansky (1993) developed a qualitative model for the rotation of a magnetic dimer in the presence of a rotating magnetic field and performed stability analyses on it. They noted the existence

of a critical parameter above which the dimer would rotate in sync with the field, while below it rotation would be asynchronous. Their analysis, however, does not extend to investigating the influence of the rotating dimer on the surrounding fluid medium.

The magnetic body couple and magnetic body force acting on the ferro-aggregates must be noted when considering the stresses on the fluid continuum. The body couple is the divergence of the anti-symmetric stress, which is defined by the torques acting on the aggregates. At steady state, the magnetic torque, controlled by the cross-product of the magnetization of the aggregates and the applied magnetic field, is balanced by the hydrodynamic torque. The body force is the dot product of the magnetization of the aggregates and the gradient of the magnetic field. The H-field gradient is here considered to be only of sufficient strength to establish the concentration gradient, while contributing minimally to the body force.

3.2 MODEL DESCRIPTION

In order to predict the fluid velocity profile of a dilute suspension of ferroparticles in a blocked channel when subjected to a rotating magnetic field and to better understand the physics leading to convective flow, a model was developed to describe both the particle dynamics and the flow field. The geometry of the system was set up as shown in Figure 3.1, where $\mathscr{M}$ is the magnetic dipole moment of the magnetic field source.

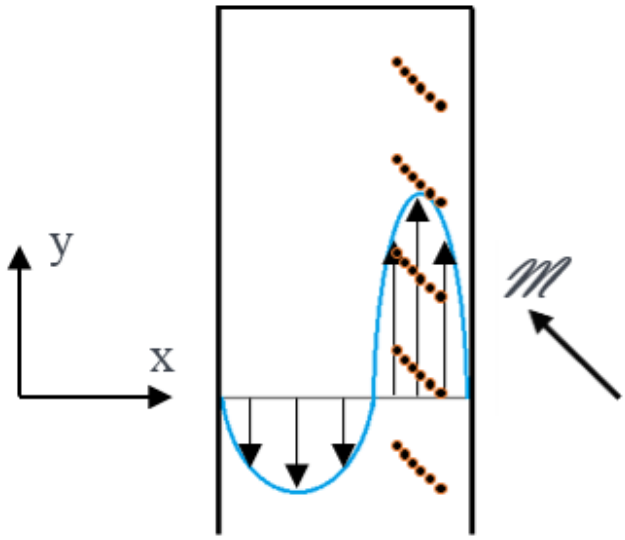

Figure 3.1: Schematic of model system showing particle aggregates, potential flow field, and rotating magnetic field source.

In order to reduce the complexity of the system, the model assumes that the spherical ferroparticles have already aggregated into slender structures in response to the presence of the magnetic field and that those aggregates have already positioned themselves within the channel according to the strength of the field's gradient. Each slender aggregate will be treated as a single, larger, ellipsoidal particle.

The model equations describing the suspension dynamics include conservation of mass (3.1) and linear momentum (3.2), given by

$$\nabla \cdot \mathbf{u} = 0\,, \tag{3.1}$$

$$\rho \frac{D\mathbf{u}}{Dt} = -\nabla p + \eta \nabla^2 \mathbf{u} + \nabla \cdot \mathbf{T}_A + n\mu_0 V \mathbf{m} \cdot \nabla \mathbf{h}\,, \tag{3.2}$$

where **u** is the velocity vector, ρ is the fluid density, t is time, p is pressure, and η is fluid viscosity. $n\mu_0 V\mathbf{m}\cdot\nabla\mathbf{h}$ is the magnetic body force, where n is the local ferro-aggregate number density, μ_0 is the magnetic permeability in a vacuum, V is the aggregate volume, **m** is the magnetization of the aggregates, and **h** is the applied magnetic field. $\mathbf{T}_A$ is the

anti-symmetric stress tensor resulting from the body couple of the applied magnetic field acting on the magnetized aggregates. It is given by [Rosensweig (1985)]

$$\mathbf{T}_A = n\begin{bmatrix} 0 & T_{M3} & -T_{M2} \\ -T_{M3} & 0 & T_{M1} \\ T_{M2} & -T_{M1} & 0 \end{bmatrix}. \tag{3.3}$$

The ferro-aggregate number density is described by the equation:

$$\frac{\partial n}{\partial t} + \mathbf{u_g} \cdot \nabla n = \nabla \cdot \left(\mathbf{d} \cdot \nabla n \right), \tag{3.4}$$

where $\mathbf{u_g}$ is the particle velocity across the channel due to the magnetic field gradient and $\mathbf{d}$ is the effective hydrodynamic diffusion tensor of the aggregates.

The magnetic torque $\mathbf{T}_M$ on the aggregates must be found to specify $\mathbf{T_A}$, thereby linking the suspension dynamics with the particle dynamics. The magnetic component of the torque on the aggregates is given by

$$\mathbf{T}_M = \mu_0 V \left(\mathbf{m} \times \mathbf{h} \right). \tag{3.5}$$

The magnetization of the aggregates is described by

$$\mathbf{m} = \alpha_L \mathbf{pp} \cdot \mathbf{h} + \alpha_T \mathbf{h}, \tag{3.6}$$

where $\mathbf{p}$ is the director describing the orientation of the aggregates, $\alpha_L = (2/3)(L/a)^2 \left[\ln(2L/a) - 1 \right]^{-1}$ and $\alpha_T = 2$ [Rocha and Acrivos (1974)]. L is the length of the semi-major axis and a is the length of the semi-minor axis.

The hydrodynamic torque on the aggregates is given by [Kim and Karrila (1991)]

$$\mathbf{T}_H = 8\pi\eta L^3 \left(\left[X^C \mathbf{pp} + Y^C \left(\mathbf{I} - \mathbf{pp} \right) \right] \left(\boldsymbol{\omega} - \boldsymbol{\omega}^\infty \right) + Y^H \left[\mathbf{p} \times \left(\mathbf{e}^\infty \cdot \mathbf{p} \right) \right] \right), \tag{3.7}$$

where $\boldsymbol{\omega}$ is the angular velocity of the aggregates, $\boldsymbol{\omega}^\infty$ is the angular velocity of the bulk fluid, and $\mathbf{e}^\infty$ is the strain rate due to the flow. The parameters X^C, Y^C, and Y^H are known

functions of aggregate eccentricity, $\varepsilon = \sqrt{L^2 - a^2}/L$, and are listed in Appendix B [Kim and Karrila (1991)].

Following Jeffery (1922) and Hinch and Leal (1979), the angular velocity of the aggregates can be expressed via Euler angles as a function of aggregate orientation so

$$\frac{d\mathbf{p}}{dt} = \mathbf{K}(\mathbf{p}) \cdot \boldsymbol{\omega} . \tag{3.8}$$

See Appendix B for **K(p)**.

Setting the magnetic and hydrodynamic torques equal to one another results in a dynamic equation for the orientation of the aggregates:

$$\frac{d\mathbf{p}}{dt} = \mathbf{K} \cdot \left[\boldsymbol{\omega}^{\infty} + \left[X^C \mathbf{pp} + Y^C (\mathbf{I} - \mathbf{pp}) \right]^{-1} \begin{pmatrix} \frac{\mu_0 V}{8\pi\eta L^3} \left(\alpha_L \mathbf{pp} \cdot \mathbf{h} + \alpha_T \mathbf{h} \right) \times \mathbf{h} \\ -Y^H \left[\mathbf{p} \times \left(\mathbf{e}^{\infty} \cdot \mathbf{p} \right) \right] \end{pmatrix} \right]. \tag{3.9}$$

3.3 NON-DIMENSIONALIZATION

The first step in analyzing these equations is to appropriately non-dimensionalize them. To that end, dimensionless time and distance have been defined as $\tau = \Omega t$ and $X = x/d$, respectively, where Ω is the rotation rate of the magnetic field and d is the channel diameter. Similarly, aggregate rotation rate is non-dimensionalized according to $\boldsymbol{\Omega} = \boldsymbol{\omega}/\Omega$. The dimensionless magnetic field and magnetization are $\mathbf{H} = \mathbf{h}/H$ and $\mathbf{M} = \mathbf{m}/\alpha_L H$, respectively, where H is the magnetic field strength. Dimensionless concentration is represented by $N = nV/\Phi$, where Φ is the average volume fraction of the aggregates, and dimensionless torque is represented by $G_M = T_M/\eta L^3 \Omega$.

Based upon the following analysis, a characteristic velocity of $u_c = L^3 \Omega d\, \Phi/V$ was chosen, making the dimensionless velocity $\mathbf{U} = \mathbf{u}V/\Phi L^3 \Omega d$. Accordingly, the characteristic pressure is defined as $p_c = \eta u_c/d$, while the characteristic diffusion

coefficient is defined as $D_c = u_c d$. Finally, the characteristic values of the local flow rotation rate and strain rate are $\omega_c^\infty = e_c^\infty = u_c / d$.

Following these definitions, non-dimensionalizing equations (3.1-3.5) gives

$$\nabla \cdot \mathbf{U} = 0, \tag{3.10}$$

$$\frac{\rho}{\eta} d^2 \Omega \frac{D\mathbf{U}}{D\tau} = -\nabla P + \nabla^2 \mathbf{U} + \nabla \cdot \mathbf{G}_A + \frac{\mu_0 V \alpha_L H^2}{\eta L^3 \Omega} N \mathbf{M} \cdot \nabla \mathbf{H}, \tag{3.11}$$

$$\mathbf{G}_A = N \begin{bmatrix} 0 & G_{M3} & -G_{M2} \\ -G_{M3} & 0 & G_{M1} \\ G_{M2} & -G_{M1} & 0 \end{bmatrix}, \tag{3.12}$$

$$\frac{V}{\Phi L^3} \frac{\partial N}{\partial \tau} + \mathbf{U}_\mathbf{g} \cdot \nabla N = \nabla \cdot \left(\mathbf{D} \cdot \nabla N \right), \tag{3.13}$$

$$\mathbf{G}_M = \mathbf{M} \times \mathbf{H} \left(\frac{\mu_0 V \alpha_L H^2}{\eta L^3 \Omega} \right). \tag{3.14}$$

Since the magnitude of $\mathbf{m} \times \mathbf{h} = MH \sin\theta$, where θ is the offset angle between the H-field and magnetization vectors, the magnitude of $\mathbf{M} \times \mathbf{H} \approx \sin\theta$.

Non-dimensionalizing equations (3.6-3.7) gives

$$\mathbf{M} = \mathbf{pp} \cdot \mathbf{H} + \frac{\alpha_T}{\alpha_L} \mathbf{H}, \tag{3.15}$$

$$\mathbf{G}_H = 8\pi \left(\left[X^C \mathbf{pp} + Y^C \left(\mathbf{I} - \mathbf{pp} \right) \right] \left(\mathbf{\Omega} - \frac{\Phi L^3}{V} \mathbf{\Omega}^\infty \right) + \frac{\Phi L^3}{V} Y^H \left[\mathbf{p} \times \left(\mathbf{E}^\infty \cdot \mathbf{p} \right) \right] \right). \tag{3.16}$$

Likewise, the aggregate orientation equation (3.9) becomes

$$\frac{d\mathbf{p}}{d\tau} = \mathbf{K} \cdot \frac{\Phi L^3}{V} \mathbf{\Omega}^\infty + \mathbf{K} \cdot \left[X^C \mathbf{pp} + Y^C \left(\mathbf{I} - \mathbf{pp} \right) \right]^{-1} \left(\begin{array}{l} \dfrac{\mu_0 V \alpha_L H^2}{8\pi \eta L^3 \Omega} \left[\mathbf{pp} \cdot \mathbf{H} + \dfrac{\alpha_T}{\alpha_L} \mathbf{H} \right] \times \mathbf{H} \\ -\dfrac{\Phi L^3}{V} Y^H \left[\mathbf{p} \times \left(\mathbf{E}^\infty \cdot \mathbf{p} \right) \right] \end{array} \right). \tag{3.17}$$

Setting the magnetic and hydrodynamic torques equal to one another gives

$$\sin\theta = \frac{8\pi\eta L^3\Omega}{\mu_0 V \alpha_L H^2}\left(\begin{array}{l}\left[X^C\mathbf{pp}+Y^C\left(\mathbf{I}-\mathbf{pp}\right)\right]\left(\boldsymbol{\Omega}-\dfrac{\Phi L^3}{V}\boldsymbol{\Omega}^\infty\right)\\ +\dfrac{\Phi L^3}{V}Y^H\left[\mathbf{p}\times\left(\mathbf{E}^\infty\cdot\mathbf{p}\right)\right]\end{array}\right). \tag{3.18}$$

As such,

$$\sin\theta \propto \frac{\eta L^3 Y^C \Omega}{\mu_0 V \alpha_L H^2}. \tag{3.19}$$

3.4 Discussion and Conclusions

Based upon these non-dimensionalizations, several conclusions can be drawn about the behavior of the magnetically-induced velocity. The velocity scales proportionally to both the volume fraction of the aggregates and the rotation rate of the magnetic field. Similarly, since the characteristic velocity is also proportional to L^3/V, assuming ellipsoidal aggregates, the magnetically-induced velocity scales proportionally with L^2/a^2, or the square of the aspect ratio of the aggregates.

Interestingly, velocity is seen to be independent of the magnetic field strength. This independence is only possible due to the assumption that the aggregates are of fixed length and aspect ratio. When this assumption is eliminated in Chapter 6, the velocity will be shown to be influenced by the H-field strength. With the aggregates of fixed size as in Chapters 4 and 5, however, torque is independent of the magnitude of the magnetic field. This occurs because the torque is explicitly dependent upon the product of the magnetic field strength, the magnetization of the aggregates, and the sine of the offset angle between the two. Since the magnetization of the aggregates is proportional to H and the sine of the offset angle is inversely proportional to H^2, the magnetic field strength dependence of the torque is canceled out.

Since H is the magnetic field strength applied to the region of interest and not the magnetic field strength at the source, changing the location of the magnetic field source as done in Chapter 5 will not impact the preceding non-dimensionalizations and their corresponding scaling arguments.

Chapter 4: 2D Model with Fixed Size Aggregates in a Non-Displaced Magnetic Field

4.1 EQUATIONS

Following the equations from Chapter 3, consider a flow that has been magnetically induced from quiescence in a two-dimensional channel where inertia, magnetic body force, strain rate, and the angular velocity of the bulk fluid are negligible. Also, within the region of interest, the magnetic field is assumed to be spatially constant, varying only with time, while the local aggregate number density varies only with x-position across the channel. In addition, the magnetic field source is assumed to be located at the channel in the region of interest. As noted previously, the slender aggregates will be treated like larger individual ellipsoidal particles of constant, fixed aspect ratio and length.

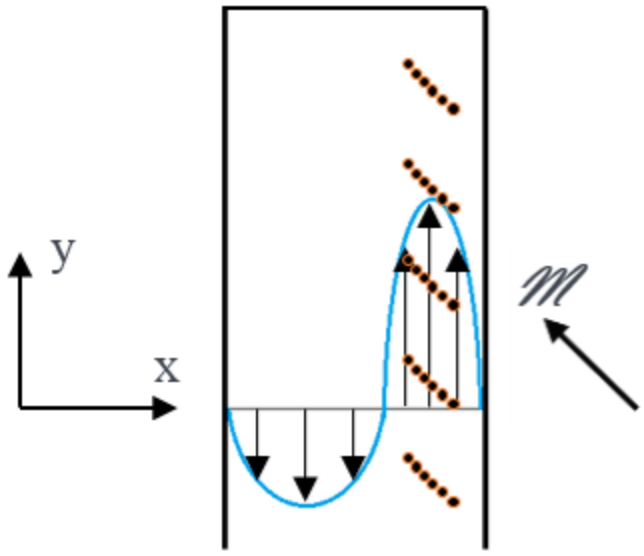

Figure 4.1: Schematic of model system showing particle aggregates, potential flow field, and rotating magnetic field source.

Using the dimensionless equations derived in Chapter 3, the flow is described by

$$\frac{\partial U_x}{\partial X}+\frac{\partial U_y}{\partial Y}=0, \tag{4.1}$$

$$-\frac{\partial P}{\partial X}+\frac{\partial^2 U_x}{\partial X^2}+\frac{\partial^2 U_x}{\partial Y^2}=0, \tag{4.2}$$

$$-\frac{\partial P}{\partial Y}+\frac{\partial^2 U_y}{\partial X^2}+\frac{\partial^2 U_y}{\partial Y^2}+\frac{8\pi Y^C}{\sin\theta}\frac{\partial N}{\partial X}\begin{pmatrix}\left(\cos^2\phi H_x+\sin\phi\cos\phi H_y\right)H_y\\-\left(\sin\phi\cos\phi H_x+\sin^2\phi H_y\right)H_x\end{pmatrix}=0, \tag{4.3}$$

The dynamics of a rod in the flow are given by

$$\frac{dp_x}{d\tau}=-\frac{\sin\phi}{\sin\theta}\left[\left(\cos^2\phi H_x+\sin\phi\cos\phi H_y\right)H_y-\left(\sin\phi\cos\phi H_x+\sin^2\phi H_y\right)H_x\right], \tag{4.4}$$

$$\frac{dp_y}{d\tau}=\frac{\cos\phi}{\sin\theta}\left[\left(\cos^2\phi H_x+\sin\phi\cos\phi H_y\right)H_y-\left(\sin\phi\cos\phi H_x+\sin^2\phi H_y\right)H_x\right], \tag{4.5}$$

where $\phi=\tan^{-1}\left(p_y/p_x\right)$ is the orientation angle of the ferro-aggregate. As such, $p_y=\sin\phi$ and $p_x=\cos\phi$.

The *x* and *y* components of the dimensionless magnetic field are assumed to be given by $H_x=\cos(\tau)$ and $H_y=\sin(\tau)$. It is further assumed that the fluid flow velocity across the channel is negligible and that the bulk flow velocity u_y does not change with y-position along the channel. In this case the equations of motion simplify to become

$$\frac{\partial P}{\partial X}=0, \tag{4.6}$$

$$-\frac{\partial P}{\partial Y}+\frac{\partial^2 U_y}{\partial X^2}+\frac{4\pi Y^C}{\sin\theta}\frac{\partial N}{\partial X}\sin\left(2\tau-2\phi\right)=0, \tag{4.7}$$

$$\frac{dp_x}{d\tau}=-\frac{\sin\phi}{2\sin\theta}\sin\left(2\tau-2\phi\right), \tag{4.8}$$

$$\frac{dp_y}{d\tau}=\frac{\cos\phi}{2\sin\theta}\sin\left(2\tau-2\phi\right). \tag{4.9}$$

The offset angle between the H-field orientation and the orientation of the aggregates is $\theta = \tau - \phi$. For sufficiently strong magnetic fields, the offset angle will be constant, so aggregate rotation rate $\left(d\phi/dt\right)$ will match the H-field rotation rate (Ω). Therefore, $d\phi/d\tau = 1$, and since $dp/d\tau = \left(dp/d\phi\right)\left(d\phi/d\tau\right)$, it follows that $dp/d\tau = dp/d\phi$. $dp_x/d\phi = -\sin\phi$ and $dp_y/d\phi = \cos\phi$, so $\sin\left(2\tau - 2\phi\right)/2\sin\theta = 1$, or $\sin\left(2\theta\right) = 2\sin\theta$. In the case of a small offset angle, as would exist in the presence of a strong magnetic field, this equation is valid as the approximation $\sin\theta = \theta$ holds so $\sin\left(2\theta\right) = 2\theta$ and $2\theta = 2\sin\theta$. Equations (4.7-4.9) then become

$$-\frac{\partial P}{\partial Y} + \frac{\partial^2 U_y}{\partial X^2} + 8\pi Y^C \frac{\partial N}{\partial X} = 0\,, \tag{4.10}$$

$$\frac{dp_x}{d\tau} = \frac{dp_x}{d\phi} = -\sin\phi\,, \tag{4.11}$$

$$\frac{dp_y}{d\tau} = \frac{dp_y}{d\phi} = \cos\phi\,. \tag{4.12}$$

Equation (4.10) can be re-arranged to give a differential equation for the flow velocity:

$$\frac{\partial^2 U_y}{\partial X^2} = \frac{\partial P}{\partial Y} - 8\pi Y^C \frac{\partial N}{\partial X}\,. \tag{4.13}$$

Integrating yields

$$\frac{\partial U_y}{\partial X} = X\frac{\partial P}{\partial Y} - 8\pi Y^C N + C_1\,, \tag{4.14}$$

$$U_y = \frac{X^2}{2}\frac{\partial P}{\partial Y} - 8\pi Y^C \int_0^X N\mathrm{d}\psi + C_1 X + C_2\,, \tag{4.15}$$

where ψ is simply being used as a variable of integration in place of X.

Applying the no-slip ($U_y = 0$) boundary condition at $X = 0$ gives

$$C_2 = 0\,. \tag{4.16}$$

Applying the no-slip boundary condition at $X = 1$ and noting that $\int_0^1 N dX = 1$ gives

$$C_1 = 8\pi Y^C - \frac{1}{2}\frac{\partial P}{\partial Y}. \tag{4.17}$$

Substituting the values of C_1 and C_2 into equation (4.15) yields

$$U_y = \frac{\left(X^2 - X\right)}{2}\frac{\partial P}{\partial Y} + 8\pi Y^C \left(X - \int_0^X N \mathrm{d}\psi\right). \tag{4.18}$$

In an unblocked channel, the pressure gradient vanishes giving an expression for the magnetically-driven flow velocity:

$$U_m = 8\pi Y^C \left(X - \int_0^X N \mathrm{d}\psi\right). \tag{4.19}$$

In a blocked channel, the spatially-averaged net velocity must be zero with the average magnetically-driven and pressure-driven flow rates cancelling one another. The pressure gradient is then given by

$$\frac{\partial P}{\partial Y} = 48\pi Y^C \left[1 - 2\int_0^1 \left(\int_0^X N \mathrm{d}\psi\right) \mathrm{d}X\right]. \tag{4.20}$$

Inserting the solution for the pressure gradient into the expression for the net flow velocity gives

$$U_y = 8\pi Y^C \left[3X^2 - 2X - \int_0^X N \mathrm{d}X - 6\left(X^2 - X\right)\int_0^1 \left(\int_0^X N \mathrm{d}\psi\right) \mathrm{d}X\right]. \tag{4.21}$$

In order to evaluate the flow field in equation (4.21), the concentration field across the channel must be obtained. To do so, it is assumed that a balance exists between the force pushing the aggregates toward the wall at a velocity of U_g as a result of the magnetic field gradient and the hydrodynamic diffusion D, diffusing the aggregates away from the wall. The constant $\beta = U_g / D$, a cross-flow Peclet number, is used to quantify the relative transport mechanisms which govern the concentration profile of the

aggregates. The concentration profile would also be expected to be exponential with respect to channel position and satisfy equation (3.13).

$$\frac{V}{\Phi L^3}\frac{\partial N}{\partial \tau} + \mathbf{U_g}\cdot\nabla N = \nabla\cdot\left(\mathbf{D}\cdot\nabla N\right) \tag{3.13}$$

The channel walls are impermeable to the ferroparticles, leading to the boundary condition of no flux through the channel wall: $U_g N - D\left(\partial N/\partial X\right)\big|_{X=1} = 0$. The constraint on the average concentration in the channel can also be used as the second boundary condition: $\int_0^1 N dX = 1$.

Satisfying those conditions yields an expression for the concentration:

$$N = \beta\frac{\exp\left(\beta X\right)}{\exp\left(\beta\right)-1}. \tag{4.22}$$

Utilizing this expression for the concentration gives improved expressions for the magnetically-induced and pressure-induced velocities:

$$U_m = 8\pi Y^C\left[X - \frac{\exp\left(\beta X\right)-1}{\exp\left(\beta\right)-1}\right], \tag{4.23}$$

$$U_p = 24\pi Y^C\left[1-\frac{2}{\beta}+\frac{2}{\exp\left(\beta\right)-1}\right]\left(X^2 - X\right). \tag{4.24}$$

4.2 PARTICLE DYNAMICS

4.2.1 Torque

Computational simulation of the preceding equations gives further insight into the particle dynamics of the process and its resulting flow field.

In order to better understand the rotation of the aggregates, the time-averaged torque which causes that rotation is plotted against the applied magnetic field strength as shown in Figure 4.2. From that plot, a critical threshold strength becomes apparent.

Above it, there is significant torque on the aggregates with dimensional scaling of $\eta L^3 \Omega$, but below it the torque rapidly drops to zero as if no magnetic field was being applied at all. The value of this critical field strength was found from the simulation results to coincide with

$$H_{crit} = \sqrt{\frac{8\eta L^3 Y^C \Omega}{\mu_0 V \alpha_L}}. \tag{4.25}$$

This value agrees with the scaling obtained by substituting the maximum value of sin(θ) possible, 1, into equation (3.19) and re-arranging to solve for *H*.

The critical magnetic field strength is a function of viscosity, aggregate geometry, and field rotation rate. Of these parameters, only field rotation rate can be directly modified. Re-organizing equation (4.25), a critical magnetic field rotation rate could be defined for a given magnetic field strength.

$$\Omega_{crit} = \frac{\mu_0 V \alpha_L H^2}{8\eta L^3 Y^C} \tag{4.26}$$

Since the critical H-field magnitude is proportional to the square root of the field rotation rate, the critical H-field rotation rate is proportional to the square of the field magnitude. The existence of such a critical magnetic field frequency has been experimentally verified by Helgesen, Pieranski, and Skjeltorp (1990). They noted that as field frequency decreased the rotation of an affected bound pair of magnetic holes changed from a smooth steady state to small, local oscillations.

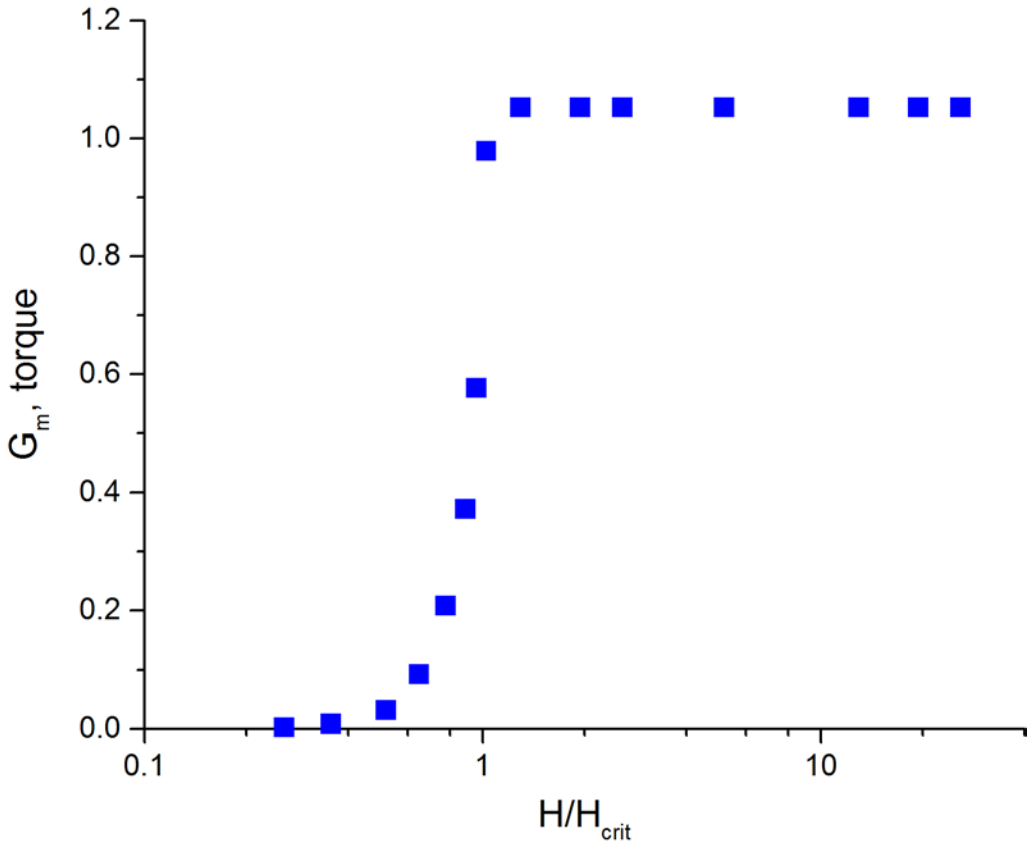

Figure 4.2: Dimensionless torque on aggregates when subjected to magnetic fields of various amplitudes.

4.2.2 Orientation Angle

Figure 4.3 tracks the rotation of the aggregates, plotting their orientation angle over time, for three different cases: above, at, and below the critical magnetic field amplitude. An initial condition of $\phi = 0$ is used. When the applied magnetic field strength is greater than the critical H-field strength, the aggregates rotate in sync with the field with very little offset. When the applied field is weaker than the critical field, aggregate rotation is insignificant. Around the threshold magnitude, the aggregates still rotate primarily in one direction, but net aggregate rotation is much slower and bears little to no resemblance to the field rotation.

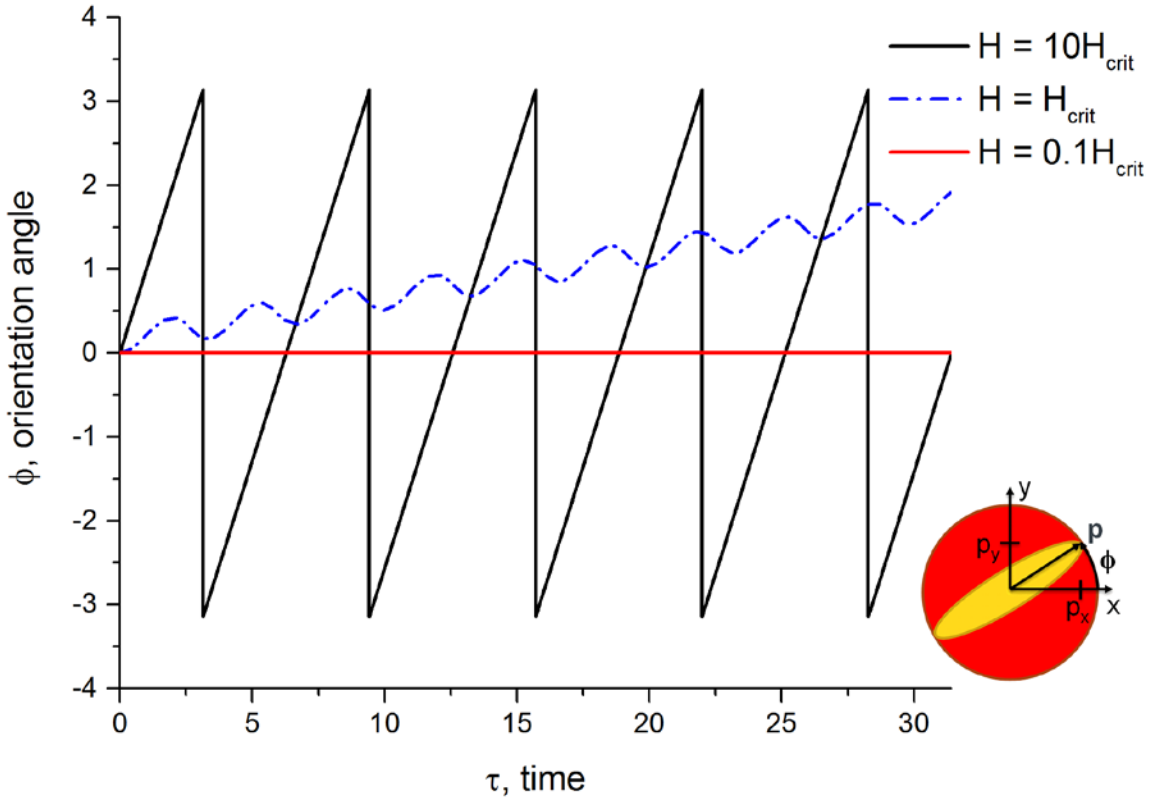

Figure 4.3: Orientation angle of the aggregates over dimensionless time for 5Hz magnetic fields above, at, and below the critical field strength. Inset schematic of orientation angle in the x-y plane and relative to an aggregate director.

4.2.3 Offset Angle

Alternatively, this information can be demonstrated by plotting the time-averaged offset angle between the orientation of the aggregates and the H-field orientation against the magnetic field strength as shown in Figure 4.4. Above and near the critical field amplitude, the data fit well with the expression

$$\theta = \frac{8\eta L^3 Y^C \Omega}{\mu_0 V \alpha_L H^2}. \tag{4.27}$$

Small average offset angles, which deviate from this equation, are obtained for weak magnetic fields below the threshold magnitude because the aggregates have

essentially stopped moving and offset angle is bound between $-\pi$ and π. As such, the times when aggregate offset is negative cancel out those when it is positive.

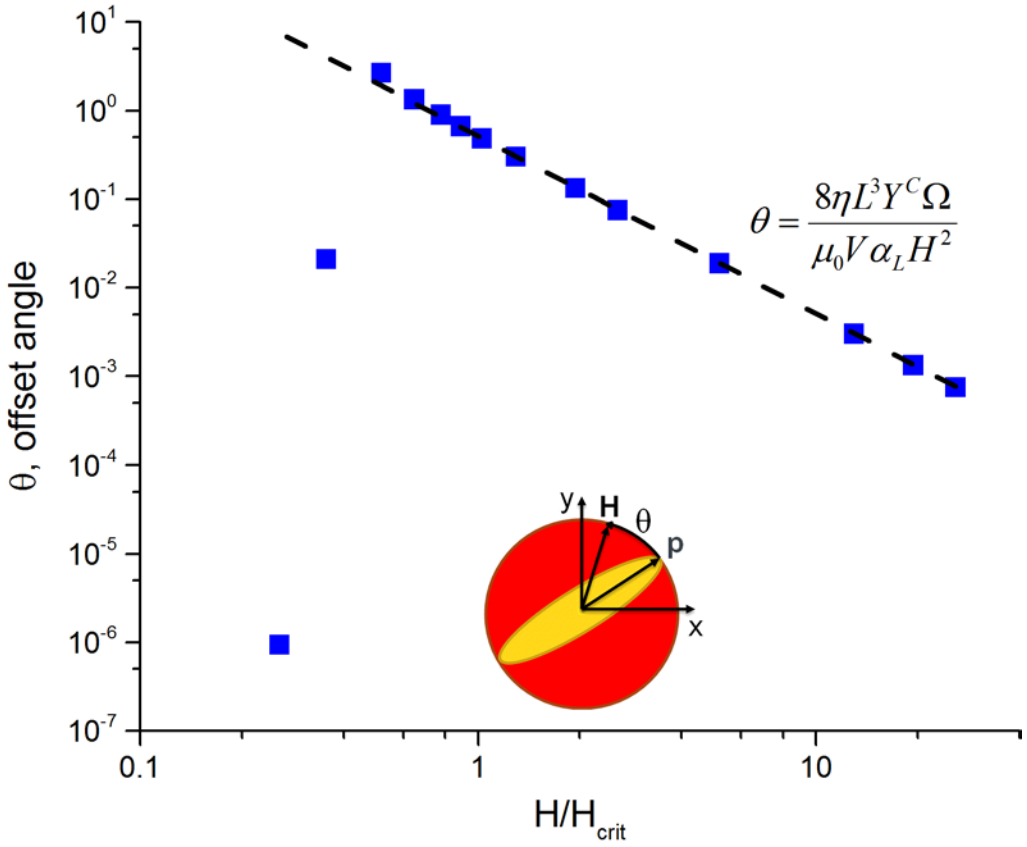

Figure 4.4: Offset angle of the aggregates from the magnetic field when subjected to magnetic fields of various amplitudes. Inset schematic of offset angle in the x-y plane and relative to the H-field vector and an aggregate director.

4.3 FLUID FLOW

4.3.1 Magnetically-Driven Velocity Profile

The particle dynamics induce fluid flow within the channel, so the critical field strength, which plays such an important role in those dynamics, is also an essential parameter of the fluid velocity profile. Figure 4.5a plots the dimensionless magnetically-

induced velocity profile across the channel above, at, and below the critical magnetic field strength for a 5 Hz applied magnetic field and a particular β of 75, while Figure 4.5b does the same for β = 7.5. Figures 4.5c-d plot the dimensional magnetically-induced velocity profile across the channel at different frequencies above the critical threshold for β = 75 and β = 7.5.

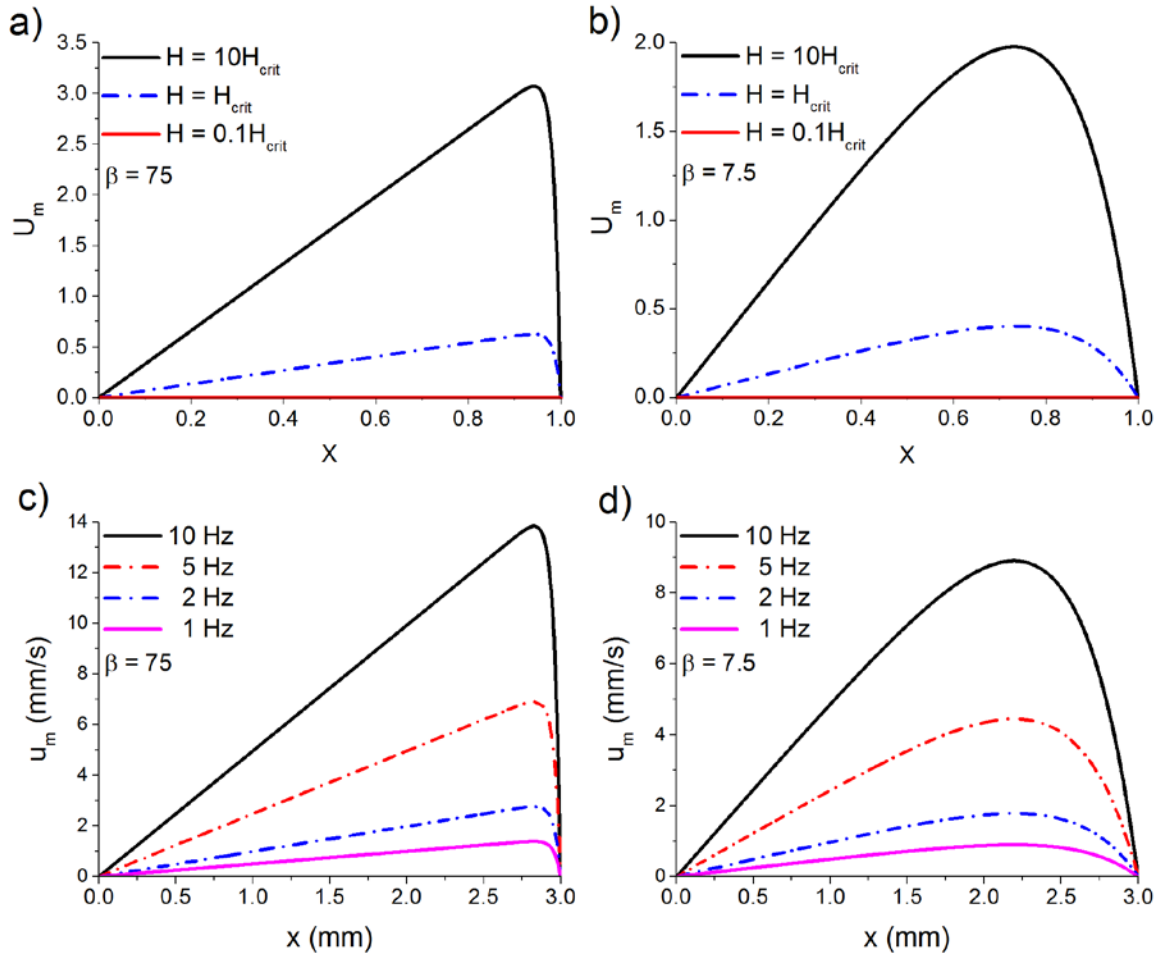

Figure 4.5: Dimensionless velocity profiles above, at, and below the magnetic field's critical threshold at 5Hz with (a) β = 75 and (b) β = 7.5. Dimensional velocity profiles above the critical magnetic field strength by a factor of 10 at different frequencies for (c) β = 75 and (d) β = 7.5.

The greatest velocities are induced above the critical H-field amplitude since the aggregates are rotating the fastest, while in the absence of rotation below the threshold no flow is induced. This also explains why increased magnetic field rotation rate leads to increased fluid velocity. Note that Figures 4.5c-d are shown dimensionally because the field rotation rate is a parameter of the characteristic velocity. If plotted non-dimensionally, the different curves would collapse onto the single line shown for $H = 10H_{crit}$ for the corresponding β in Figures 4.5a-b.

While the amplitude and rotation rate of the magnetic field affect the magnitude of the flow field, β influences the shape of the flow field. β directly controls the shape of the concentration profile, relating the magnetic body force and hydrodynamic diffusion acting on the particles. For high β values, the particles are very heavily concentrated against one wall of the channel, and this leads to an elevated maximum velocity very close to that wall. As the value of β decreases, the peak concentration decreases. This translates into a decreased peak velocity closer to the middle of the channel.

4.3.2 Average Velocity and Magnetic Field Rotation Rate

The dimensional average magnetically-induced velocity is plotted against the applied magnetic field frequency above, at, and below the critical H-field strength for $\beta = 75$ and $\beta = 7.5$ in Figures 4.6a-b. As depicted in Figure 4.5, increased magnetic field rotation rate yields increased velocity. Magnetic field amplitudes greater than the threshold produce the greatest velocity, while those less than the threshold produce no velocity. Increased β also yields increased average velocity.

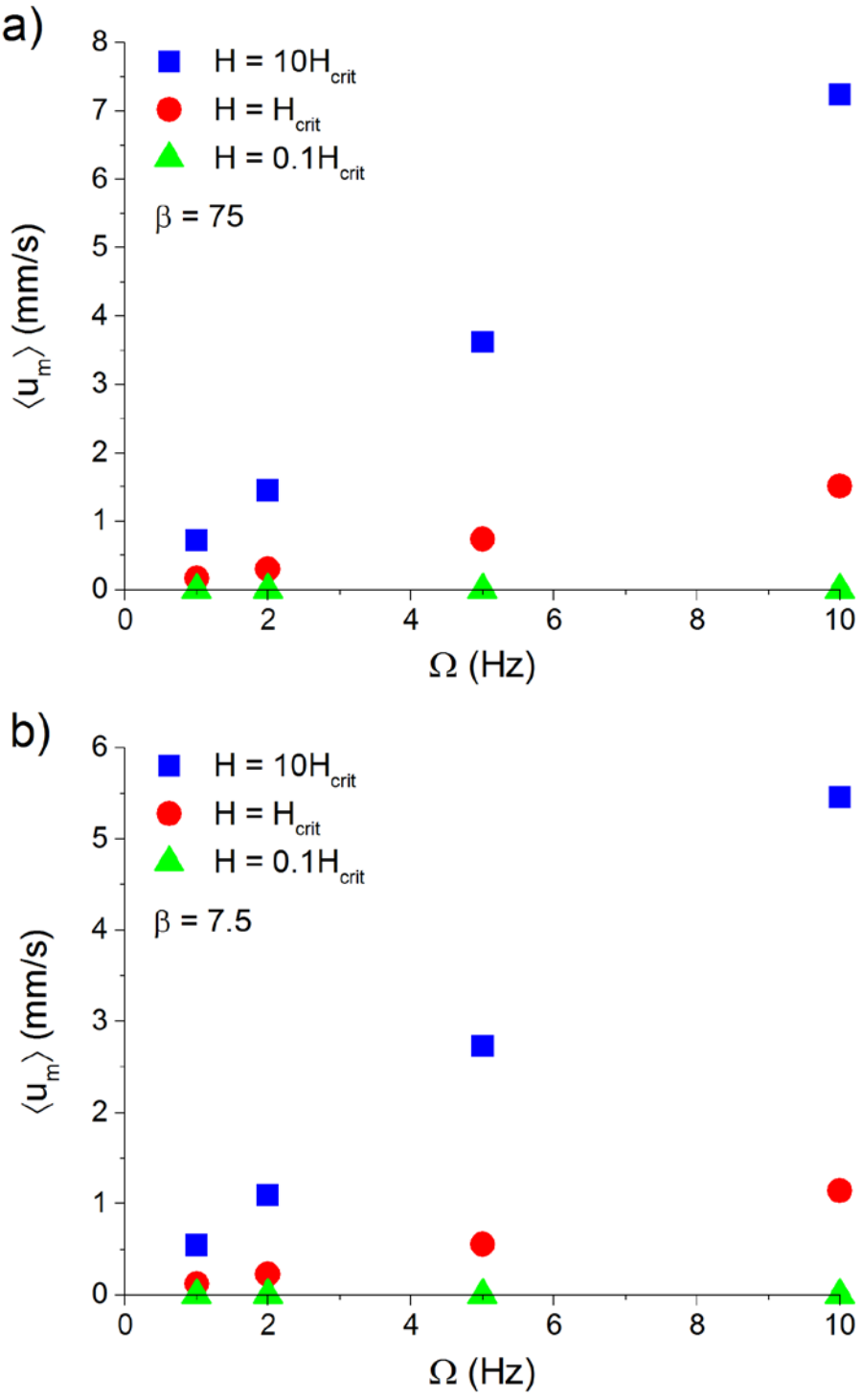

Figure 4.6: Average fluid velocity versus magnetic field rotation rate above, at, and below the critical magnetic field strength with (a) $\beta = 75$ and (b) $\beta = 7.5$.

4.3.3 Overall Velocity Profile

If the channel is blocked, a pressure field will develop in response to drive fluid flow away from the blockage. The magnetically-induced, pressure-induced, and overall dimensionless velocity profiles, U_m, U_p, and U_y, respectively are shown for $\beta = 75$ and $\beta = 7.5$ in Figures 4.7a-b. Superposition of the positive magnetically-induced and negative pressure-induced flow fields yields the net flow field for the system. The fluid flows toward the clot along the far wall and returns from the occlusion by the near wall in keeping with continuity, which dictates that the spatially-averaged net velocity along the channel must be zero at all times. As β decreases, the particles become more evenly distributed across the channel, and the net velocity profile flattens out as the magnetically-induced velocity diminishes and flattens out as well. As U_m becomes increasingly spread across the channel, there ceases to be a place for the return flow that does not essentially negate the total flow altogether.

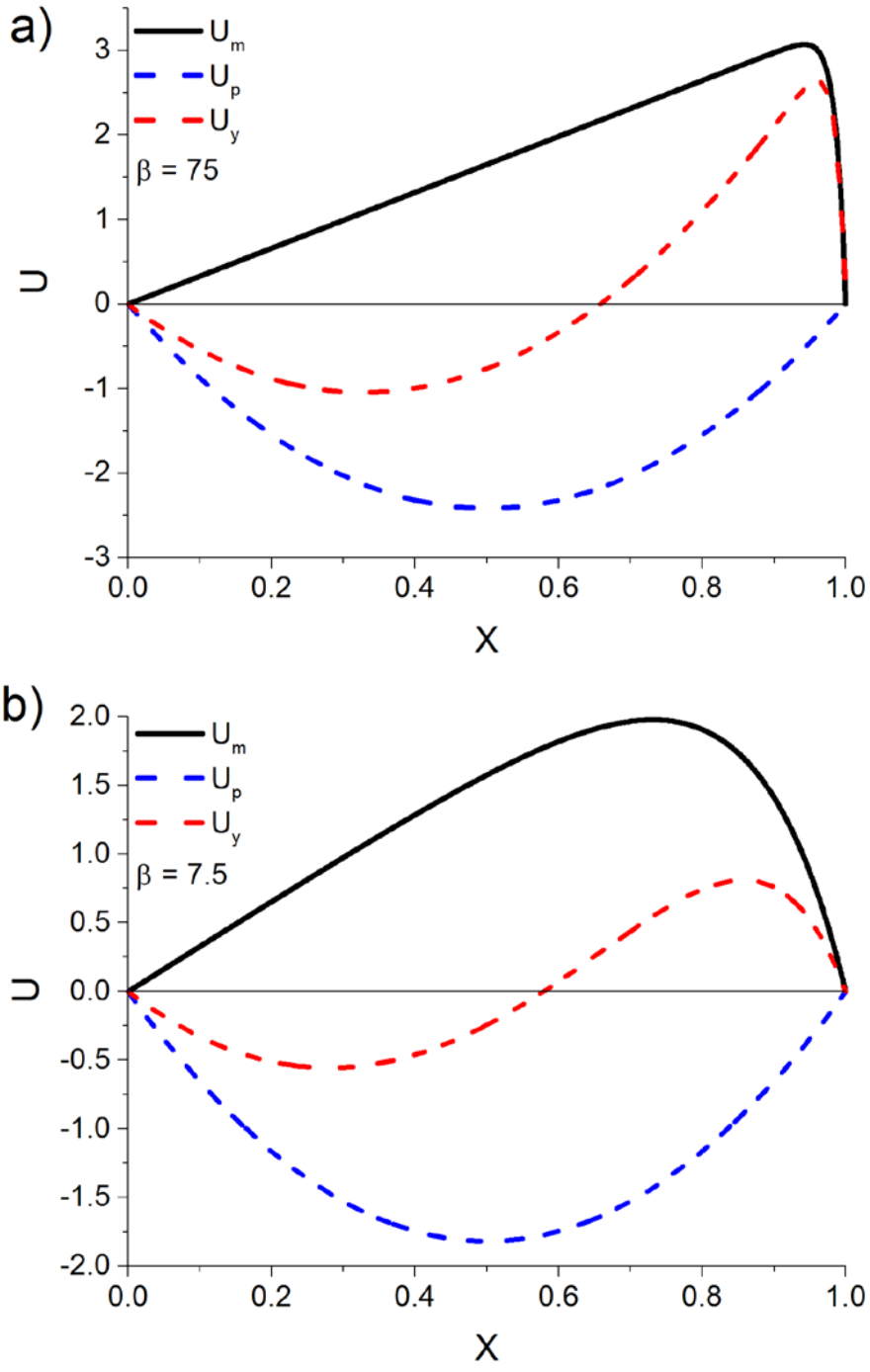

Figure 4.7: Dimensionless velocity profiles of the magnetically-induced flow U_m, the pressure-induced flow U_p, and the overall, combined flow U_y with the applied magnetic field strength ten times greater than the critical threshold and (a) $\beta = 75$ and (b) $\beta = 7.5$.

4.4 DISCUSSION AND CONCLUSIONS

Fluid flow in dead-end pores can be induced by adding ferroparticles to the fluid and applying a rotating magnetic field with a gradient. This fluid flow is induced by the rotation of particle aggregates. Above a critical threshold magnetic field strength, which can be estimated as $H_{crit} = \sqrt{8\eta L^3 Y^C \Omega / (\mu_0 V \alpha_L)}$, the aggregates rotate at the same rate as the magnetic field. Above that critical amplitude, the offset between aggregate orientation and the field orientation is small and inversely proportional to the square of the H-field strength. Below the critical amplitude, negligible torque is generated on the aggregates leading to negligible rotation and subsequently negligible flow. Above the critical amplitude, fluid velocity increases proportionally with field rotation rate. The velocity is independent of the magnetic field strength since further increases in field amplitude cannot force the aggregates to rotate any faster than the applied field. The form of the velocity profile is dictated by the concentration gradient, which is dependent upon the cross-flow Peclet number, beta, that defines the balance between the magnetic body force and hydrodynamic diffusion. A weaker body force owing to a weaker field gradient leads to a flatter velocity profile with less pronounced directional flow within the blocked pore. As such, in order to optimize flow, rapid field rotation, a strong field gradient, and a field strength above the critical threshold are all desired.

Chapter 5: Displaced Magnetic Field

5.1 Changes to Model Equations

In order to improve the model presented in Chapter 4, the assumption that the magnetic field source is located at the channel in the region of interest will now be eliminated. This correction is of practical importance as it means that the H-field source can now be located outside of the stroke victim's head. For a magnetic dipole field source, the dimensional magnetic field is described by

$$\mathbf{h} = \frac{1}{4\pi}\left(\frac{3\mathbf{r}\left(\mathscr{m}\cdot\mathbf{r}\right)}{r^5} - \frac{\mathscr{m}}{r^3}\right), \tag{5.1}$$

where $\mathscr{m}$ is the magnetic dipole moment with $\mathscr{m}_x = \cos\left(\Omega t\right)$ and $\mathscr{m}_y = \sin\left(\Omega t\right)$. $\mathbf{r}$ is the displacement vector between the point of interest and the dipole field source.

This source displacement from the channel is assumed to occur only in the x direction. Defining x_0 as the displacement of the source from the channel, as shown in Figure 5.1, performing a Taylor series expansion, and assuming that $x_0 >> x$ and $x_0 >> y$ gives

$$h_x \cong \frac{\mathscr{m}\cos\left(\Omega t\right)}{2\pi x_0^3}, \tag{5.2}$$

$$h_y \cong \frac{-\mathscr{m}\sin\left(\Omega t\right)}{4\pi x_0^3}. \tag{5.3}$$

Setting the characteristic magnetic field strength, H, equal to $\mathscr{m}/4\pi x_0^3$ yields $H_x = 2H\cos\left(\tau\right)$ and $H_y = -H\sin\left(\tau\right)$.

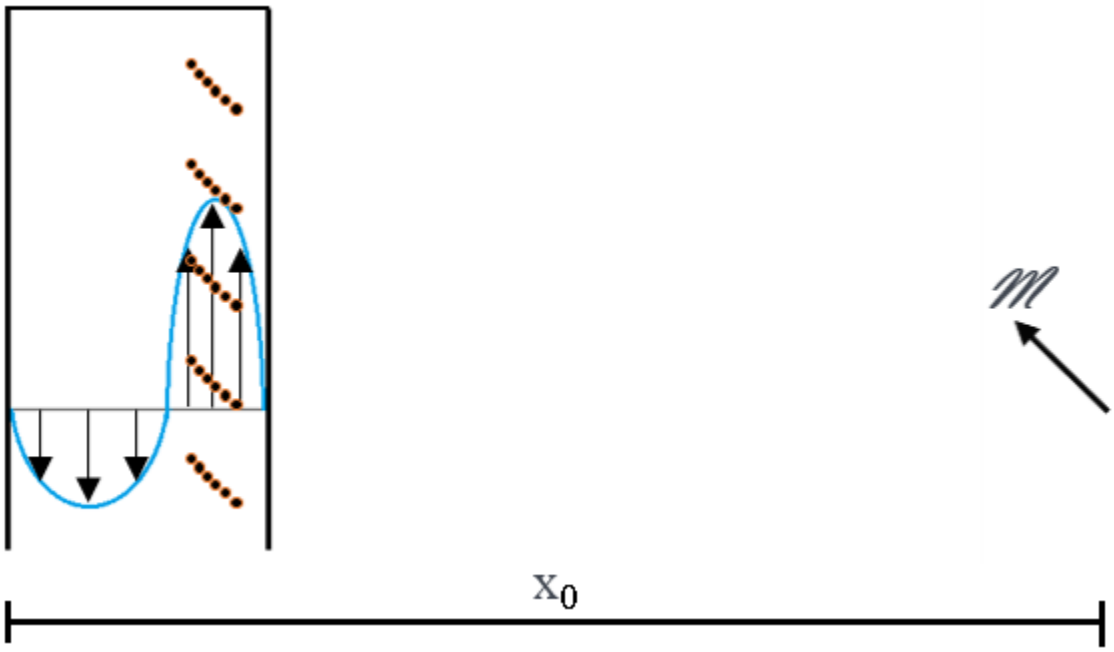

Figure 5.1: Schematic of model system showing particle aggregates, potential flow field, and displaced rotating magnetic field source.

Substituting these new expressions for the x and y components of the dimensionless applied magnetic field into equations (4.3-4.5) yields

$$\frac{\partial P}{\partial Y}=\frac{\partial^2 U_y}{\partial X^2}-\frac{8\pi Y^C}{\sin\theta}\frac{\partial N}{\partial X}\left[\sin(2\tau)\cos(2\phi)-\sin\phi\cos\phi\left(\sin^2(\tau)-4\cos^2(\tau)\right)\right], \quad (5.4)$$

$$\frac{dp_x}{d\tau}=\frac{-\sin\phi}{\sin\theta}\left[\sin(2\tau)\cos(2\phi)-\sin\phi\cos\phi\left(\sin^2(\tau)-4\cos^2(\tau)\right)\right], \quad (5.5)$$

$$\frac{dp_y}{d\tau}=\frac{\cos\phi}{\sin\theta}\left[\sin(2\tau)\cos(2\phi)-\sin\phi\cos\phi\left(\sin^2(\tau)-4\cos^2(\tau)\right)\right]. \quad (5.6)$$

In order to solve for the magnetically-induced velocity profile, equation (5.4) can be analyzed in the same manner as the corresponding equation (4.10) from the previous chapter with the same no slip boundary conditions at the channel walls. The same equation (4.22) is also used to define the concentration profile.

$$N = \beta \frac{\exp(\beta X)}{\exp(\beta) - 1} \tag{4.22}$$

$$U_m = \frac{8\pi Y^C}{\sin\theta} \begin{pmatrix} \sin\phi\cos\phi\left[\sin^2(\tau) - 4\cos^2(\tau)\right] \\ -\sin(2\tau)\cos(2\phi) \end{pmatrix} \left(X - \frac{\exp(\beta X) - 1}{\exp(\beta) - 1} \right) \tag{5.7}$$

Solving for the spatially-averaged magnetically-induced velocity gives

$$\langle U_m \rangle = \frac{8\pi Y^C}{\sin\theta} \begin{pmatrix} \sin\phi\cos\phi\left[\sin^2(\tau) - 4\cos^2(\tau)\right] \\ -\sin(2\tau)\cos(2\phi) \end{pmatrix} \left(\frac{1}{2} - \frac{1}{\beta} + \frac{1}{\exp(\beta) - 1} \right). \tag{5.8}$$

As such, the pressure gradient and pressure-induced velocity profile are given by

$$\frac{\partial P}{\partial Y} = \frac{96\pi Y^C}{\sin\theta} \begin{pmatrix} \sin\phi\cos\phi\left[\sin^2(\tau) - 4\cos^2(\tau)\right] \\ -\sin(2\tau)\cos(2\phi) \end{pmatrix} \left(\frac{1}{2} - \frac{1}{\beta} + \frac{1}{\exp(\beta) - 1} \right), \tag{5.9}$$

$$U_p = \frac{48\pi Y^C}{\sin\theta} \begin{pmatrix} \sin\phi\cos\phi\left[\sin^2(\tau) - 4\cos^2(\tau)\right] \\ -\sin(2\tau)\cos(2\phi) \end{pmatrix} \left(\frac{1}{2} - \frac{1}{\beta} + \frac{1}{\exp(\beta) - 1} \right) \left(X^2 - X \right). \tag{5.10}$$

5.2 PARTICLE DYNAMICS

5.2.1 Torque

Computational simulations of these updated equations were performed in order to evaluate the changes to the particle dynamics and resulting flow field with the magnetic field source displaced. As such, the transient torque is plotted in Figure 5.2a with the applied magnetic field above, at, and below the critical field strength. The time-averaged torque is plotted against the applied magnetic field strength in Figure 5.2b.

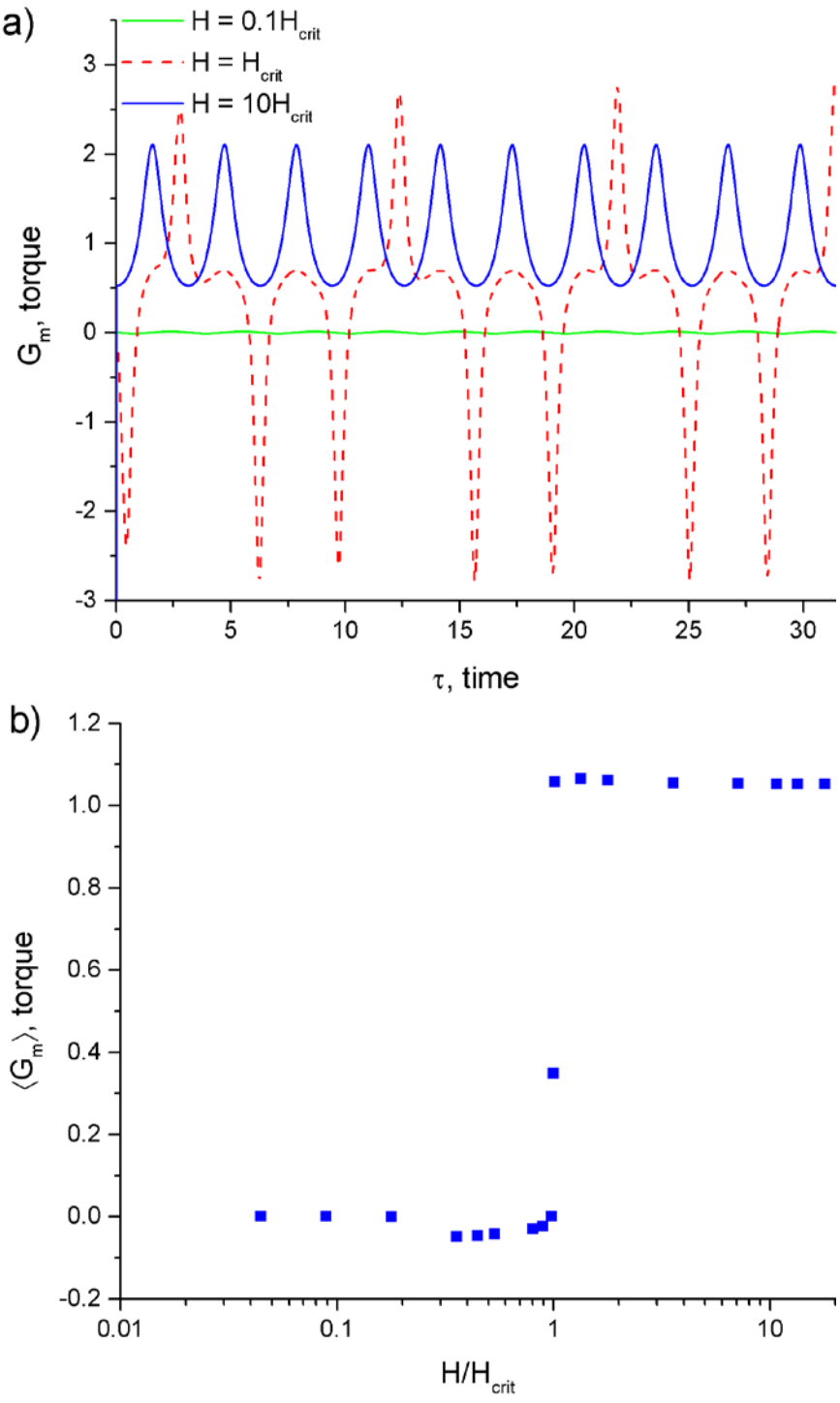

Figure 5.2: Dimensionless torque on particle aggregates in the presence of magnetic fields a) over time above, at, and below the magnetic field's critical threshold, and b) time-averaged at various magnetic field strengths.

The torque generated on the ferro-aggregates with the H-field displaced is approximately zero when the field strength is less than the critical value. When the applied magnetic field strength is greater than the threshold strength, the dimensionless torque transiently oscillates between about 0.5 and 2 with a dimensionless time period of π, or half an aggregate revolution. The average dimensionless torque is around 1.

These oscillations in the torque occur because displacing the magnetic field source causes a change in the magnetic field being applied at the channel. The amplitude of the x-component of the applied field is now twice that of the y-component.

Around the critical field strength, the time-averaged dimensionless torque quickly transitions between 0 and 1. The transient behavior of the torque is erratic, even switching sign, and thus direction.

5.2.2 Orientation Angle

Figure 5.3 tracks the rotation of the aggregates in response to the torque, plotting their orientation angle over time, for three different cases: above, at, and below the critical magnetic field amplitude. As with the non-displaced magnetic field source analyzed in Chapter 4, when the applied field is weaker than the critical field, aggregate rotation is insignificant. When the applied magnetic field strength is greater than the critical H-field strength, however, the aggregates no longer rotate in sync with the field source. Orientation angle does not change linearly from π to $-\pi$, but instead deviates from linearity in an oscillatory manner in response to the changing torque. Around the threshold magnitude, the aggregates still rotate primarily in one direction, but their rotation is chaotic and bears little to no resemblance to the field rotation.

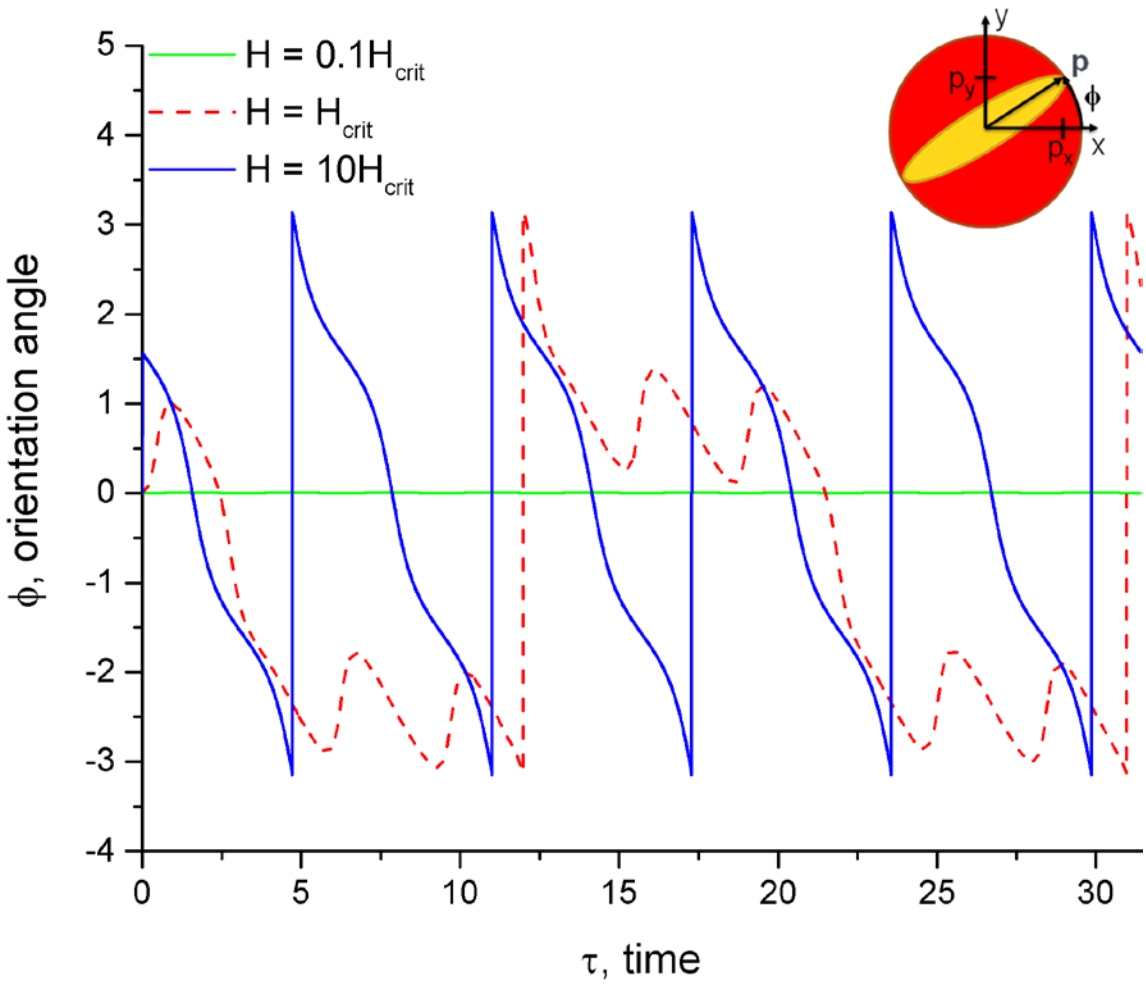

Figure 5.3: Orientation angle of the aggregates over dimensionless time for 5Hz magnetic fields above, at, and below the critical field strength.

5.2.3 Offset Angles

Alternatively, this information can be demonstrated by plotting the difference between aggregate orientation and the H-field source orientation over time as shown in Figure 5.4. For magnetic fields much stronger than the critical threshold strength, following an initial transience, this pseudo-offset angle oscillates around $-\pi/2$. The oscillations are in response to the changing torque. Due to the displacement of the magnetic field source from the channel, the applied magnetic field is no longer oriented

in the same direction as the magnetic field source. As such, aggregate orientation initially rapidly transitions from agreement with the H-field source at zero degrees to near alignment with the applied field source. This leaves the magnetic field source approximately 90 degrees, or $\pi/2$ radians, behind the orientation of the aggregates.

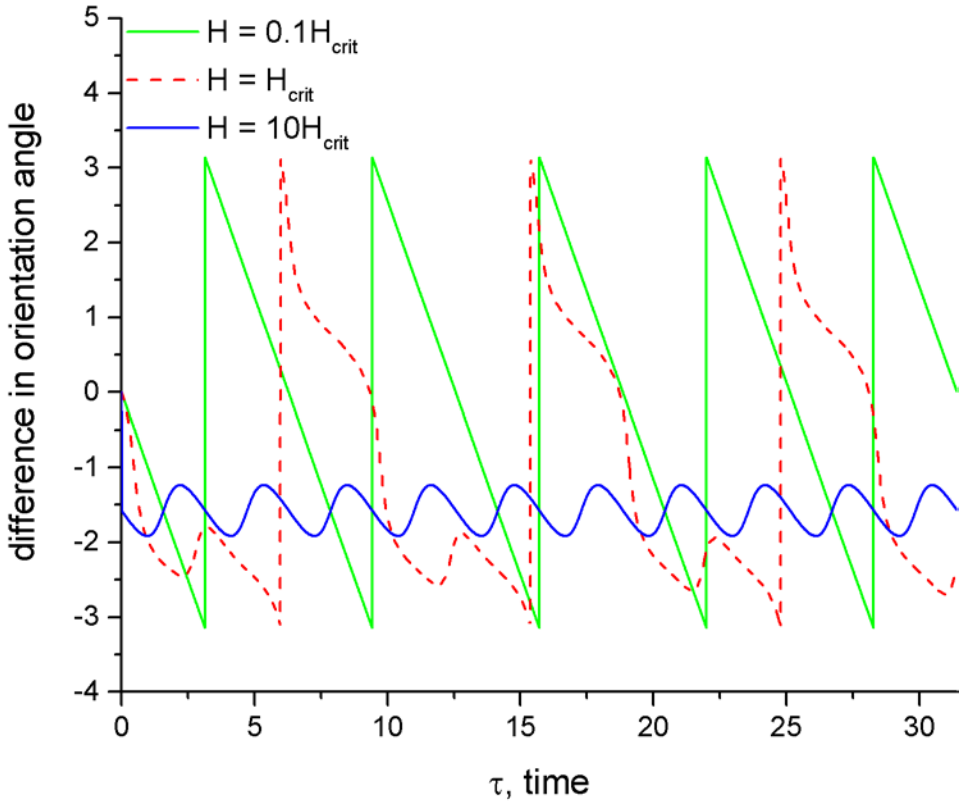

Figure 5.4: The difference between aggregate orientation and the magnetic field source orientation over time above, at, and below the magnetic field's critical threshold.

The magnitude of the time-averaged offset angle between the orientation of the aggregates and the applied H-field orientation is plotted against the magnetic field strength in Figure 5.5 in order to obtain further insight into the particle dynamics. As with the non-displaced magnetic field source, the largest transiently averaged offset

angles are obtained for applied H-field strengths near the critical threshold because aggregate orientation and offset behave chaotically over time. Small average offset angles are obtained for weak magnetic fields well below the threshold magnitude because the aggregates have essentially stopped moving. Both offset angle and applied magnetic field orientation are bound between $-\pi$ and π, and the average applied H-field orientation is zero. As such, the times when aggregate offset is negative cancel out those when offset is positive. For magnetic field strengths well above the critical magnitude, the offset angle, θ, approaches zero for all times following the initial transience.

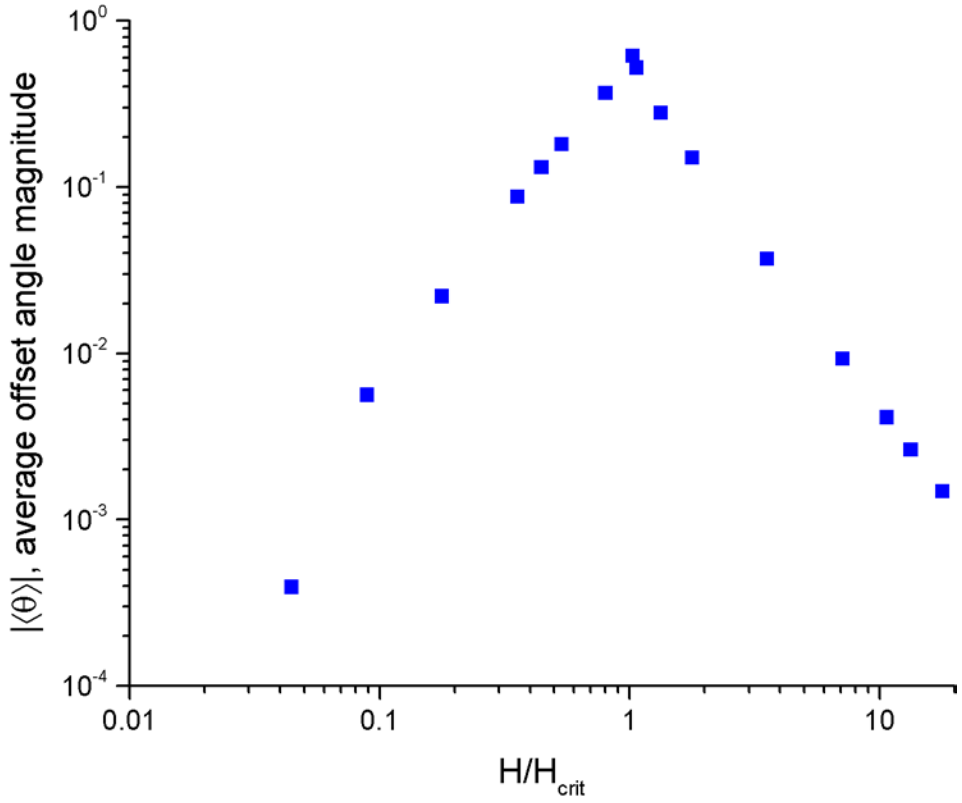

Figure 5.5: The magnitude of the time-averaged offset angle between aggregate orientation and the applied magnetic field orientation at various magnetic field strengths.

5.3 FLUID FLOW

5.3.1 Magnetically-Induced Velocity Profile

The aggregate dynamics induce fluid flow within the channel, so the critical field strength which plays such an important role in those dynamics is also an essential parameter of the fluid velocity profile. Figure 5.6a plots the dimensionless magnetically-induced velocity profile across the channel at the critical magnetic field strength for a particular cross-flow Peclet number, β, of 75, while Figure 5.6b does the same above the magnetic field strength.

Since the torque changes transiently due to the magnetic field source displacement, the magnetically-induced velocity also changes with time. The spatially-averaged velocity is actually proportional to the torque on the aggregates. A negative velocity profile is obtained at $\tau = 2\pi$ with the magnetic field near its critical strength because the corresponding torque is negative. Similarly, well above the threshold field strength, the torque and magnetically-induced velocity both oscillate transiently with a dimensionless time period of π. As such, both are minimized when the dimensionless time is a multiple of π and both peak at times halfway between the nearest minima.

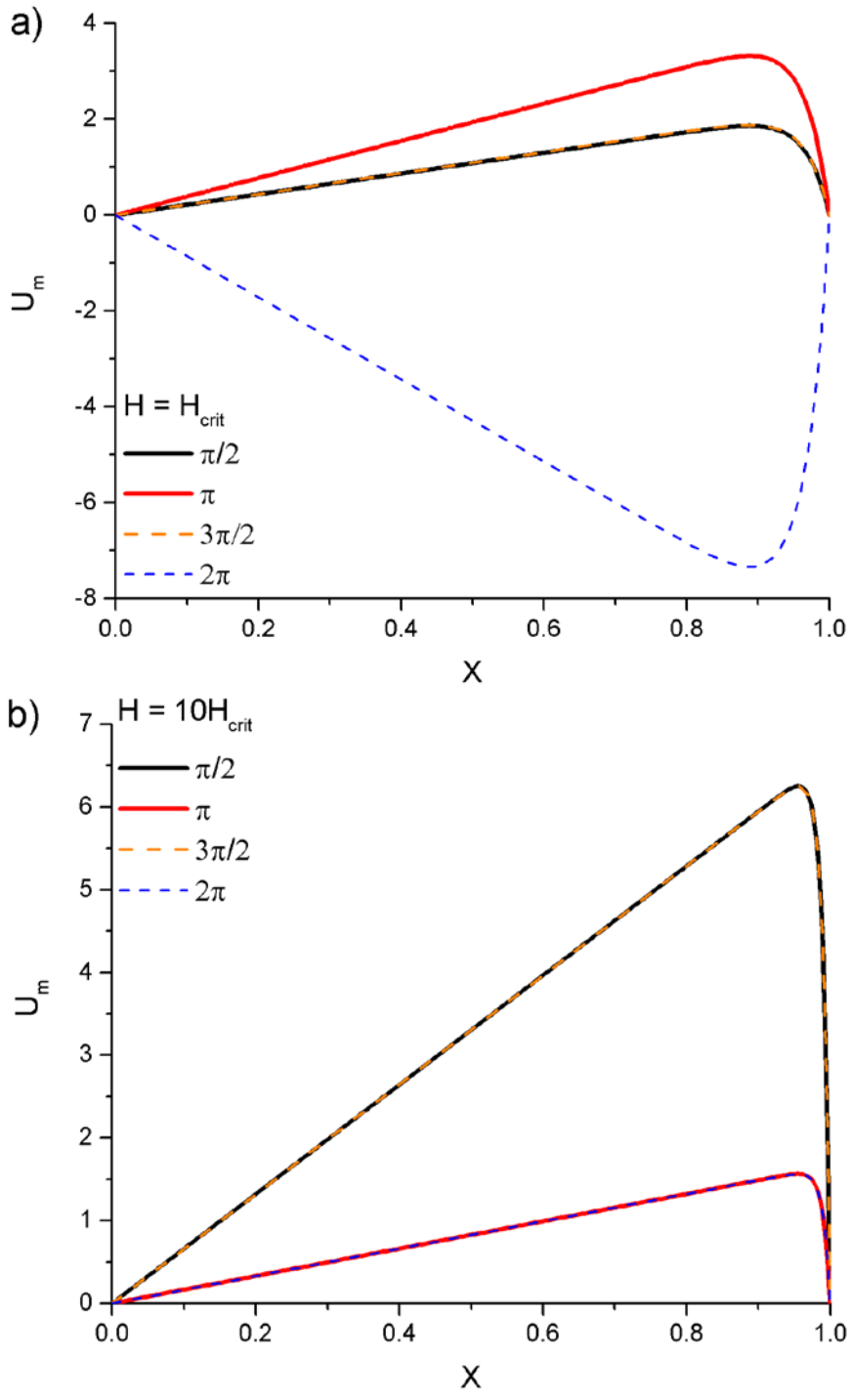

Figure 5.6: Dimensionless velocity profiles across a blocked channel with β = 75 a) at the magnetic field's critical threshold and b) above the critical magnetic field strength.

5.3.2 Pressure-Induced and Overall Velocity Profiles

As noted in Chapter 4, in a blocked channel, a pressure field will develop in response to drive fluid flow away from the blockage. The magnetically-induced, pressure-induced, and overall dimensionless velocity profiles, U_m, U_p, and U_y, respectively are shown for $\beta = 75$ in Figures 5.7a-c.

The transient magnetically-induced velocity produces a correspondingly transient pressure gradient and, therefore, transient pressure-induced velocity. Larger magnetically-induced velocities yield larger pressure-induced velocities, so the magnitude of U_p reaches its maxima and minima at the same times as U_m. Superposition of the positive magnetically-induced and negative pressure-induced flow fields yields the net flow field for the system. The fluid flows toward the clot along one wall and returns from the occlusion by the other wall in keeping with continuity, which dictates that the spatially-averaged net velocity must be zero at all times.

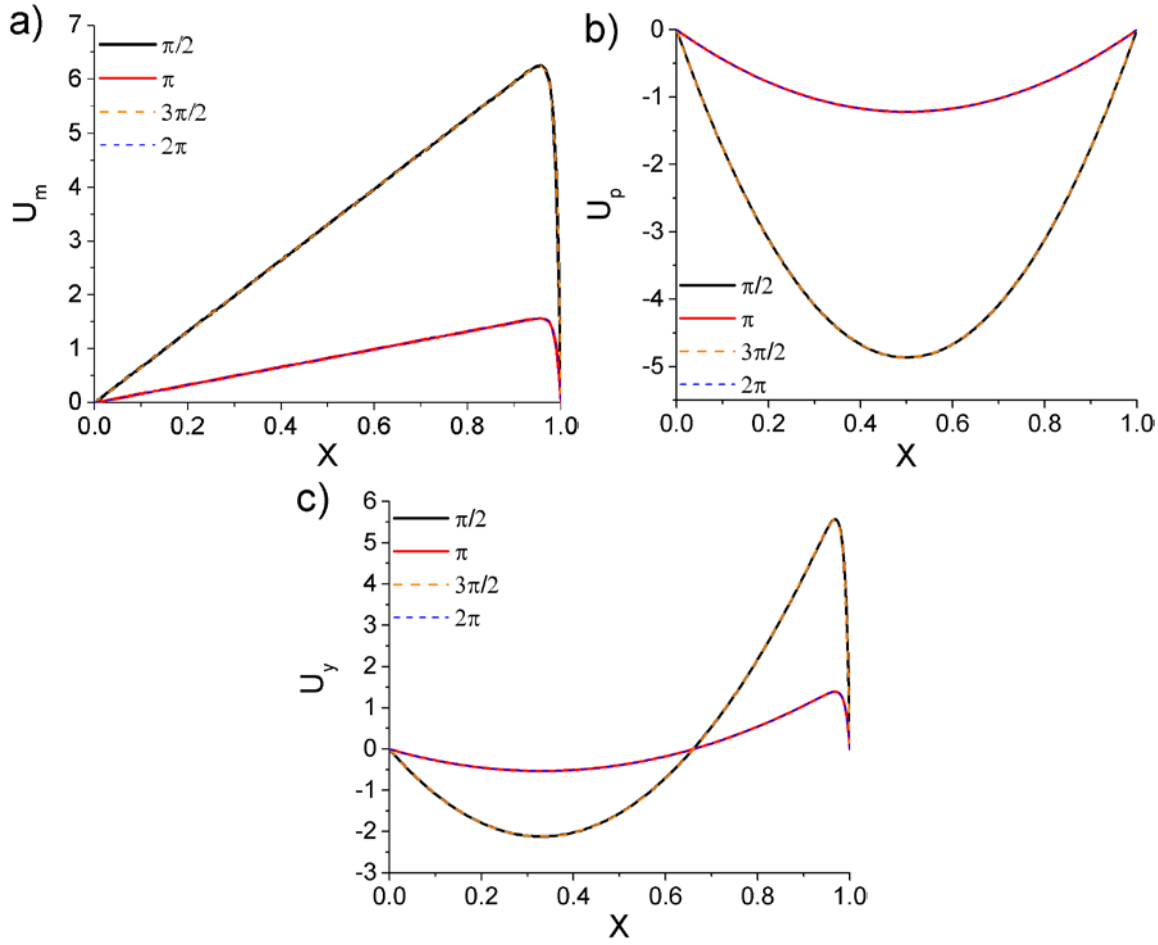

Figure 5.7: Dimensionless velocity profiles across a blocked channel with β = 75 showing how the superposition of a) the magnetically-induced velocity profile and b) the pressure-induced velocity profile creates c) the overall velocity profile for magnetic fields much stronger than the critical threshold.

5.3.3 Shear and Volume Fraction Profiles

Based upon the overall velocity profile, the shear rate profile within the blocked channel can be obtained from the derivative of the velocity with respect to *x*. As shown in Figure 5.8, when a typical 7500A/m magnetic field, well above the critical H-field strength, rotating at 5Hz, or 10π radians per second, is applied to an occluded channel with an average ferroparticle volume fraction of 0.1%, the magnitude of the shear rate is

less than that of the rotation rate throughout most of the channel. Near the channel wall closer to the field source, however, the shear surpasses the rotation rate. Despite the small portion of the channel where this happens, this is still notable since the ferroparticles are heavily concentrated in that region. While unimportant for aggregates of fixed size, rotation and shear are competing mechanisms by which the ferro-aggregates may be broken down. Figure 5.8 suggests that both mechanisms are important. Shear dominates in the thin layer near the wall, where the ferro-aggregates are most concentrated, while rotation dominates everywhere else.

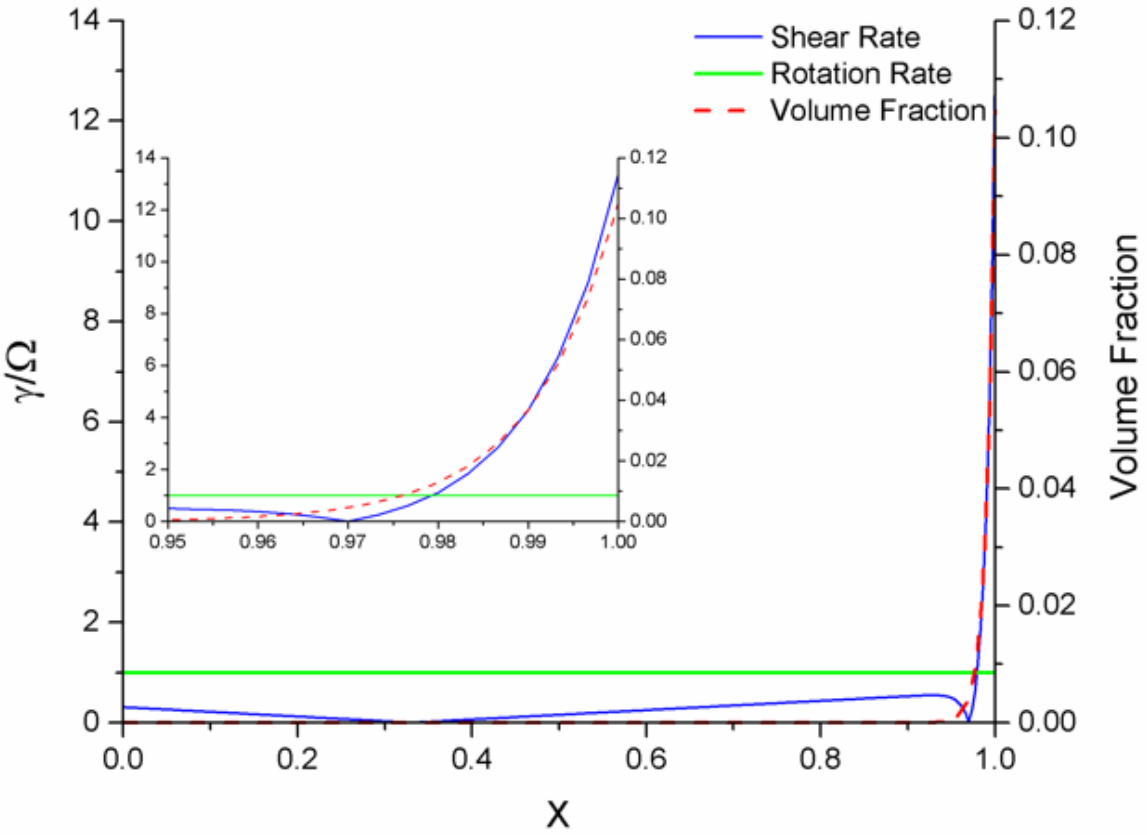

Figure 5.8: Dimensionless induced shear and ferroparticle volume fraction profiles across a channel with an average volume fraction of 0.1%, under the influence of a 7500A/m magnetic field rotating at 5Hz, when $\tau = \pi/2$.

Chapter 6: Aggregates of Variable Size

6.1 Equations Relating Shear, Length, and Aspect Ratio

In order to further improve the model presented in Chapter 5, the assumption that the aggregates are of fixed size will now be eliminated. As in practice, the size of the aggregates will be dictated by either their rotation or the shear acting on them, whichever keeps the aggregates smaller. Following Bossis (2002) and Gomez-Ramirez (2011), the aggregate length, $2L$, is implicitly defined.

$$\gamma = 0.046383 \frac{\mu_0 \mu_f}{\eta L} r_p H^2 \left[\frac{\mu_p - \mu_f}{\mu_p + 2\mu_f} \right]^2, \tag{6.1}$$

where r_p is the radius of the individual ferroparticles, μ_f is the relative magnetic permeability of the fluid, and μ_p is the relative magnetic permeability of the ferro-aggregates. The relative magnetic permeability of the fluid is assumed to be approximately equal to 1, while the relative magnetic permeability of the aggregates is functionally related to their magnetic susceptibility, χ_M.

$$\mu_p = \chi_M + 1 \tag{6.2}$$

The magnetic susceptibility relates the applied magnetic field strength to the magnetization of the aggregates in a manner similar to equation (3.6).

$$m = \chi_M h, \tag{6.3}$$

$$\mathbf{m} = \alpha_L \mathbf{pp} \cdot \mathbf{h} + \alpha_T \mathbf{h}, \tag{3.6}$$

where α_L is related to the aspect ratio, $\alpha_L = (2/3)(L/a)^2 \left[\ln(2L/a) - 1 \right]^{-1}$, and $\alpha_T = 2$ [Rocha and Acrivos (1974)].

It follows that

$$\chi_M \cong \frac{(2/3)(L/a)^2}{\ln(2L/a)-1}+2, \tag{6.4}$$

$$\mu_p \cong \frac{(2/3)(L/a)^2}{\ln(2L/a)-1}+3, \tag{6.5}$$

$$\gamma \cong 0.046383\frac{\mu_0\mu_f}{\eta L}r_p H^2\left[\frac{\frac{(2/3)(L/a)^2}{\ln(2L/a)-1}+2}{\frac{(2/3)(L/a)^2}{\ln(2L/a)-1}+5}\right]^2 \tag{6.6}$$

In order to fully describe the size of the aggregates, however, the relationship between aggregate diameter, 2*a*, and aggregate length, 2*L*, must also be defined. From the analysis of Gomez-Ramirez (2011), L/r_p is "roughly proportional" to $\left(a/r_p\right)^2$. Since L/r_p is equivalent to the number of particles along the major axis of the ellipsoid and a/r_p is equal to the number of particles along the minor axis of the ellipsoid, this makes physical sense. In response to increased magnetic field strength, aggregate diameter will increase slower than aggregate length due to the tendency of the ferroparticles to align themselves with the applied magnetic field. Aggregate diameter is not constant with increasing *H* though. As magnetic field strength increases, the magnetic attractive forces increase and ferroparticles can more easily join aggregates without attaching to one end or the other. As such, $a/r_p = \left(L/r_p\right)^k$ where *k* is between 0 and 1. Setting *k* to 0.5 gives $L = a^2/r_p$.

6.2 Further Adjustments to Model Equations

Aggregate length variability also affects other parameters of the magnetically-induced velocity. Significantly, the characteristic velocity depends upon *L*. As such, using the non-dimensionalizations from Chapter 3 is no longer practical, and equations will now be presented dimensionally.

Additionally, the magnitude of the hydrodynamic diffusion of the aggregates, $|\mathbf{d}|$, is defined by the product of the shear and L^2 [Davis (1996)].

$$|\mathbf{d}| = \gamma L^2 \tag{6.7}$$

Aggregate velocity across the channel due to the magnetic field gradient, u_g, is proportional to the magnetization of the aggregates and, therefore, is roughly proportional to the product of the H-field strength and the aspect ratio dependent parameter α_L.

$$u_g \propto H\alpha_L \tag{6.8}$$

Since the balance between $\mathbf{u_g}$ and $\mathbf{d}$ controls the shape of the concentration profile within the channel, the equations relating to the concentration must be updated as well. Equation (3.4), defining the aggregate number density, must be modified to define the ferroparticle number density since aggregates are no longer conserved.

$$\frac{\partial n}{\partial t} + \mathbf{u_g} \cdot \nabla n = \nabla \cdot (\mathbf{d} \cdot \nabla n) \tag{3.4}$$

The number of particles per aggregate, n_a, can be defined by the ratio of particle number density, c, to aggregate number density.

$$n_a = \frac{c}{n} \tag{6.9}$$

Alternatively, n_a can be defined with respect to the physical dimensions of the ferroparticles and their aggregates as

$$n_a = \frac{\pi}{6}\frac{a^2 L}{r_p^3}. \tag{6.10}$$

Since n, c, $\mathbf{u_g}$, and $\mathbf{d}$ are all dependent upon L and, therefore, x but independent of y-position along the channel, equation (3.4) then becomes

$$\frac{\partial c}{\partial t} = -\frac{\partial u_g c}{\partial x} + \frac{\partial}{\partial x}\left[|\mathbf{d}|\frac{\partial c}{\partial x}\right] - \frac{\partial}{\partial x}\left[|\mathbf{d}|\frac{c}{n_a}\frac{\partial n_a}{\partial x}\right]. \tag{6.11}$$

Additionally, since *a*, *L*, *n*, and α_L are all functions of *x*, the equations for the velocity profiles must be adjusted. The magnetically-induced velocity profile becomes

$$u_m = \frac{4}{3}\pi\frac{\mu_0}{\eta}H^2\left(\int_0^x a^2 Ln\alpha_L \mathrm{d}\psi - \frac{x}{d}\int_0^d a^2 Ln\alpha_L \mathrm{d}x\right) f\left(t,\Omega,\phi\right), \tag{6.12}$$

where $f\left(t,\Omega,\phi\right) = \sin\left(2\Omega t\right)\cos\left(2\phi\right) - \sin\phi\cos\phi\left[\sin^2\left(\Omega t\right) - 4\cos^2\left(\Omega t\right)\right]$ and ψ is being used as a variable of integration in place of *x*.

6.3 Model System Parameters and Initial Conditions

These equations are of a circular nature. For example, shear defines aggregate length, which sets the concentration profiles of the aggregates and ferroparticles, which affect the velocity profiles that define the shear. As such, computational solution of these expressions is very useful. Computational loops can be used to solve the system of equations transiently, solving for new values at the current time based upon previous values at past times. For example, the original expression for the shear defines an expression for aggregate length, which ultimately defines a new shear at a new time.

In order for this approach to work, initial conditions must be provided. These initial conditions are listed in Table 6.1. The dimensional values of the system parameters for a base case follow in Table 6.2. The system parameters do not change with time.

System Parameter	Meaning	Initial Value with Units	Initial Value in Alternate Units
a	aggregate semi-minor axis length	5×10^{-7} m	500nm
ϕ	aggregate orientation	$\pi/2$ radians	90°
β	cross-flow Peclet number	75	
u_m	magnetically-induced velocity	0 m/s	0 mm/s
u_p	pressure-induced velocity	0 m/s	0 mm/s

Table 6.1: Necessary initial conditions for solving the model system of equations.

System Parameter	Meaning	Value with Units	Value in Alternate Units
r_p	ferroparticle radius	5×10^{-8} m	50 nm
d	channel diameter	.003 m	3 mm
H	H-field strength	7500 A/m	
Ω	H-field rotation rate	10π rad/s	5 Hz
η	fluid viscosity	4×10^{-3} Pa·s	
μ_0	magnetic permeability of a vacuum	$4\pi\times10^{-7}$ N/A^2	
μ_f	relative magnetic permeability of fluid	1	
Φ	average volume fraction of particles	10^{-3}	0.1%

Table 6.2: Fixed values of various system parameters used for solving the base case.

6.4 AGGREGATE ORIENTATION

Computational simulations of the updated equations were performed using the preceding system parameters and initial conditions. Changes to the particle dynamics and the resulting flow field were evaluated with aggregate size controlled by rotation and shear.

Figure 6.1 tracks the rotation of the aggregates, plotting their orientation angle over time. Aggregate orientation does not change noticeably depending upon whether aggregate size is fixed or not.

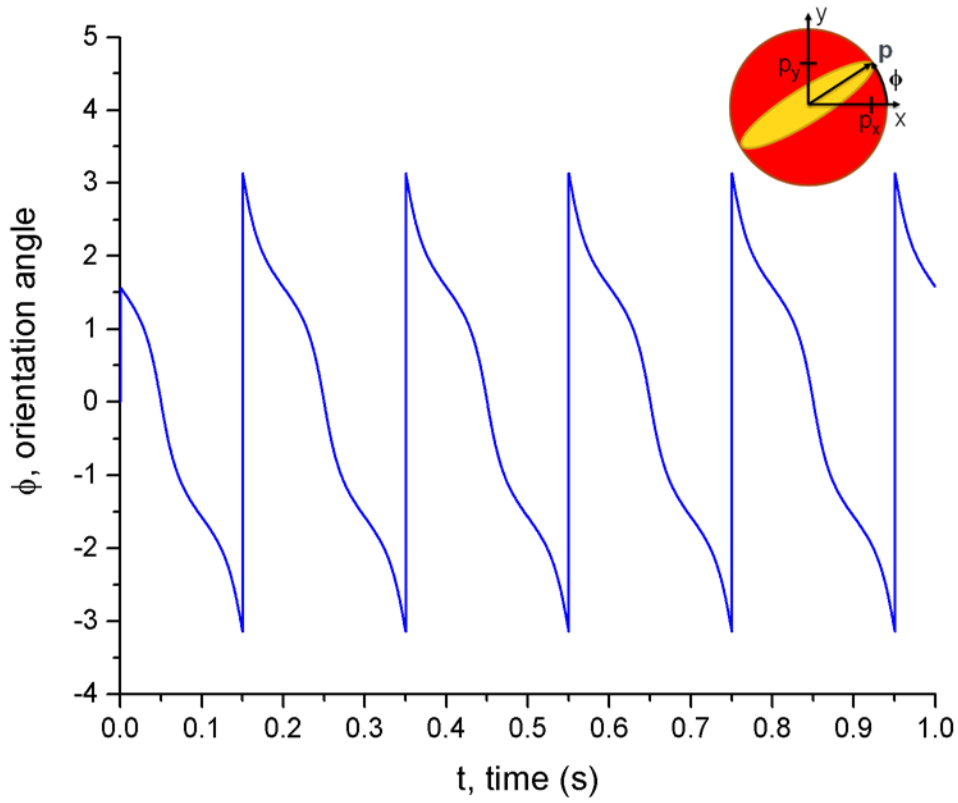

Figure 6.1: Orientation angle of the aggregates over time for a 7500A/m magnetic field, above the critical field strength, rotating at 5Hz.

6.5 VELOCITY PROFILES

As shown in Figures 6.2a-c, the magnetically-induced, pressure-induced, and overall velocity profiles obtained using the variable aggregate size model appear qualitatively similar to those obtained with aggregate size fixed. The velocity profiles still oscillate transiently with a dimensionless time period of $\Omega t = \pi$. Interestingly, although the system was computationally solved transiently assuming an initially quiescent channel, by the time Ωt equals $\pi/2$, the system has reached its pseudo-steady state in which the flow field repeats every dimensionless time period.

For the base case in which a 7500A/m magnetic field rotating at 5Hz is applied to a channel with an average ferroparticle volume fraction of 0.1%, the overall flow velocity

toward the blockage achieves a maximum value of roughly 3.53mm/s when Ωt equals $\pi/2$ and where x equals 2.9mm. The return flow velocity away from the blockage obtains its maximum magnitude of about 1.35mm/s at the same time where x equals 1mm.

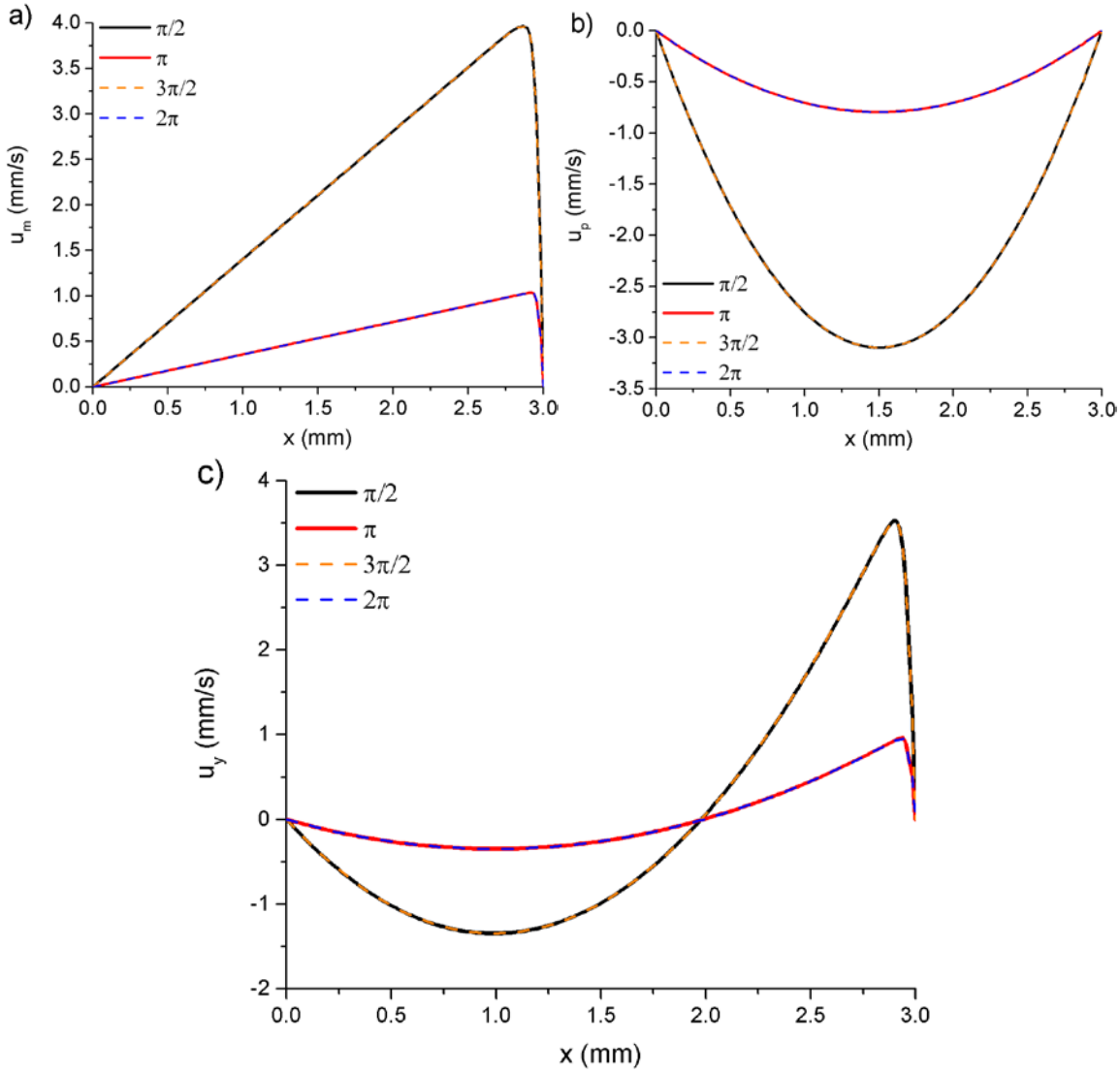

Figure 6.2: Velocity profiles across a blocked channel with an average ferroparticle volume fraction of 0.1% in the presence of a 7500A/m magnetic field rotating at 5Hz showing how the superposition of a) the magnetically-induced velocity profile and b) the pressure-induced velocity profile creates c) the overall velocity profile.

6.6 Shear, Aggregate Size, and Volume Fraction Profiles

Since the velocity profiles qualitatively match with those obtained in Chapter 5, it follows that the shear profiles are also of similar shape. As shown in Figure 6.3a, the base case of a 7500A/m magnetic field rotating at 5Hz applied to an occluded channel with an average ferroparticle volume fraction of 0.1% still yields shear rates that are less significant than the rotation rate throughout most of the channel. Near the channel wall closer to the field source, the shear still surpasses the rotation rate. The ferro-aggregates in that region are sheared to lengths that are shorter than the rotationally set maximum as shown in Figure 6.3b.

Figure 6.4 highlights some differences between the fixed and variable aggregate size models. The ratio of the maximum induced shear to the rotation rate is significantly decreased by using the variable size model. Correspondingly, the width of the region where shear dominates is smaller, however, this does not mean that the shearing of the aggregates is unimportant. The ferroparticle volume fraction profile is even sharper, increasing rapidly to its maximum at the channel wall nearer to the magnetic field source.

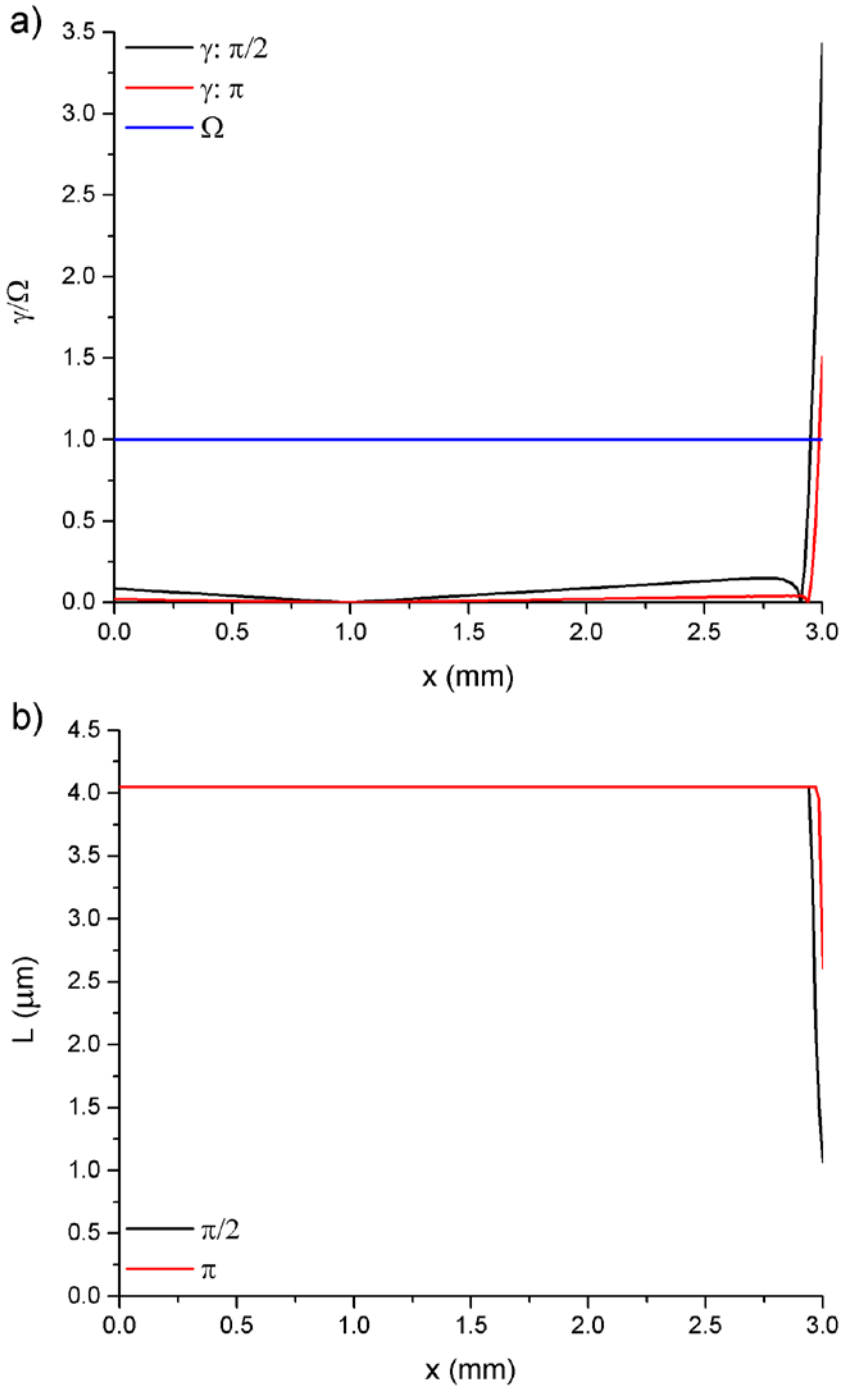

Figure 6.3: Profiles of a) shear and b) length of the semi-major axis of the aggregates across a channel, with an average ferroparticle volume fraction of 0.1%, in the presence of a 7500A/m magnetic field rotating at 5Hz when Ωt equals π/2 and π.

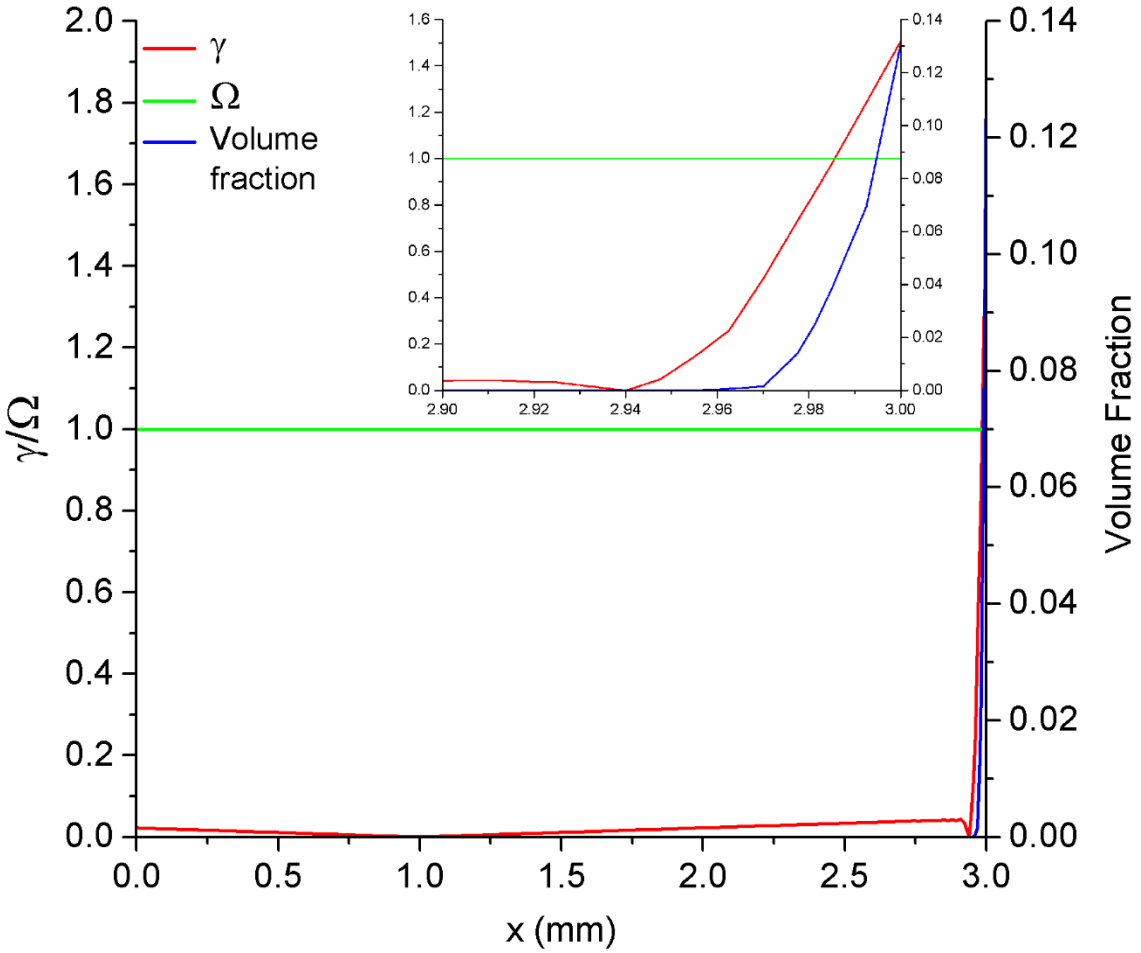

Figure 6.4: Profiles of induced shear and particle volume fraction across a blocked channel, with an average volume fraction of 0.1%, under the influence of a 7500A/m magnetic field rotating at 5Hz when Ωt equals π.

6.7 Average Magnetically-Induced Velocity

Due to the high shear near the channel wall closer to the magnetic field source, the length of the aggregates is not constant in time or space under the base conditions. When the aggregates were of fixed length, the average magnetically-induced velocity changed proportionally with the rotation rate of the applied magnetic field as suggested by the characteristic velocity chosen for the non-dimensionalization in Chapter 3, $u_c = L^3 \Omega d \, \Phi / V$.

Unfortunately, that characteristic velocity also depended upon aggregate size. If the rotation rate is permitted to control aggregate size with the magnetic field strength held constant, increased rotation rate will lead to smaller aggregates until they are broken down into individual ferroparticles unable to effectively induce fluid flow. This is shown in Figure 6.5 as the rotation of the magnetic field becomes faster than 10Hz.

Decreasing rotation rate will also eventually lead to no flow. As originally indicated by the characteristic velocity, no matter how large the aggregates are, if they do not rotate, no fluid flow will be induced. As such, the average magnetically-induced velocity must reach a maximum at some intermediate field rotation rate.

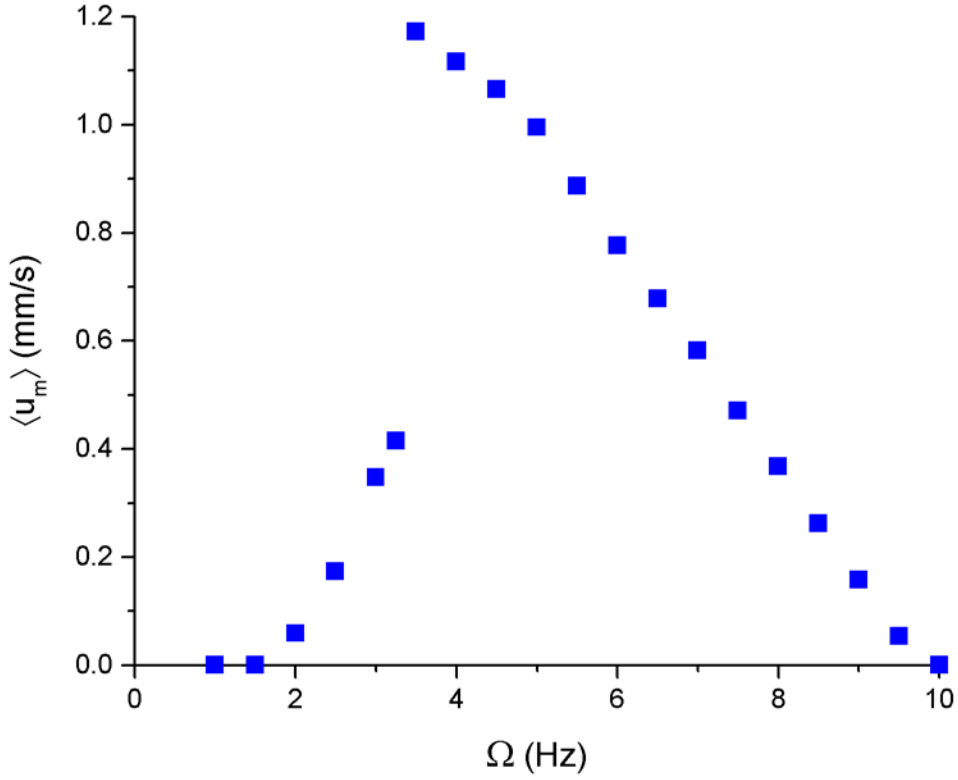

Figure 6.5: Average magnetically-induced velocity in a channel with an average particle volume fraction of 0.1% under the influence of a 7500A/m magnetic field rotating at various frequencies.

There are other issues with low rotation rate, however, that relate to aggregate size. The sharp change in the average magnetically-induced velocity between 3.25Hz and 3.5Hz depicted in Figure 6.5 is caused by the introduction of the shear as a parameter of interest. As shown in Figure 6.6, for a 7500A/m magnetic field, when the rotation rate is 3.25Hz or less, the rotation sets aggregate length everywhere in the channel. When the rotation rate is 3.5Hz or more, shear controls aggregate length near the channel wall closer to the magnetic field source.

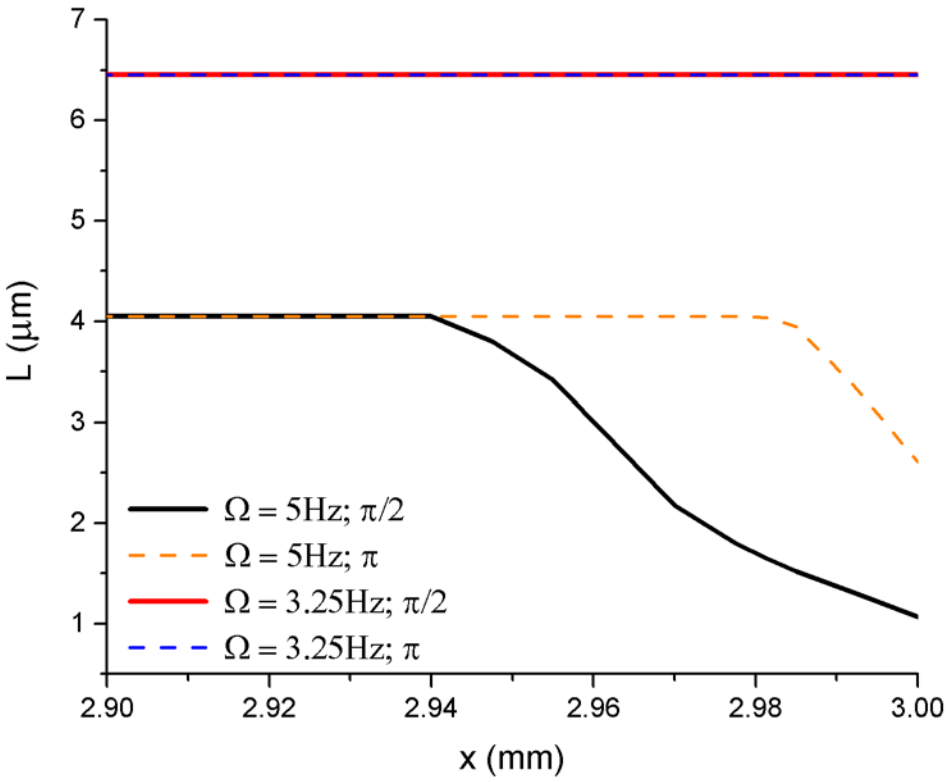

Figure 6.6: Length of the semi-major axis of the aggregates near the wall where shear is highest under the influence of a 7500A/m magnetic field rotating at 5Hz and 3.25 Hz when Ωt equals π/2 and π.

Assuming a fixed quantity of ferroparticles, or a fixed average volume fraction, as the aggregates grow larger the number of aggregates drops. When the H-field rotation

rate is decreased, without sufficient shear to keep aggregate size under control, the number of aggregates eventually becomes too few to effectively induce flow. This is reflected in Figure 6.5 as the rotation of the magnetic field becomes slower than 1.5Hz.

This effect can also occur as the magnetic field strength is increased beyond 10,000A/m while the rotation rate is held constant at 5Hz as shown in Figure 6.7.

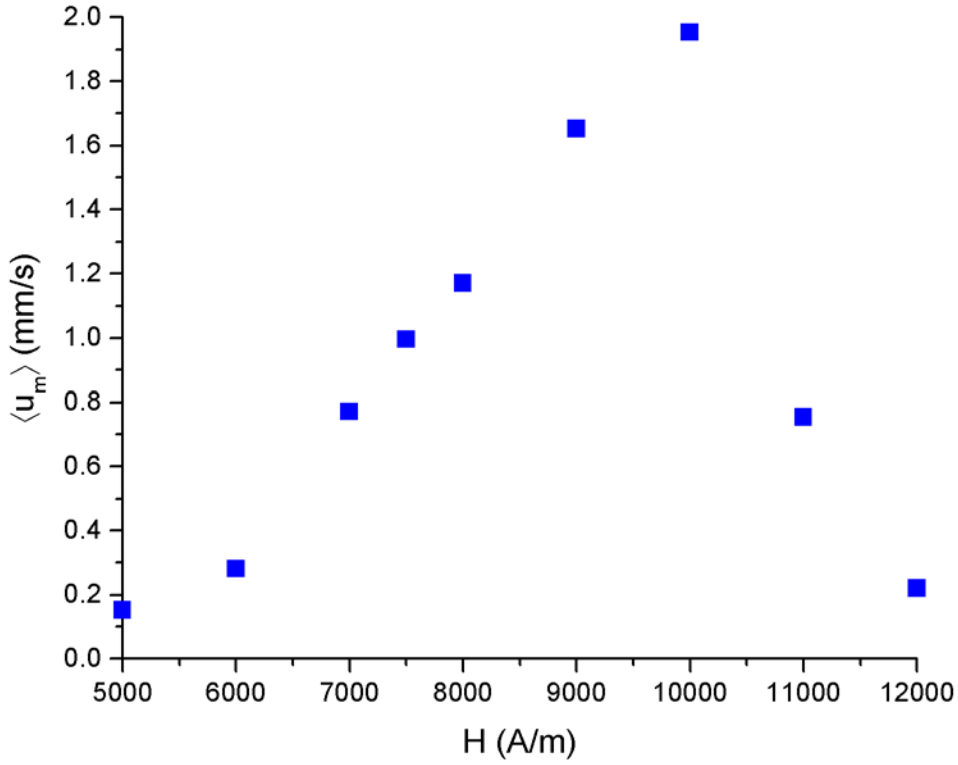

Figure 6.7: Average magnetically-induced velocity in a channel with an average particle volume fraction of 0.1% under the influence of a 5Hz magnetic field at various field strengths.

Based upon Figures 6.5 and 6.7, it is evident that careful selection of the frequency and magnitude of the applied magnetic field is essential to optimizing the magnetically-induced flow in occluded vessels.

Chapter 7: Transport in a Magnetically-Induced Flow Field

7.1 INTRODUCTION

In order to more fully understand the time required for thrombolytic to be delivered to a thrombus when the transport has been magnetically-enhanced, computational simulations were developed to investigate the convective and diffusive transport in an artery.

A number of assumptions were made. The reactions of the thrombolytic both within the bloodstream and at the thrombus were ignored. The transient oscillations of the induced flow field were also ignored. Additionally, the initial evolution of the ferroparticle concentration profile within the occluded vessel is also ignored. The ferroparticle concentration gradient is assumed to be fixed with respect to both time and y-position along the blocked channel length.

The model geometry was a two-dimensional representation of the last 4.5cm of a 3mm wide channel leading up to a blockage, like a thrombus. It did not include the neighboring unblocked vessel or the entrance to the occluded vessel. As such, transport through the unblocked vessel and entrance effects at the inlet to the occluded vessel were not analyzed.

7.2 FLOW FIELD

The steady state flow field was computationally obtained by using COMSOL Multiphysics to simultaneously solve the continuity (2.1) and incompressible Navier-Stokes (2.2) equations.

$$\nabla \cdot \mathbf{u} = 0 \tag{2.1}$$

$$\rho \frac{\partial \mathbf{u}}{\partial t} + \rho(\mathbf{u} \cdot \nabla)\mathbf{u} = \nabla \cdot \left[-p\mathbf{I} + \mu\left(\nabla \mathbf{u} + (\nabla \mathbf{u})^T\right)\right] + \mathbf{F} \tag{2.2}$$

In the Navier-Stokes equations, the magnetic body couple was treated as an external force acting on the fluid continuum. This force and the inlet velocity at the entrance to the model geometry were defined by computational solution of the variable aggregate size model presented in Chapter 6 assuming a 7500A/m applied magnetic field rotating at 5Hz but with the average particle volume fraction an order of magnitude lower than the base case, at 0.01%. To avoid the transient oscillations in the velocity, the time-averaged overall velocity profile, u_y, was utilized. No-slip boundary conditions were applied at the channel walls as well as at the thrombus.

Throughout most of the channel length, the flow field matches the velocity profile defined at the inlet, with no flow across the channel. Near the blockage that velocity profile is inaccurate, however, as the flow in the positive y-direction on the right side of the channel must turn, travel across the channel, and ultimately become the return flow in the negative y-direction on the left side of the channel. This is shown by the streamlines in Figure 7.1a. The y-component of the velocity field is shown in Figure 7.1b. The maximum velocity obtained by the flow heading toward the thrombus is 0.14mm/s, while the maximum magnitude of the return flow velocity is -0.07mm/s.

Although experiments by Pulse Therapeutics demonstrate that a vortex forms near the clot, no such unusual flow effects are predicted by this simulation. This complex behavior would be anticipated, however, if the ferroparticle concentration within the blocked channel was tracked over time. As ferroparticles neared the clot, they would be transported across the channel following the streamlines. The particles would subsequently be drawn back across the channel due to the magnetic field gradient, and the process would repeat. The resulting particle circulation would then lead to flow recirculation.

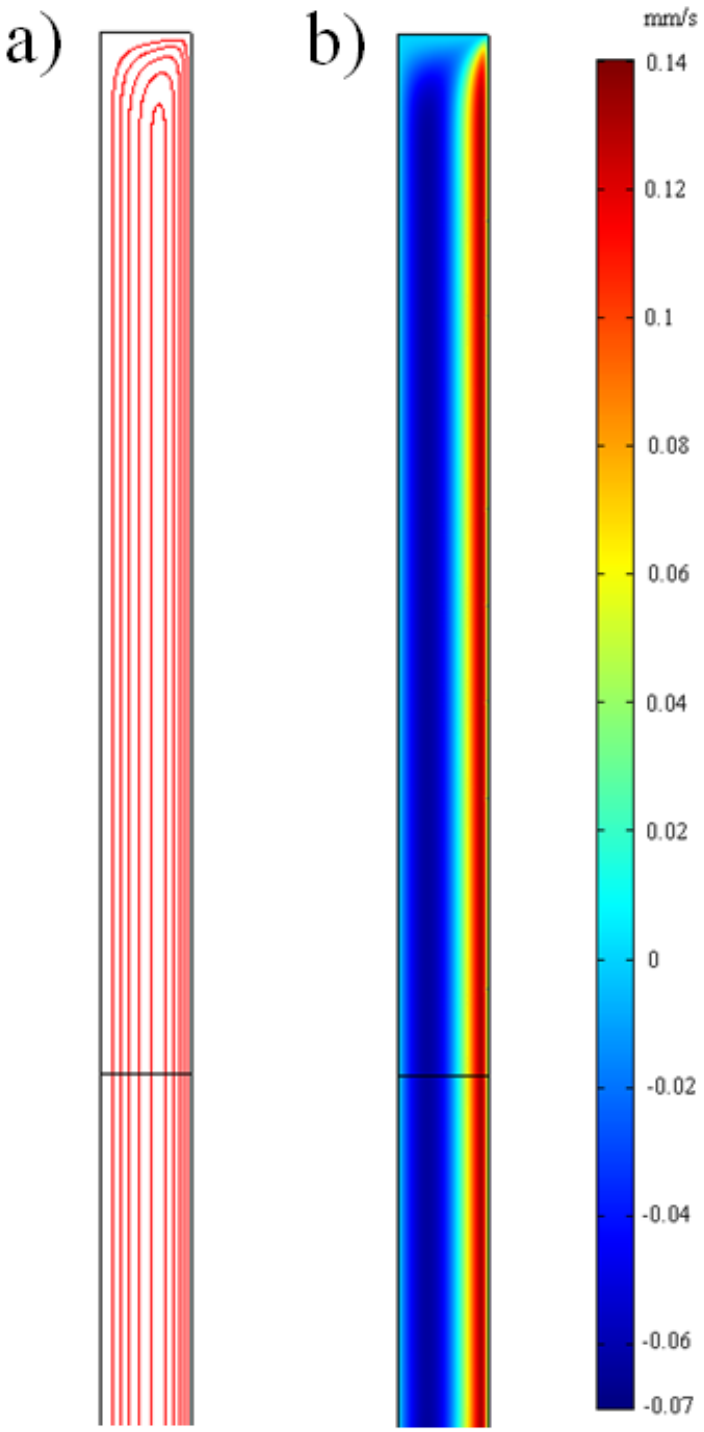

Figure 7.1: a) Streamlines and b) the y-component of the overall velocity in an occluded vessel acted upon by a 7500A/m magnetic field rotating at 5Hz with the ferroparticles accounting for a volume fraction of 0.01%.

7.2 THROMBOLYTIC CONCENTRATION

Computational simulation of the transient evolution of the thrombolytic concentration profile within the blocked vessel was subsequently performed using the steady state flow field. In keeping with the diffusion-limited simulations from Chapter 2, a thrombolytic diffusion coefficient of $8\times10^{-10}m^2/s$ was used. Boundary conditions of no flux of thrombolytic through the channel walls or thrombus were used. For the initial condition, the thrombolytic was assumed to have already penetrated 1cm into the model geometry as shown on the left side of Figure 7.2. The thrombolytic concentration everywhere within that first centimeter was assumed to be initially equal to the administered concentration. Figure 7.2 shows the thrombolytic concentration profile in the blocked channel as a fraction of its administered concentration every 100 seconds for a total of 700s.

The thrombolytic travels the additional 3.5cm from the initial concentration front to the thrombus in just under 300s, or 5 minutes.

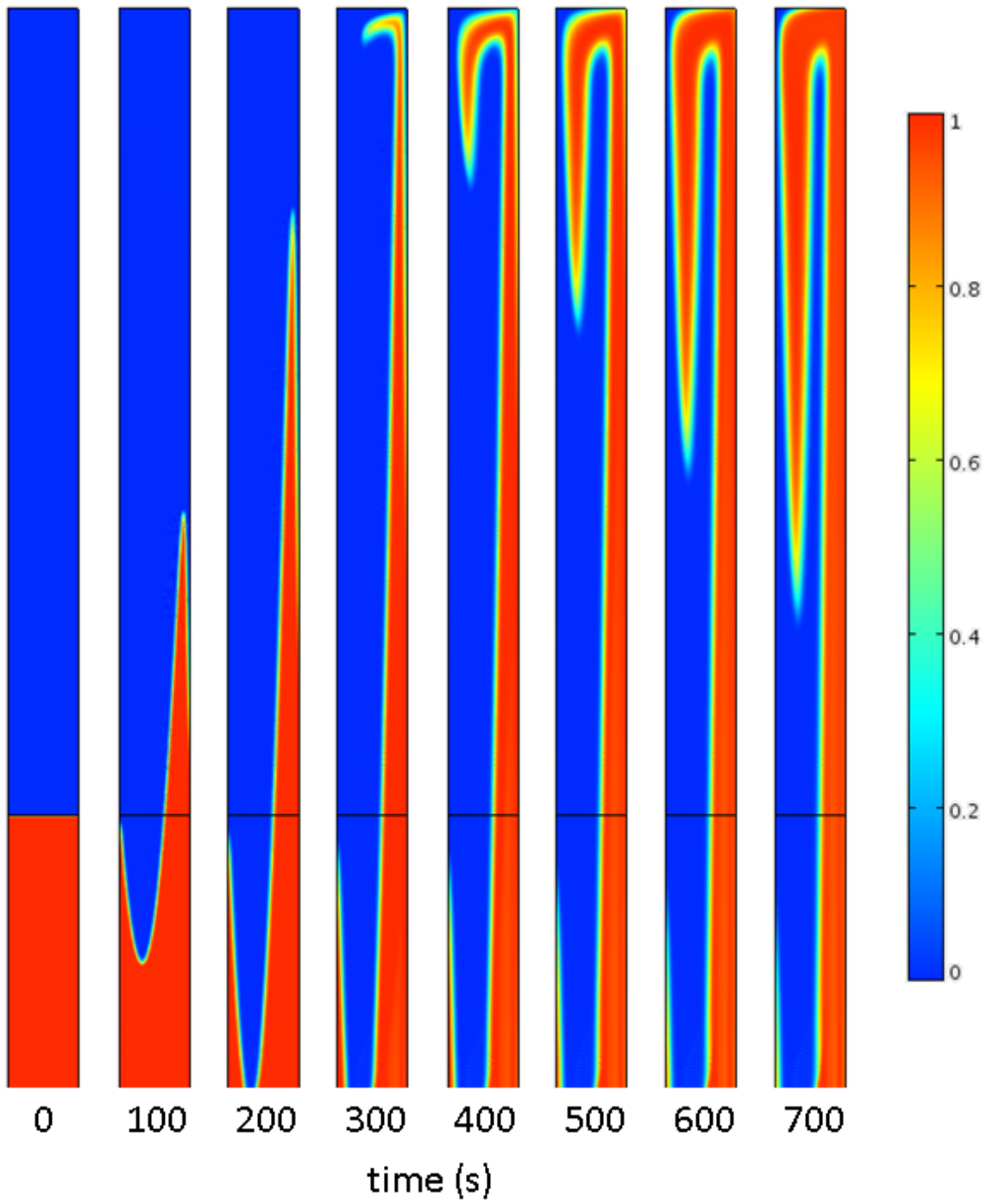

Figure 7.2: Concentration profiles for the thrombolytic, as a fraction of the administered concentration, over time with 100 seconds between images.

Chapter 8: Concluding Remarks

8.1 Conclusions

Magnetically-enhanced transport of thrombolytics through occluded vessels is possible. Applying a sufficiently strong magnetic field with a gradient will make ferroparticles administered with the thrombolytic aggregate into chains on one side of the blocked vessel. For applied magnetic fields above a critical threshold strength, which can be estimated as $H_{crit} = \sqrt{8\eta L^3 Y^C \Omega / (\mu_0 V \alpha_L)}$, the aggregates will rotate at the same rate as the magnetic field. The rotation of these aggregates will induce fluid flow and restore convective transport within the clogged vessel if the magnitude and frequency of the applied magnetic field are carefully selected to yield aggregates of sufficient size and quantity.

Simulation results predicting thrombolytics reaching a clot 3.5cm into an occluded channel, at a concentration comparable to that at which it entered, within five minutes, strongly suggest that the magnetically-enhanced transport method invented by Pulse Therapeutics would be extremely effective in treating strokes. Given the inherently time-sensitive nature of stroke treatment, this would represent an enormous improvement on the current diffusion-limited standard. It should be noted though that a number of assumptions were introduced in Chapter 7 to obtain those results. Experiments conducted by Pulse Therapeutics suggest that, for the simulated occluded vessel size, the thrombolytic should reach the clot in five to fifteen minutes.

Correcting the simulation assumptions will slow the theoretical thrombolytic transport or reduce the amount of thrombolytic predicted to reach the clot. For example, accounting for the reaction of the thrombolytic in the bloodstream will slightly decrease the amount of thrombolytic theoretically reaching the clot. Fortunately, tPA's half-life of 5 to 10 minutes [Gravanis and Tsirka (2008)] and streptokinase's half-life of 23 minutes

[Baker (2003)] are both longer than the predicted transport time to the simulated clot. As such, at least half of the thrombolytic entering the blocked vessel should be able to reach the clot within five minutes.

Including the initial evolution of the ferroparticle concentration profile within the simulated blocked channel and establishing the predicted ferro-aggregate gradient could substantially increase the time required for the thrombolytic to reach the clot. Realistically, the flow field would not already be at steady state when the thrombolytic starts traveling through the blocked vessel. The ferroparticles also need to be transported through the clogged vessel. In order to induce flow toward the clot in a particular location, ferroparticles must be present there. As such, the region of the occluded channel near to the blockage would not experience induced flow until about the same time that thrombolytic initially reached that region.

Even if accurate tracking of the ferroparticles and ferro-aggregates increases the theoretical time required for thrombolytic to reach the clot by an entire order of magnitude, the magnetically-enhanced transport will still be vastly superior to the current standard of diffusion-limited transport. The magnetically-enhanced transport would still carry at least 0.1 percent of the administered thrombolytic to the clot, 3.5cm into the 3mm wide occluded vessel, within 50 minutes. Simulation of the diffusion-limited transport predicts that less than 10^{-4} percent of the administered thrombolytic is delivered to a thrombus located a mere 0.5cm into a 3mm wide blocked blood vessel within 2 hours, assuming that the blocked vessel branches off from its neighboring unblocked vessel at a 45° angle.

Given the magnitude of this improvement, the practical application of magnetically-enhanced thrombolytic transport for stroke treatment in hospitals could save

an untold number of lives. Developing guidelines and protocols for the treatment method should be a priority.

8.2 SUGGESTED FUTURE WORK

The rate of thrombolytic delivery could be better understood and more easily predicted if the magnetically-enhanced convective-diffusive transport model, discussed in Chapter 7, accounted for the transient evolution of the ferro-aggregate concentration profile in the occluded vessel. Another possible improvement to that model is accounting for the reaction of the thrombolytic both in the bloodstream and at the clot. Transiently keeping track of the quantity of thrombolytic actually delivered to the thrombus would also be beneficial.

More fundamentally, the magnetic field source in the model could be permitted to rotate in all three spatial dimensions and the corresponding aggregate dynamics could be analyzed in 3D. The effect of the three-dimensional rotation of the aggregates on the flow field could then be considered. The geometry of the occluded vessel could also be improved from the current two-dimensional channel into a three-dimensional tube. Including the neighboring unblocked vessel in the model geometry would allow for analysis of the entrance effects going into the occluded vessel. The length, diameter, and branch angle of the blocked vessel could be treated as system variables as in Chapter 2. Additionally, the magnetic field source could be offset from the model geometry in different directions in order to further investigate the effect of H-field source position. Since aggregate concentration is highest near a vessel wall, the interactions between the wall and the spinning aggregates are important and should be considered in future models.

Appendix A: Nomenclature

A.1 Chapter 2 Nomenclature

Latin alphabet based

c	concentration (mol/m^3; μM)
D	diameter of the occluded vessel (m; mm)
$D_{\tau,P}$	diffusion coefficient of thrombolytic/plasminogen (m^2/s; mm^2/hr)
$\mathbf{F}$	external forces (N)
$\mathbf{I}$	identity matrix
k	reaction rate constant
k'	pseudo-reaction rate constant
L	length of the occluded vessel (m; cm)
p	pressure (Pa)
P	free plasminogen concentration (mol/m^3; μM)
P_b	bound plasminogen concentration (mol/m^3; μM)
Q	blood flow rate in unblocked vessel (m^3/s; mL/min)
R	reaction rate ($\text{mol} \cdot \text{m}^{-3} \cdot \text{s}^{-1}$)
S	streptokinase concentration (mol/m^3; μM)
t	time (s)
T	tPA concentration (mol/m^3; μM)
$\mathbf{u}$	velocity (m/s; cm/s)

Greek alphabet based

δ	characteristic clot thickness (m)
θ	angle between the blocked and unblocked vessels ($\leq 90°$)
μ	viscosity of fluid medium ($\text{Pa} \cdot \text{s}$)

ρ density of fluid medium (kg/m^3)

τ thrombolytic concentration (mol/m^3)

Subscripts

b bound

i at occluded vessel inlet

P plasminogen

τ thrombolytic

0 initial

1 during first hour following start of administration; during administration

2+ after first hour following start of drug administration; after administration

A.2 CHAPTER 3-6 NOMENCLATURE

Latin alphabet based

a length of an aggregate's semi-minor axis (m)

c ferroparticle number density (particles/m^3)

C ferroparticle number density (dimensionless)

$C_{\#}$ constant of integration

d channel diameter (m)

d effective hydrodynamic diffusion vector (m^2/s)

D effective hydrodynamic diffusion (dimensionless)

$\mathbf{e}^{\infty}$ strain rate due to the flow (s^{-1})

$\mathbf{E}^{\infty}$ strain rate due to the flow (dimensionless)

f function

$\mathbf{G}_A$ anti-symmetric stress tensor (dimensionless)

$\mathbf{G}_M$ magnetic torque (dimensionless)

$\mathbf{h}$	applied magnetic field (A/m)
$\mathbf{H}$	applied magnetic field (dimensionless)
$\mathbf{K}$	rotation matrix
L	length of an aggregate's semi-major axis (m)
$\mathbb{m}$	magnetic dipole moment ($\mathrm{A}\cdot\mathrm{m}^2$)
$\mathbf{m}$	magnetization of the aggregates (A/m)
$\mathbf{M}$	magnetization of the aggregates (dimensionless)
n	aggregate number density (aggregates/m^3)
n_a	number of particles per aggregate
N	aggregate number density (dimensionless)
p	pressure (Pa)
P	pressure (dimensionless)
$\mathbf{p}$	director describing aggregate orientation
$\mathbf{r}$	displacement from magnetic field source (m)
r_p	radius of ferroparticles (m)
t	time (s)
$\mathbf{T}_A$	anti-symmetric stress tensor
$\mathbf{T}_{H,M}$	hydrodynamic/magnetic torque ($\mathrm{N}\cdot\mathrm{m}$)
$\mathbf{u}$	velocity (m/s)
$\mathbf{U}$	velocity (dimensionless)
V	volume of an aggregate (m^3)
V_P	volume of a particle (m^3)
x	position across channel (m)
x_0	distance between the magnetic field source and the channel wall at x=0
X	position across channel (dimensionless)

X^C function of aggregate eccentricity (dimensionless)

y position along channel (m)

Y position long channel (dimensionless)

$Y^{C,H}$ functions of aggregate eccentricity (dimensionless)

Greek alphabet based

$\alpha_{L,T}$ functions defining aggregate magnetization (dimensionless)

β ratio relating magnetic body force to hydrodynamic diffusion (dimensionless)

ε eccentricity of the aggregates (dimensionless)

η viscosity of fluid medium ($\mathrm{Pa \cdot s}$)

θ offset angle between aggregate orientation and applied magnetic field orientation

μ_0 magnetic permeability of a vacuum ($\mathrm{N/A^2}$)

μ_f relative magnetic permeability of fluid (dimensionless)

μ_p relative magnetic permeability of ferro-aggregates (dimensionless)

ρ density of fluid medium ($\mathrm{kg/m^3}$)

τ time (dimensionless)

ϕ orientation angle of the aggregates

Φ average volume fraction of particles/aggregates

χ_M magnetic susceptibility (dimensionless)

Ψ variable of integration

$\boldsymbol{\omega}$ angular velocity of the aggregates (rad/s)

$\boldsymbol{\omega}^{\infty}$ angular velocity of the bulk fluid (rad/s)

Ω angular velocity of the applied magnetic field (rad/s)

$\boldsymbol{\Omega}$ angular velocity of the aggregates (dimensionless)

Subscripts

A	anti-symmetric
crit	critical
g	due to gradient of H-field
H	hydrodynamic
m	magnetically-induced
M	magnetic
p	pressure-induced
P	particle
x	across the channel
y	along the channel; in flow direction

Appendix B: Functional Parameters of Aggregate Orientation

The hydrodynamic torque on the aggregates is a function of three different eccentricity dependent values:

$$X^C = \frac{4}{3}\varepsilon^3\left(1-\varepsilon^2\right)\left[2\varepsilon-\left(1-\varepsilon^2\right)\ln\left(\frac{1+\varepsilon}{1-\varepsilon}\right)\right]^{-1}, \tag{B.1}$$

$$Y^C = \frac{4}{3}\varepsilon^3\left(2-\varepsilon^2\right)\left[-2\varepsilon+\left(1+\varepsilon^2\right)\ln\left(\frac{1+\varepsilon}{1-\varepsilon}\right)\right]^{-1}, \tag{B.2}$$

$$Y^H = \frac{4}{3}\varepsilon^5\left[-2\varepsilon+\left(1+\varepsilon^2\right)\ln\left(\frac{1+\varepsilon}{1-\varepsilon}\right)\right]^{-1}. \tag{B.3}$$

In order to describe the rate of change of the aggregate orientation, a matrix **K(p)** is multiplied by the aggregate orientation rate. This transformation matrix functions to describe the relationship between the fixed spatial Cartesian coordinate system of the channel and the coordinate system of the rigid body described by its Euler angles. It is given by

$$\mathbf{K}(\mathbf{p}) = \begin{pmatrix} 0 & \cos\theta & -\sin\theta\sin\phi \\ -\cos\theta & 0 & \sin\theta\cos\phi \\ \sin\theta\sin\phi & -\sin\theta\cos\phi & 0 \end{pmatrix}. \tag{B.4}$$

Bibliography

Allan R. and S. Mason, "Particle behaviour in shear and electric fields II. Rigid rods and spherical doublets," *Proceedings of the Royal Society of London, Series A: Mathematical, Physical and Engineering Sciences* **267** (1328), 62-76 (1962).

Alleman A. J., W. Barnard and R. L. Radford, United States Patent No. US 8,603,014 B2 (Dec 10, 2013).

Anand S. and S. L. Diamond, "Computer Simulation of Systemic Circulation and Clot Lysis Dynamics During Thrombolytic Therapy That Accounts for Inner Clot Transport and Reaction," *Circulation* **94** (4), 763-774 (1996).

Baker W. F., Jr., "Thrombolytic therapy: clinical applications," *Hematology-Oncology Clinics of North America* **17** (1), 283-311 (2003).

Banerjee A., Y. Chisti and U. C. Banerjee, "Streptokinase - a clinically useful thrombolytic agent," *Biotechnology Advances* **22** (4), 287-307 (2004).

Barlow G. H., L. Summaria and K. C. Robbins, "Molecular weight studies on human plasminogen and plasmin at the microgram level," *Journal of Biological Chemistry* **244** (5), 1138-1141 (1969).

Bossis G., O. Volkova, S. Lacis and A. Meunier. "Magnetorheology: Fluids, Structures and Rheology." *Ferrofluids*. Ed. Odenbach. Vol. 594. Lecture Notes in Physics. 202-230 (Springer, Berlin, 2002).

Broderick J. P., "Endovascular Therapy for Acute Ischemic Stroke," *Stroke* **40** (3), S103-S106 (2009).

Broderick J. P. and W. Hacke, "Treatment of Acute Ischemic Stroke - Part I: Recanalization Strategies," *Circulation* **106** (12), 1563-1569 (2002).

Cederholm-Williams S. A., "Concentration of plasminogen and antiplasmin in plasma and serum," *Journal of Clinical Pathology* **34** (9), 979-981 (1981).

Chen S., X. He, V. Bertola and M. Wang, "Electro-osmosis of non-Newtonian fluids in porous media using lattice Poisson-Boltzmann method," *Journal of Colloid and Interface Science* **436**, 186-193 (2014).

Chen X., J. E. Leeman, J. Wang, J. J. Pacella and F. S. Villanueva, "New insights into mechanisms of sonothrombolysis using ultra-high-speed imaging," *Ultrasound in Medicine and Biology* **40** (1), 258-262 (2014).

Chiesi USA, http://chiesiusa.com/products/.

Clements M. and R. Bonnecaze, "Diffusion limited delivery of streptokinase and tPA to a thrombus," *Cardiovascular Engineering and Technology* **4** (4), 364-373 (2013).

Corbyn Z., "Stroke: A growing global burden," *Nature* **510** (7506), S2-S3 (2014).

Cornu C., F. Boutitie, L. Candelise, J. P. Boissel, G. A. Donnan, M. Hommel, A. Jaillard and K. R. Lees, "Streptokinase in Acute Ischemic Stroke: An Individual Patient Data Meta-Analysis - The Thrombolysis in Acute Stroke Pooling Project," *Stroke* **31** (7), 1555-1560 (2000).

Creighton F. M., United States Patent No. US 8,313,422 B2 (Nov 20, 2012).

Creighton F. M., United States Patent No. US 8,529,428 B2 (Sep 10, 2013).

Creighton F. M., United States Patent No. US 8,715,150 B2 (May 6, 2014).

Davis R. H., "Hydrodynamic diffusion of suspended particles: a symposium," *Journal of Fluid Mechanics* **310**, 325-335 (1996).

Demetriades S., "Effect of electrostatic fields on the orientation of colloidal particles immersed in shear flow," *Journal of Chemical Physics* **29** (5), 1054-1063 (1958).

Diamond S. L. and S. Anand, "Inner Clot Diffusion and Permeation During Fibrinolysis," *Biophysical Journal* **65** (6), 2622-2643 (1993).

Donnan G. A., D. W. Howells, R. Markus, D. Toni and S. M. Davis, "Can the time window for administration of thrombolytics in stroke be increased," *CNS Drugs* **17** (14), 995-1011 (2003).

Drugs.com, http://www.drugs.com/international/.

Eissa A., I. Krass and B. V. Bajorek, "Optimizing the management of acute ischaemic stroke: a review of the utilization of intravenous recombinant tissue plasminogen activator (tPA)," *Journal of Clinical Pharmacy and Therapeutics* **37** (6), 620-629 (2012).

Farajzadeh R., A. Ameri, M. Faber, D. van Batenburg, D. Boersma and J. Bruining, "Effect of continuous, trapped, and flowing gas on performance of alkaline surfactant polymer (ASP) flooding," *Industrial & Engineering Chemistry Research* **52** (38), 13839-13848 (2013).

Food and Drug Administration, http://www.accessdata.fda.gov/scripts/cder/drugsatfda/.

Furie B. and B. C. Furie, "Mechanisms of disease: mechanisms of thrombus formation," *New England Journal of Medicine* **359** (9), 938-949 (2008).

Gan G., "Simulation of buoyancy-induced flow in open cavities for natural ventilation," *Energy and Buildings* **38**, 410-420 (2006).

Gardell S. J., "The search for the ideal thrombolytic agent: Maximize the benefit and minimize the risk," *Toxicologic Pathology* **21** (2), 190-198 (1993).

Genentech, http://www.gene.com/patients/medicines.

Gobin Y. P., S. Starkman, G. R. Duckwiler *et al.*, "MERCI 1 - A Phase 1 Study of Mechanical Embolus Removal in Cerebral Ischemia," *Stroke* **35** (12), 2848-2853 (2004).

Gomez-Ramirez A., P. Kuzhir, M. T. Lopez-Lopez, G. Bossis, A. Meunier and J. D. G. Duran, "Steady shear flow of magnetic fiber suspensions: Theory and comparison with experiments," *Journal of Rheology* **55** (1), 43-67 (2011).

Gravanis I. and S. E. Tsirka, "tPA as a therapeutic target in stroke," *Expert Opinion on Therapeutic Targets* **12** (2), 159-170 (2008).

Helgesen G., P. Pieranski and A. T. Skjeltorp, "Nonlinear phenomena in systems of magnetic holes," *Physical Review Letters* **64** (12), 1425-1428 (1990).

Herman I. P., *Physics of the Human Body*. (Springer, Berlin, 2007).

Hermentin P., T. Cuesta-Linker, J. Weisse, K.-H. Schmidt, M. Knorst, M. Scheld and M. Thimme, "Comparative Analysis of the Activity and Content of Different Streptokinase Preparations," *European Heart Journal* **26** (9), 933-940 (2005).

Hill M. D., W. Brooks, A. Mackey *et al.*, "Stroke After Carotid Stenting and Endarterectomy in the Carotid Revascularization Endarterectomy Versus Stenting Trial (CREST)," *Circulation* **126** (25), 3054-3061 (2012).

Hinch E. J. and L. G. Leal, "Rotation of small non-axisymmetric particles in a simple shear flow," *Journal of Fluid Mechanics* **92** (3), 591-608 (1979).

Horvath D. and P. Kopcansky, "Magnetic dimer motion effects in a rotating magnetic field (A qualititative model of magnetoviscosity and permittivity in magnetorheological suspensions)," *Czechoslovak Journal of Physics* **43** (6), 671-681 (1993).

Huibers A., G. de Borst, S. Wan, F. Kennedy, A. Giannopoulos, F. Moll and T. Richards, "Non-invasive Carotid Artery Imaging to Identify the Vulnerable Plaque: Current Status and Future Goals," *European Journal of Vascular and Endovascular Surgery* **50** (5), 563-572 (2015).

Jaillard A., C. Cornu, A. Durieux, T. Moulin, F. Boutitie, K. R. Lees and M. Hommel, "Hemorrhagic Transformation in Acute Ischemic Stroke - The MAST-E Study," *Stroke* **30** (7), 1326-1332 (1999).

Jeffery G. B., "The motion of ellipsoidal particles immersed in a viscous fluid," *Proceedings of the Royal Society of London, Series A: Mathematical, Physical and Engineering Sciences* **102** (715), 161-179 (1922).

Kim S. and S. J. Karrila, *Microhydrodynamics: Principles and Selected Applications*. (Butterworth-Heinemann, Boston, 1991).

Kwon S., A. G. Hartzema, P. W. Duncan and S. Min-Lai, "Disability measures in stroke - Relationship among the Barthel Index, the Functional Independence Measure, and the Modified Rankin Scale," *Stroke* **35** (4), 918-923 (2004).

Langer D., M. Alexander, V. Janardhan *et al.*, "The Penumbra Pivotal Stroke Trial - Safety and Effectiveness of a New Generation of Mechanical Devices for Clot Removal in Intracranial Large Vessel Occlusive Disease," *Stroke* **40** (8), 2761-2768 (2009).

Leipnitz G., C. Miyashita, M. Heiden, G. Blohn, M. Kohler and E. Wenzel, "Reference values and variability of plasminogen in healthy blood donors and its relation to parameters of the fibrinolytic system," *Haemostasis* **18** (Suppl. 1), 61-68 (1988).

Lottenberg R., L. E. DesJardin, H. Wang and M. D. P. Boyle, "Streptokinase-Producing Streptococci Grown in Human Plasma Acquire Unregulated Cell-Associated Plasmin Activity," *Journal of Infectious Diseases* **166** (2), 436-440 (1992).

Machi P., V. Costalat, K. Lobotesis, I. L. Maldonado, J. F. Vendrell, C. Riquelme and A. Bonafe, "Solitaire FR Thrombectomy System: Immediate Results in 56 Consecutive Acute Ischemic Stroke Patients," *Journal of Neurointerventional Surgery* **4** (1), 62-66 (2011).

Mattle H. P., "Intravenous or intra-arterial thrombolysis? It's time to find the right approach for the right patient," *Stroke* **38** (7), 2038-2040 (2007).

Maulaz A. B., R. T. Martins, M. d. C. Ribeiro, R. Londero, J. O. D Soares and J. G. Fernandes, "Could thrombolytic approaches in acute stroke benefit from stringent selection criteria?," *Nature: Clinical Practice: Neurology* **5** (3), 138-139 (2009).

McCabe J. M., P.-H. Huang, L. Riedl, A. C. Eisenhauer and P. Sobieszczyk, "Usefulness and Safety of Ultrasound-Assisted Catheter-Directed Thrombolysis for Submassive Pulmonary Emboli," *American Journal of Cardiology* **115** (6), 821-824 (2015).

McDowell M. A., C. D. Fryar, C. L. Ogden and K. M. Flegal, "Anthropometric Reference Data for Children and Adults: United States, 2003-2006," *National Health Statistics Reports* **10**, 1-45 (2008).

Mehta R. and A. D. Shapiro, "Plasminogen deficiency," *Haemophilia* **14** (6), 1261-1268 (2008).

Microbix, https://microbix.com.

Miller C., E. Hill and M. Moutier, "Remediation of DNAPL-contaminated subsurface systems using density-motivated mobilization," *Environmental Science & Technology* **34** (4), 719-724 (2000).

Norris V., A. R. Thierry, P. Amar, I. B. Holland and F. Molina, "The mimic chain reaction," *Journal of molecular microbiology and biotechnology* **22** (5), 335-343 (2012).

Parrado J., F. Conejero-Lara, R. A. G. Smith, J. M. Marshall, C. P. Ponting and C. M. Dobson, "The domain organization of streptokinase: Nuclear magnetic resonance, circular dichroism, and functional characterization of proteolytic fragments," *Protein Science* **5** (4), 693-704 (1996).

Piebalgs A. and X. Y. Xu, "Towards a multi-physics modelling framework for thrombolysis under the influence of blood flow," *Journal of the Royal Society Interface* **12** (113), 1-10 (2015).

Powers W. J., C. P. Derdeyn, J. Biller *et al.*, "2015 American Heart Association/American Stroke Association Focused Update of the 2013 Guidelines for the Early Management of Patients with Acute Ischemic Stroke Regarding Endovascular Treatment - A Guideline for Healthcare Professionals from the American Heart Association/American Stroke Association," *Stroke* **46** (10), 3020-3035 (2015).

Reilly M. J., *Enhancing the mechanical properties of a peptide-based hydrogel via covalent crosslinking*. ProQuest, 2008.

Rocha A. and A. Acrivos, "Experiments on the effective conductivity of dilute dispersions containing highly conducting slender inclusions," *Proceedings of the Royal Society of London, Series A: Mathematical, Physical and Engineering Sciences* **337** (1608), 123-133 (1974).

Roger V. L., A. S. Go, D. M. Lloyd-Jones *et al.*, "Heart disease and stroke statistics-2012 update: A report from the American Heart Association," *Circulation* **125**, e2-e220 (2012).

Roos S. T., L. J. Juffermans, J. Slikkerveer, E. C. Unger, T. R. Porter and O. Kamp, "Sonothrombolysis in acute stroke and myocardial infarction: A systematic review," *IJC Heart & Vessels* **4** (1), 1-6 (2014).

Rosensweig R. E., *Ferrohydrodynamics*. (Cambridge University Press, Cambridge, 1985).

Rubiera M. and A. V. Alexandrov, "Sonothrombolysis in the Management of Acute Ischemic Stroke," *American Journal of Cardiovascular Drugs* **10** (1), 5-10 (2010).

Runge M. S., T. Quertermous and E. Haber, "Plasminogen Activators: The old and the new," *Circulation* **79** (2), 217-224 (1989).

Sedaghat M. H., A. Hatampour and R. Razmi, "Investigating the role of polymer type and dead end pores' distribution on oil recovery efficiency during ASP flooding," *Egyptian Journal of Petroleum* **22** (2), 241-247 (2013).

Shine A. and R. Armstrong, "The rotation of a suspended axisymmetric ellipsoid in a magnetic field," *Rheologica Acta* **26** (2), 152-161 (1987).

Smith W. S., G. Sung, J. Saver *et al.*, "Mechanical Thrombectomy for Acute Ischemic Stroke - Final Results of the Multi MERCI Trial," *Stroke* **39** (4), 1205-1212 (2008).

Sun H. and H. Guo, "Fluid motion induced by acoustic field in microchannel," *Proceedings of 2007 IEEE International Symposium on Ultrasonics*, 1866-1869 (2007).

Van de Werf F. J., "The ideal fibrinolytic: Can drug design improve clinical results?," *European Heart Journal* **20** (20), 1452-1458 (1999).

Verstraete M., "The search for the ideal thrombolytic agent," *Journal of the American College of Cardiology* **10** (5), 4B-10B (1987).

Walpole S. C., D. Prieto-Merino, P. Edwards, J. Cleland, G. Stevens and I. Roberts, "The weight of nations: an estimation of adult human biomass," *BMC Public Health* **12**, 439-444 (2012).

Wardlaw J. M., V. Murray, E. Berge, G. del Zoppo, P. Sandercock, R. L. Lindley and G. Cohen, "Recombinant tissue plasminogen activator for acute ischaemic stroke: an updated systematic review and meta-analysis," *Lancet* **379** (9834), 2364-2372 (2012).

White W. F., G. H. Barlow and M. M. Mozen, "Isolation and Characterization of Plasminogen Activators (Urokinase) from Human Urine," *Biochemistry* **5** (7), 2160-2169 (1966).

World Health Organization, http://www.who.int/medicines/publications/en/.